An investigation into the lift generation of a rotating Coanda-based system, and the implementation of its control mechanisms.

Maman, Jelal

Award date:
2019

Awarding institution:
University of Bath

An investigation into the lift generation of a rotating Coanda-based system, and the implementation of its control mechanisms.

Jelal G. Maman

A thesis submitted for the degree of Doctor of Philosophy
University of Bath
Department of Mechanical Engineering
February 2019

Primary supervisor: Michael Carley

Secondary supervisor: Pejman Iravani

Abstract

The Conda effect is the tendency of a fluid flow to adhere to and follow the curvature of a contacting surface. The demand for micro air vehicles is on the rise, and in the search for more efficient unmanned flight, this effect has been successfully implemented in a UAV design by various teams. This design consists of placing a toroidal surface under a fan. The jet is deflected outwards on top of the surface. Due to the Coanda effect, flow is redirected downwards producing an upwards force. This design's control flaps are located at the bottom edge of the curved surface. The fan's torque is countered using actuated stators.

In this thesis, a novel system utilising a rotating surface in conjunction with the Coanda effect is designed. The curvature is altered so that jet exits the nozzle at 45^o to the horizontal. The rotating surface is used to counter the fan's torque and control surfaces are mounted at the nozzle.

An analytical model of such a flow is investigated in order to determine a control framework. Computational and experimental data is generated to determine its lift capabilities. Both sets of results show the lift varies quadratically with respect to the jet velocity. Similarly, the torque varies quadratically with the disk angular velocity. These models are subsequently used to measure the control moments generated by flaps on the craft. Both models generated significant control responses. The computational data clearly shows the variation of lift coefficient with flap deflection is partially linear. However, the experimental data seems to go through multiple regimes. The data was also subject to a vibrational analysis.

In the discussion, differences and parallels between the various models used are put forward. Recurring frequencies observed in the vibrational analysis of the experimental data are used to strengthen the case for the hypothesized flow regimes. A comparison is made between the traditional and novel design. In a non-spinning configuration, the former is more efficient. In a spinning configuration however, it does not suffer from radial flow ejection causing separation.Finally, it is shown that the system studied is capable of controlled flight. Furthermore, arguments are made to show it may be inherently more stable than a traditional Coanda craft. Some improvements and future works are also suggested.

Contents

1 Introduction **4**

2 Literature review **7**
2.1 History of the Coanda effect 7
2.2 State of the art 10
2.3 Mathematical models 11
2.3.1 The flow of a jet over a curved surface 12
2.3.2 The flow due to a rotating disk 14
2.3.3 The flow due to a rotating sphere in a free stream 15

3 Methods **18**
3.1 Mathematical models 21
3.1.1 Aerodynamic model 23
3.1.2 Control model 26
3.2 CFD analysis 33
3.2.1 Validation 33
3.2.2 Designs and measurements 39
3.3 Experimental setup 45
3.3.1 Rig evolution 45
3.3.2 Load cell 47
3.3.3 Final build 50
3.4 Summary 61

4 Results **62**
4.1 Boundary layer 62
4.2 Pressure distribution 67
4.2.1 Traditional model 68
4.2.2 Novel model 71
4.3 Lift Generation 73
4.4 Control results 81
4.4.1 Computational 81

4.4.2 Experimental data 82

5 Discussion **89**
5.1 Results Summary 89
5.1.1 Boundary layer and pressure results 89
5.1.2 Lift tests 91
5.1.3 Control data 94
5.2 Design comparison 97
5.2.1 Non spinning design 98
5.2.2 Spinning design 99
5.2.3 Other design considerations 101
5.3 Control and stability 101
5.3.1 Control moments 101
5.3.2 Stability 102

6 Conclusion **106**

Table of symbols

coordinate frames

r	distance from centre of curvature	m
x	horizontal axis towards flight direction (In 3D)	m
x	horizontal axis (In 2D)	m
y	horizontal axis normal to flight direction (In 3D)	m
y	vertical axis (In 2D)	m
z	vertical axis (In 3D)	m
z	distance from surface (In 2D)	m
α	angle about x	rad
β	angle about y	rad
γ	angle about z	rad
θ	angular distance along the disk	rad
$\overline{\theta}$	curvature deflection from the horizontal plane	rad

Subscripts

B	away from flight direction
c	2D chord componoent
C	compressor component
D	disk component
F	in flight direction
l	bottom surface
Ld	left diagonal of disk
p	center of pressure position
Rd	right diagonal of disk
u	upper surface
x	in x 3D dimension
y	in y 3D dimension
z	in z 3D dimension

Geometric properties

AR	aspect ratio	
c_M	centre of mass	
h	nozzle height	m
I_C	compressor's moment of inertia in rotation axis	kg.m^2
I_D	disk's moment of inertia in rotation axis	kg.m^2
I_x	system's moment of inertia in x	kg.m^2
I_y	system's moment of inertia in y	kg.m^2
I_z	system's moment of inertia in z	kg.m^2
n	number of control surfaces	
R	disk curvature radius	m
S_c	cross Sectional Area $S_c = \pi(x_m^2 - x_0^2)$	m^2
$\bar{x}$	mean surface distance from centreline $\frac{x_0+x_m}{2}$	m
x_0	see figure 3.1, 3.2	m
x_{in}	see figure 3.1, 3.2	m
x_m	see figure 3.1, 3.2	m
Δ	span of control surfaces	rad
η	control surface angle	rad
η_{min}	minimum control surface angle	rad
η_r	range of control surface angles	rad

Physical properties

b	slope of the lift coefficient curve	
B	rotation parameter defined in chapter 3	
c_L	lift coefficient	N/A
c'_L	configurational lift coefficient	
c_{L0}	lift coefficient at $\eta = 0$	
δc_L	change in lift coefficient due to a control surface	rad^{-1}
d	duty of the compressor	%
e_r	standard deviation of measurement due to vibrations	N
e_x	standard deviation of measurements between experiments	N
F	force	N
F_{XY}	horizontal force magnitude	N
J	transverse force component 3D as seen in figure 3.3	N
K	radial force component 3D as seen in figure 3.3	N
L	lift	N
L_T	total spin angular momentum	
m	total mass of system	kg
M	Moment	Nm
δM	change in moment due to a control action	$\text{Nm}/^o$
$\dot{m}$	mass flow rate	kg.s^{-1}
p	local pressure	Pa
Re	Reynolds number	
T	torque	Nm
u	velocity component in x	m.s^{-1}
U_d	combined jet and angular velocity at mid-chord	m.s^{-1}
U_j	jet Velocity	m.s^{-1}
v	velocity component in y	m.s^{-1}
V	total velocity magnitude	m.s^{-1}
v_r	radial velocity	m.s^{-1}
v_w	transverse velocity	m.s^{-1}
v_θ	tangential velocity	m.s^{-1}
w	velocity component in z	m.s^{-1}
Re	reynolds number	
γ_d	desired heading	rad
$\Delta\theta_p$	change in centre of pressure position due to control action	rad
θ_v	direction of flow velocity	rad
Ω	angular velocity of the disk	Hz
Ω_C	angular velocity of the compressor	rad.s^{-1}
Ω_D	angular velocity of the disk	rad.s^{-1}

Chapter 1

Introduction

In recent years, interest in unmanned aerial aircraft has been increasing. The range of applications for these systems is widening and new designs are being explored. Drones are being starting to be used by emergency response teams, farmers to survey their land, by and film makers. As the legislation gets put into place, larger scale use will be found in areas like drone delivery such as Amazon's Prime Air. More traditional UAV designs, such as quad copters, are now being used commercially and personally on a large scale. This is due to the miniaturization of high performance electric motors and cheaper electronic components. With a rising demand for these platforms, more efficient solutions must be explored.

The Coanda effect, first discovered in the beginning of the 20^{th} century, is currently being researched as a novel method to produce lift. The Coanda effect is the tendency for a flow to follow a curved surface. Working prototypes of this mechanism have been designed and built, notably by J.L Naudin [1] in 2006. In order to further improve on this design, the geometry is altered and a rotating aspect is added. The design produced and tested in this report can be seen in figure 1.1b. Two parameters are the main drivers of force: a outward jet produced by the central fan and blown over the surface, and the black surface's rotation.

The traditional design consist of a fan to induce the flow seen in figure 1.1a. Actuated stators on the curved surface counter moments generated by the fan. Flaps seen on the bottom edge of the surface control the aircraft's pitch and yaw. In the first design iteration, a rotation was added to the Coanda surface and the control surfaces were relocated to the nozzle before the curvature. In figure 1.1b, the jet inducing fan and control surfaces can be seen on the central assembly of the novel design. Furthermore, the curved surface has been adjusted in order to be compatible with rotation.

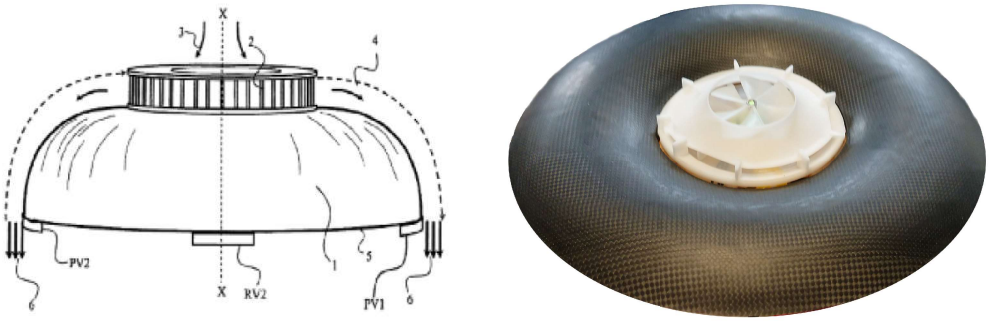

(a) Traditional design diagram [2]. (b) Image of the latest disk prototype.

Figure 1.1: Visual representation of Coanda based aircraft.

Coanda-craft have vertical take off and landing capabilities and manoeuvre, much like a quad copter, by tilting. Moments are applied in the desired direction using the control surfaces. The traditional design, however, utilizes the flaps at the edge of the disk for thrust vectoring. Unmade areal vehicles using the Coanda effect are still emerging. However, from what other groups have shown, these aircraft have some benefits over quad copters, their closest analogue. The first of which is an increase in efficiency due to flow entrainment. Secondly, the lack of external spinning parts in the traditional design makes it safer for human operators as well as for the craft itself. This does not apply to the novel design as the disk rotating. Spin is used for increased stability. Furthermore, it may be possible that the rotation further increases the lifting potential of the design.

Aims

This investigation is framed within aerodynamic and control aspect. The aims of this reports can therefore be divided accordingly:

- Determining the feasibility and practicality of a Coanda based aircraft.
- Understanding the underlying aerodynamic mechanisms.
- Understanding the varying effects of jet and angular velocities in the system.
- Implementing and testing a control system.
- Comparing the novel design proposed to the traditional one.

This project effectively is looking into the underlying mechanisms that would enable a novel type of aircraft. Furthermore, it attempts to improve on an existing design.

Objectives

In order to achieve the stated aims multiple objectives must be completed. These are presented in order and are as follows:

- Generating an analytical model of the system.
- A CFD model of the tested system must be generated and validated against known solutions.
- The CFD model is used to generate the following:
  - Boundary layer velocity profiles.
  - Pressure distribution.
  - Lift and lift coefficients.
  - Control moments.
- An experimental configuration must be designed and built. This setup must be capable of varying the experimental parameters (U_j, Ω, and η).
- The experimental setup is used to measure the following:
  - Forces and moments in 6 axis.
  - Angular and jet velocities.
- The boundary layer and pressure distribution model are used to understand the difference between the mechanisms of the traditional and novel design.
- These models are also used to understand the impact of jet and angular velocity using the B variable.
- The lift performance with respect to jet velocity is experimentally measured and compared with the computational model.
- The control moments generated by actuating the flaps are measured and compared with the computational model.
- Control data is used to determine the system's responses.
- Frequency analysis of the vibrations in experimental data is used to determine potential flow regimes.

Chapter 2

Literature review

The history of the Coanda effect is initially explored in this section, as well as some examples of aircraft using this effect as their primary source of propulsion. The state of the art section explores more recent research in the topic, notably, a working MAV designed by J. L. Naudin and papers investing different aspects of this design.

2.1 History of the Coanda effect

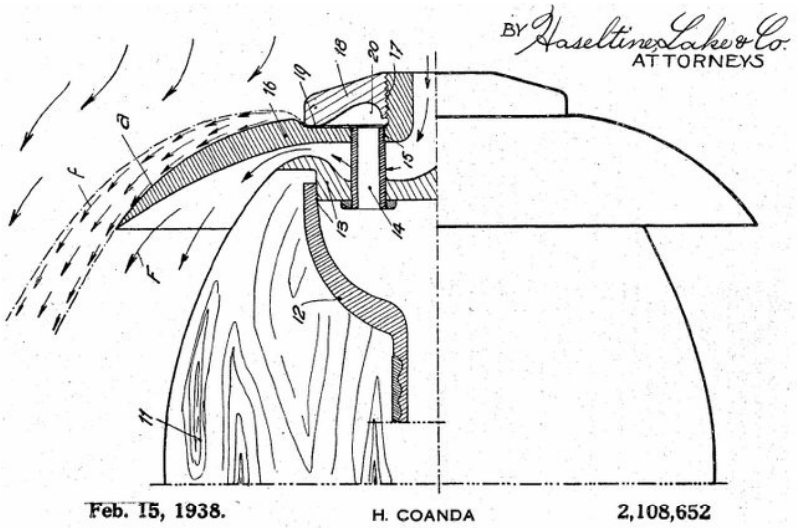

Figure 2.1: Patent made by Henri Coanda [3]

The first instance of recorded experiments involving the Coanda effect to produce lift date back to 1932 [4]. Henri Coanda stipulated that the surrounding air would be entrained due to the jet's shear layer (seen in top of the surface in figure 2.1).

Sucked air, along with the jet, is redirected underneath resulting in lift. In 1951, NACA tested the lift and thrust characteristics of a jet acting on a curved surface or multiple flat plates [5]. The study showed that using flat plates (up to nine) or a curved surface gave a lift of 0.88 and 0.81 of the undeflected thrust respectively.

During the cold war, the Canadian aerospace company AVRO tested the AVRO-car [6] and worked on Project 1794 [7,8]. Due to the politics of the time, most of the research on control systems is not published. It was found during initial testing that the AVRO-car's performance was much less than expected [9]. The main driving force was the redirected thrust produced by the AVRO-car's engines. Very little lift was generated by the curved surface. At low altitude, it performed well as ground effect produced an air cushion. After some improvements to the thrust vector and control systems, it could fly to higher altitudes but only at high speeds and angles of attack [10]. Keeping the pitch corrected at trimmed flight also seemed to be problematic. The lack of lift at high altitudes is due to the small surface area of the craft over which the flow travels. With a larger surface area, more lift would be produced by the pressure difference between the top and bottom surface. This would also increase the amount of entrained flow The jet would in turn be slowed down by the surface friction, and the boundary layer would increase in size. A larger slower moving jet is more efficient [11], therefore the thrust produced by the jet would also benefit from a larger surface area. The lack of a active boundary layer on the majority of the surface creates stagnation points, which are effectively downwards drag. The trimmed angle of attack stability is associated with a centre of drag position in relation to the centre of mass. In an attempt to prevent the nose from dipping, a V-wing shaped surface was attached to the AVRO-car's rear. Aircraft control was improved by the wing but the project was eventually deemed a dead end.

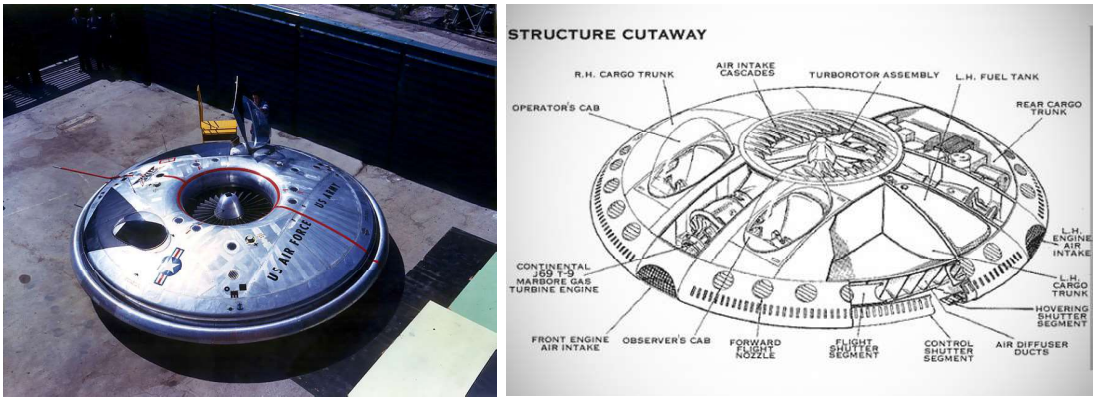

(a) The AVROcar S/N 58-7055 [12] (b) Schematics of the AVROcar

Figure 2.2: A prototype designed and built in the 70s

Other disc shaped aircraft concepts emerged at the height of the cold war such as project 1794 [7] and quite a few different patents [13–15]. These designs, however, utilise the engine jet to produce a downwards thrust rather than blowing on the upper surface. The centre of thrust is located at the exit nozzle underneath the centre line of the craft. This configuration has two potential downfalls: the craft could be unstable at high angle of attack, and the upper surface drag is considerable. If a jet boundary layer were to be present on the upper surface, the surrounding air would be deflected around the craft and drag would be reduced. In the 1970s, military and transport aircraft such as the Antonov An-72 [16] and Boeing YC-14 [17], reduced their take off and landing distance by placing the engines on top of the wing. With a jet boundary layer forming on a section of the wing, greater flap deflection angles can be reached. Since then, the idea has created a new class of high lift devices called the blown flap. A NASA study in the 90s [18] showed that forced circulation around the flap increases the maximum lift coefficient by two or three times more than mechanical flaps. The Coanda effect, as a method of generating the totality of lift, was not revisited until 2006 [1] with the rise of UAVs. The concept used a curved surface to deflect radial flow downwards. Flaps are located at the end of the curvature to vector the thrust. While some of the upwards force is a product of lift, the moments associated with pitch and roll are generated by the thrust. The centre of moment associated with the control surface is much lower than the centre of mass. This can limit the maximum angle of attack, and therefore trim velocity, of the craft.

In recent years the Coanda effect has been increasingly studied in the context of a blown flap [19, 20] due to the increasing accuracy of computational models. These computational investigations show the general characteristics associated with a Coanda flow. The flow generally sticks to the surface, but the model's mesh inflation from the surface needs to be five to ten times the boundary layer thickness as jet tends to subtly interact with surrounding air. An inflated mesh holds the property of having exponentially thinner layers as they get closer to the surface. Parameters that are normally associated with it are the number of layers, growth factor, and the minimum layer height. Computational [21] and experimental [22] (in this case both the upper and lower surface are blown, acting more like an annular wing) investigations have been made on the use of the Coanda effect to generate the whole lift. It was determined that there is a lift associated with Coanda, independent of the downwards redirected thrust. Unfortunately, no research of substance on the control systems involved with this type of aircraft configuration is available in the public domain. The addition of a rotating element Coanda flow has not been investigated in the literature available.

Two main problems arise when looking at a rotating aircraft's control systems. The control surfaces must be placed in a stationary location in an external reference frame. By sectioning the surface into four pieces, each with its own control system,

the pitching and rolling moments can be calculated from the four force vectors of each of the sections (this approach is inspired by the method used in the control of quadcopters [23]). The second complication of a rotating craft is asymmetric flight. The free stream velocity, if high enough in relation to the rotation, will disturb the pressure distribution on the surface. However, one study on Frisbee flight [24] has shown that the lift and drag may not be affected by asymmetry for flight speeds less than 20m/s. This is only applicable for the boundary layer solely formed by the rotating surface. If a jet was present between the surface and ambient air, asymmetry might affect the system differently.

2.2 State of the art

Since J. L. Naudin designed a Coanda based MAV in 2006 [1], multiple papers studying the design have been published [2,25–28]. All of the literature found on the subject is based on the design seen in figure 2.3a. Lift is generated by deflecting the propeller jet downwards. Entrainment by the flow and a more efficient jet generates more vertical force than the propeller alone. Control is achieved by actuating flaps located at bottom edge of the surface. The torque generated by the propeller is countered using stator fins seen in figure 2.3a. A South Korean team optimised and produced a working prototype using this design [28].

(a) Image of the MAV designed by J.L.Naudin [1].

(b) Coanda UAV built in South Korea [28].

Figure 2.3: Existing Coanda effect based MAV prototypes.

The team describes the lift generating mechanism but fail to mention the horizontal component generated by the Coanda effect. A computational optimisation is described followed by the control equations used in the prototype. A flight time comparison with a AR drone 2.0 quad-copter shows the Coanda effect craft outperforming the quad copter by 25% even though the quad copter is lighter. Another argument made by the team is the safety of this device.

Two papers [25, 26] use a two dimensional computational model to analyse this design. One big issue that is present in this type of analysis is the lack flow expansion. The inverse square law will lower the boundary layer velocity to the point of separation due to the adverse pressure gradient. This is specially true in the spherical configuration mentioned in two of the papers [26, 27]. The inlet's distance from the centre is very small compared to the edge and the jet velocity required to ensure attachment is unachievable. The data shown in figure [26] is generated using the same configuration as J. L. Naudin [1]. The tendencies of lift and pressure distribution in figure 2.4 are both similar to data presented in report. However, lift magnitudes presented in that paper are much greater than those measured in this paper.

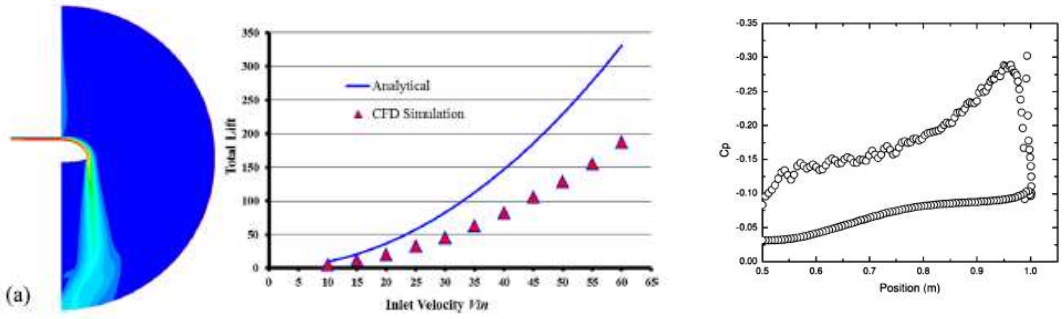

Figure 2.4: Data generated by the University of Malaysia [26]

2.3 Mathematical models

This section describes the mathematical models chosen to test the computational method. Each selected paper's methodology to generate the models is briefly summarized. The flow that would be expected in the studied system is induced by both a jet and rotating surface. Therefore, three papers are used to produce reliable mathematical models. The flow of a jet over a curved surface, a rotating flat plate, and a rotating sphere with a free stream flow are selected. Each of these describe a different part of the system. A solver that can model each individually should model a combined configuration reasonably well.

2.3.1 The flow of a jet over a curved surface

In the case of an impinging jet on a curved surface exhibiting the Coanda effect; let us consider a steady state incompressible flow over a curved surface. This system is best modelled in a cylindrical coordinate frame as shown below. The methods summarised in this section follow a chapter in Bifurcation and Chaos [29].

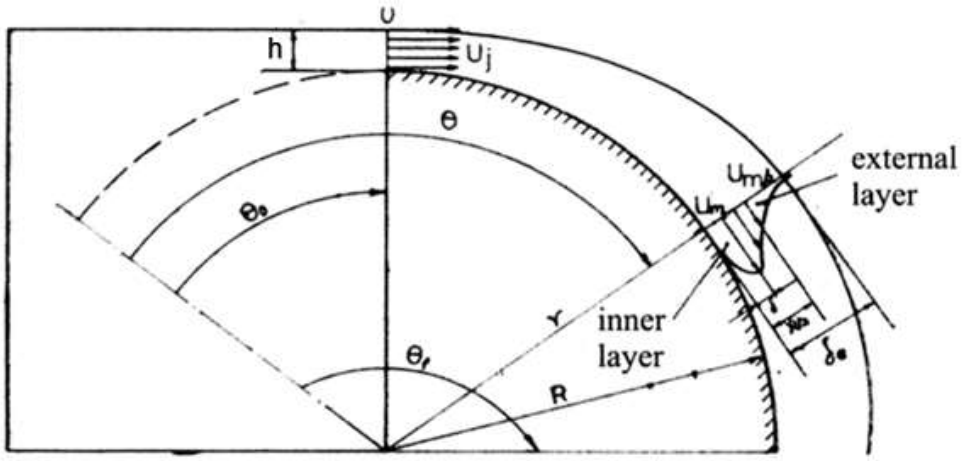

Figure 2.5: Flow and coordinate system for a Coanda flow over a curved surface [29].

The governing Navier-Stokes equations of this system are:

$$\frac{1}{r}\frac{\partial V_\theta}{\partial \theta} + \frac{\partial V_r}{\partial r} + \frac{V_r}{r} = 0, \tag{2.1}$$

$$V_r\frac{\partial V_\theta}{\partial r} + \frac{V_\theta}{r}\frac{\partial V_\theta}{\partial \theta} = \frac{1}{\rho}\frac{\partial \tau}{\partial r}, \tag{2.2}$$

$$\rho\frac{V_\theta^2}{r} = \frac{\partial p}{\partial r}, \tag{2.3}$$

where $\tau = \mu\partial\theta/\partial r$ and is neglected for a laminar flow as it represent the turbulence. The variables are expressed as the following non-dimensional parameters in order to perform a separation of variables and solve the partial differential equation:

$$V_r^* = \frac{V_r}{U_j}; V_\theta^* = \frac{V_\theta}{U_j}; r^* = \frac{r}{R}; p^* = \frac{p}{\rho U_j^2}; \mathrm{Re} = \frac{U_j R}{\nu}; y^* = y/R = r - 1 \tag{2.4}$$

where y is the normal distance from the surface. In order for the model to be accurate the nozzle height z must be much smaller than the radius of curvature. Let η be a modelling variable so that:

$$\eta = \mathrm{Re} y^* \frac{c+1}{\sigma}\theta^{(c+1)(a-1)} \tag{2.5}$$

This variable was found by the paper's author in order to simplify the Navier-Stokes equations. They can therefore be rewritten as an ordinary differential equation using the parameter η:

$$f''' + aff' + (1 - 2a)f'^2 = 0 \tag{2.6}$$

with $f = f' = 0$ for $\eta = 0$ and $f' = f'' = 0$ for $\eta \to \infty$.

In order to simplify the problem, only the laminar case will be examined for the moment. In the results of the paper [29], it is stated that for laminar flow $\sigma = 1$ and $c = 0$; it also states that $a = 0.25$ for a Coanda flow as presented here. Therefore:

$$\eta = \mathrm{Re} y^* \theta^{-3/4} \tag{2.7}$$

In order to solve the boundary value problem for f'' at $\eta = 0$, a parameter is added so that $f_\infty = \lim_{\eta \to \infty} f(\eta)$. This parameter, after further examination, only depends on the jet and curvature characteristics. It can be re-written as:

$$f_\infty = \left(\frac{h}{R}\right)^{1/2} \left(\frac{18}{\mathrm{Re}}\right)^{1/4} \tag{2.8}$$

The addition of the parameter $F = (f/f_\infty)^{1/2}$, ranging from [0, 1] as η ranges from [0, ∞), is used in the equation below with $F = 0$ in order to solve the boundary value problem:

$$f'' = \frac{f_\infty}{72}(1 - F^3)(1 - 4F^3) \tag{2.9}$$

With all the boundary conditions determined, the ODE in equation 2.9 can be solved using an ODE solver such as ode45 in MATLAB. In order to validate the CFD model, the solutions of these ODEs will be used to derive the velocity profile over the surface and ultimately compare it to the same problem solved through ANSYS. In order to determine the velocity profile the following stream function is introduced:

$$\psi = \theta^{a(c+1)} f(\eta) \tag{2.10}$$

The radial and tangential velocities can be rewritten as:

$$V_r^* = -\frac{1}{r^*}\frac{d\psi}{d\theta}; V_\theta^* = \frac{d\psi}{dr^*}$$

The general form of the velocities is shown in equations 2.11 and 2.12; they can be further simplified for a laminar flow using the parameters: $\sigma = 1$; $c = 0$ and $a = 0.25$. The laminar velocity equations are:

$$V_r^* = -\frac{\theta^{-3/4}}{4}[f - 3\eta f'] \tag{2.11}$$

$$V_\theta = \mathrm{Re}.\theta^{-1/2} f' \tag{2.12}$$

2.3.2 The flow due to a rotating disk

The steady state incompressible flow over an infinite rotating disk can be described by the following Navier-Stokes equations in a cylindrical coordinate frame. The methods summarised in this section follow the work of Benton [30].

$$r\frac{\partial u}{\partial r} + r\frac{\partial w}{\partial r} = 0 \tag{2.13}$$

$$u\frac{\partial u}{\partial r} + w\frac{\partial u}{\partial z} - \frac{v^2}{r} = -\frac{1}{\rho}\frac{\partial p}{\partial r} + \nu\left[\frac{\partial^2 u}{\partial r^2} + \frac{\partial}{\partial r}\left(\frac{u}{r}\right) + \frac{\partial^2 u}{\partial z^2}\right] \tag{2.14}$$

$$u\frac{\partial v}{\partial r} + \frac{uv}{r} + w\frac{\partial v}{\partial z} = \nu\left[\frac{\partial^2 v}{\partial r} + \frac{\partial}{\partial r}\left(\frac{v}{r}\right) + \frac{\partial^2 v}{\partial z^2}\right] \tag{2.15}$$

$$u\frac{\partial w}{\partial r} + w\frac{\partial w}{\partial z} = -\frac{1}{\rho}\frac{\partial p}{\partial z} + \nu\left[\frac{\partial^2 w}{\partial r^2} + \frac{\partial}{\partial r}\left(\frac{w}{r}\right) + \frac{\partial^2 w}{\partial z^2}\right] \tag{2.16}$$

The functions $F(\zeta)$, $G(\zeta)$, $H(\zeta)$ and $P(\zeta)$ are introduced into the velocity and pressure, where $\zeta = (\Omega/\nu)^2 z$. These are functions purely of z, they do not vary in r. By introducing them into the Navier-Stokes equations they simplify as follows:

$$H' + 2F = 0 \tag{2.17}$$

$$F'' - HF' - F^2 + G^2 = 0 \tag{2.18}$$

$$G'' - HG' - FG'' = 0 \tag{2.19}$$

$$P' - HH' + H'' = 0 \tag{2.20}$$

where $u = r\Omega F$; $v = r\Omega G$; $w = (\nu\Omega)^{1/2}H$; $p =$ - $\rho\nu\Omega P$. The boundary conditions are $G(0) = 1$, $F(0) = H(0) = G(\infty) = F(\infty) = 0$. From equation 2.20, P can be written as a function of H.

$$P(\zeta) = P_0 + 0.5H^2 - H' \tag{2.21}$$

In order to further simplify the problem, equation 2.17 is introduced into equations 2.18 and 2.19 in order to remove the F function. In order to solve these differential equations, a constant must be set as the upper boundary of the H function. Due to the dynamics of the interaction with rotating disc the flow will get pulled downwards. ($H(\infty) = -c$ where $c > 0$).

Cochran [31] suggested that the functions can be estimated using a power series. The variable $\lambda = e^{-c\zeta}$ is introduced and g(λ) and h(λ) are defined as follows:

$$G(\zeta) = c^2 g(\lambda); H(\zeta) = ch(\lambda) - c, \tag{2.22}$$

with the boundary conditions: $c^2 g(1) = h(1) = 1; g(0) = h(0) = h'(1) = 0$. λ varies from 0 to 1 with: $\lambda \to 0$ when $\zeta \to \infty$ and $\lambda = 1$ when $\zeta = 0$. As shown in Benton's paper [30], the $g(\lambda)$ and $h(\lambda)$ functions are be approximated:

$$g(\lambda) = \sum_{i=1}^{n} a_i \lambda^i \tag{2.23}$$

$$h(\lambda) = \sum_{j=i}^{n} b_j \lambda^j \tag{2.24}$$

with n being the number of coefficients used in the calculation. The series converges to within 4 decimal places with 50 coefficients. The a_i and b_j coefficients have the form:

$$a_i = \frac{1}{i(i-1)} \sum_{k=1}^{i-1} (i - 2k) a_k b_{i-k} \tag{2.25}$$

$$b_j = \frac{-1}{2j^2(j-1)} \sum_{k=1}^{j-1} [(j-k)(2j-3k) b_k b_{j-k} + 4 a_k a_{j-k}] \tag{2.26}$$

The first few terms are numerically solved in the paper [30] (which are used to initiate the MATLAB loops), as well as the parameters that have been chosen: a_1 = 1.53678; b_1 = 2.36449; c = 0.88447. Using these parameters returns the desired h and h' at $\lambda = 1$ to five significant figures.

2.3.3 The flow due to a rotating sphere in a free stream

The methods in this section show the theoretical laminar boundary equations of a rotating sphere flow as derived by Lee [32]. The Navier-Stokes equation for a rotating sphere in an axial flow can be written in a non-rotating curvilinear coordinate system (x, y), where x is the distance along the surface from the stagnation point of the sphere and y is the normal distance from the surface. The steady state equations are as follows:

$$\frac{\partial}{\partial x}(ru) + \frac{\partial}{\partial y}(rv) = 0 \tag{2.27}$$

$$u\frac{\partial u}{\partial x} + v\frac{\partial u}{\partial y} - \frac{w^2}{r}\frac{dr}{dx} = U_e \frac{dUe}{dx} + \nu \frac{\partial^2 u}{\partial y^2} \tag{2.28}$$

$$u\frac{\partial w}{\partial x} + v\frac{\partial w}{\partial y} + \frac{uw}{r}\frac{dr}{dx} = \nu \frac{\partial^2 w}{\partial y^2} \tag{2.29}$$

where U_∞ is the free stream velocity, $U_e(x)$ is the velocity of the mainstream at the edge of the boundary layer, $r(x)$ is the cross sectional radius at x, Ω is the

angular velocity of the sphere in rad.s^{-1}, u and v the velocity components in x and y respectively and w the transverse velocity. The boundary conditions are:

$$u = v = 0 \quad w = r\Omega \quad \text{at } y = 0 \tag{2.30}$$
$$v = w = 0 \quad u = U_e \quad \text{at } y \to \infty \tag{2.31}$$

Two new dimensionless variables (ξ, η) can be defined to replace x and y:

$$\xi = \int_0^x \frac{U_e(x)}{U_\infty} \left(\frac{r}{L}\right)^2 \frac{dx}{L} \tag{2.32}$$
$$\eta = \left(\frac{\mathrm{Re}_L}{2\xi}\right)^{1/2} \frac{U_e r y}{U_\infty L^2} \tag{2.33}$$

where L is the characteristic length (eg. the radius), and the Reynolds number $\mathrm{Re}_L = U_\infty L/\nu$. The stream function $\psi(x, y)$ therefore has the following form:

$$\psi(x, y) = U_\infty L \left(\frac{2\xi}{\mathrm{Re}_L}\right)^{1/2} f(\xi, \eta). \tag{2.34}$$

The velocities u and v can now be expressed in terms of $\phi(x, y)$ and furthermore in terms of $f(\xi, \eta)$. Introducing a new variable $\Lambda = (2\xi/U_e)(dU_e/d\xi)$:

$$u = \frac{L}{r}\frac{\partial \psi}{\partial y}, \qquad v = -\frac{L}{r}\frac{\partial \psi}{\partial x} \tag{2.35}$$

$$u = U_e \frac{\partial f}{\partial \eta}, \qquad v = -\frac{r U_e}{L(2\xi \mathrm{Re}_L)^{1/2}} \left[f + 2\xi \frac{\partial f}{\partial \xi} + \left(\Lambda + \frac{2\xi}{r}\frac{dr}{d\xi} - 1\right) \eta \frac{\partial f}{\partial \eta} \right] \tag{2.36}$$

In order to non-dimensionalize the velocity in the transverse direction, the following relation is created:

$$w(x, y) = r(x)\Omega g(\xi, \eta). \tag{2.37}$$

Equations 2.28 and 2.29 can be rewritten by substituting in u and v from equation 2.36:

$$f''' + f f'' + \Lambda(1 - f'^2) + \frac{2\xi}{r}\frac{dr}{d\xi}\left(\frac{r\Omega}{U_e}\right)^2 g^2 = 2\xi \frac{\partial(f', f)}{\partial(\xi, \eta)}, \tag{2.38}$$

$$g'' + f g' - g f' \left(\frac{4\xi}{r}\right)\frac{dr}{d\xi} = 2\xi \frac{\partial(g, f)}{\partial(\xi, \eta)}. \tag{2.39}$$

with the boundary conditions:

$$\begin{aligned} f = f' = 0, g = 1 \quad &\text{for} \quad \eta = 0 \\ f' = 1, g = 0 \quad &\text{for} \quad \eta \to \infty \end{aligned} \tag{2.40}$$

The parameters on the right side of equations 2.38 and 2.39 have the form $\partial(x,y)/\partial(\xi,\eta)$. This type of PDE has the following Jacobian:

$$\frac{\partial(x,y)}{\partial(\xi,\eta)} = \frac{\partial x}{\partial \xi}\frac{\partial y}{\partial \eta} - \frac{\partial y}{\partial \xi}\frac{\partial x}{\partial \eta} \tag{2.41}$$

Chao [33] has determined that f and g can be written as the following series:

$$f(\xi,\eta) = f_0(\Lambda,\eta) + \sum_{i=1}^{n}(2\xi)^i \frac{d^i\Lambda}{d\xi^i} f_i(\Lambda,\eta), \tag{2.42}$$

$$g(\xi,\eta) = f_0(\Lambda,\eta) + \sum_{i=1}^{n}(2\xi)^i \frac{d^i\Lambda}{d\xi^i} g_i(\Lambda,\eta), \tag{2.43}$$

where n is a positive integer. Using $n = 2$, a set of simultaneous partial differential equations [32, equations 25–33] are derived. Because we are working in on sphere certain parameters can be simplified:

$$\left(\frac{r\Omega}{U_e}\right)^2 \frac{2\xi}{r}\frac{dr}{d\xi} = B\Lambda \tag{2.44}$$

$$\frac{4\xi}{r}\frac{dr}{d\xi} = 2\Lambda \tag{2.45}$$

$$\frac{U_e}{U_\infty} = 1.5\sin\beta \tag{2.46}$$

$$\xi = 1 - 1.5cos\beta + 0.5\cos^3\beta \tag{2.47}$$

$$\Lambda = \frac{4\cos\beta - 6\cos^2\beta + 2\cos^4\beta}{3\sin^4\beta} \tag{2.48}$$

$$\frac{d\Lambda}{d\xi} = -\frac{8(1-\cos\beta)^3)}{9\sin^8\beta} \tag{2.49}$$

$$\frac{d^2\Lambda}{d\xi^2} = \frac{-16}{27\sin^1 2\beta}(1-\cos\beta)^3(3-5\cos\beta) \tag{2.50}$$

where $\beta = x/R$

Chapter 3

Methods

This chapter outlines the mathematical model developed for the systems researched, followed by the methods used to produce the computational and experimental data. Two designs utilizing the Coanda effect have been explored in depth. The traditional design, seen in figure 3.1, has already been investigated by Naudin [1] and Aesir [34] in recent years. The novel design being investigated, seen in figure 3.2, may have certain control advantages that will discussed in detail. The computational model will first be validated against known flow regimes. The method used to generate the lift and moment measurements will be stated, along with a detailed description of the experimental setup.

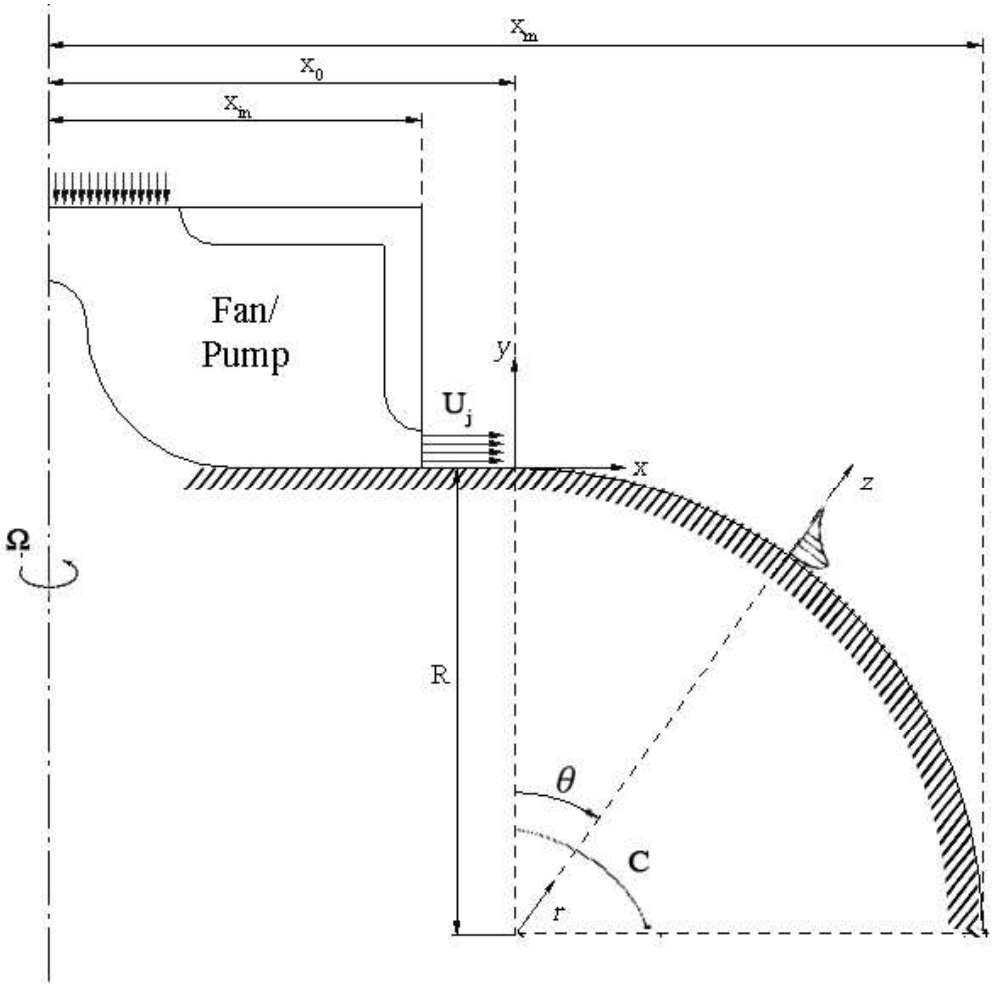

Figure 3.1: Notation of traditional design in 2D

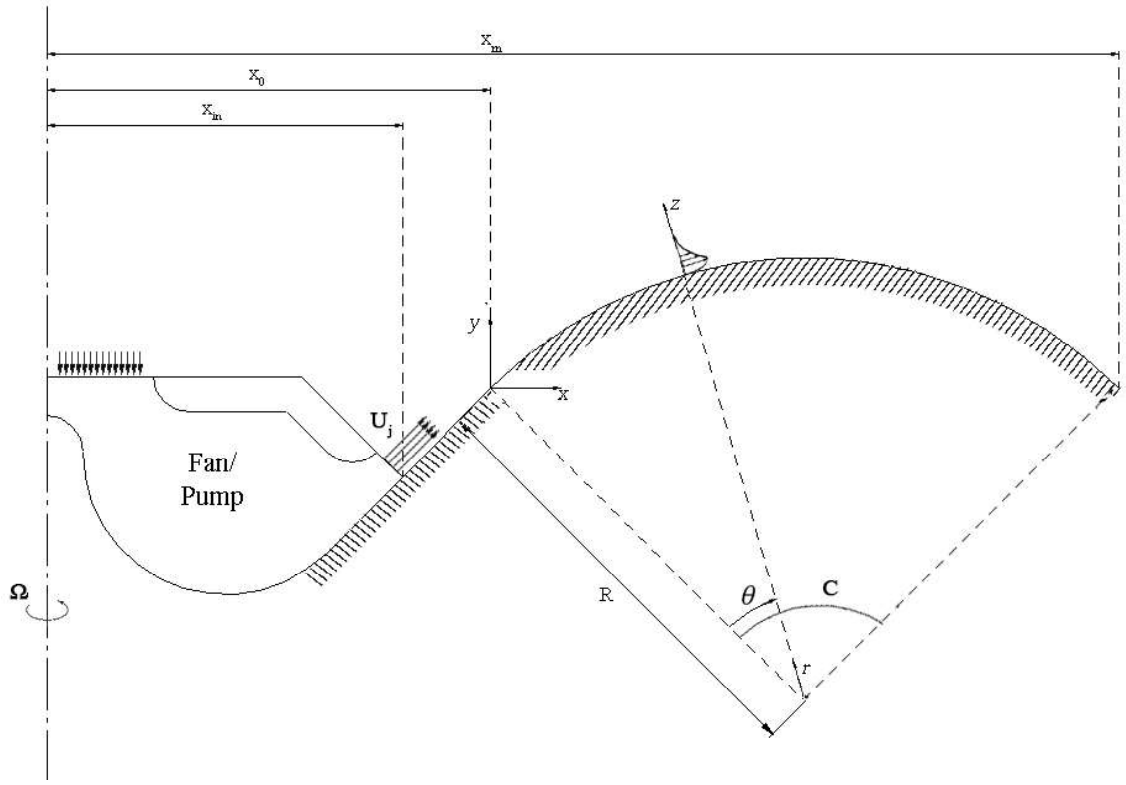

Figure 3.2: Notation of novel design in 2D

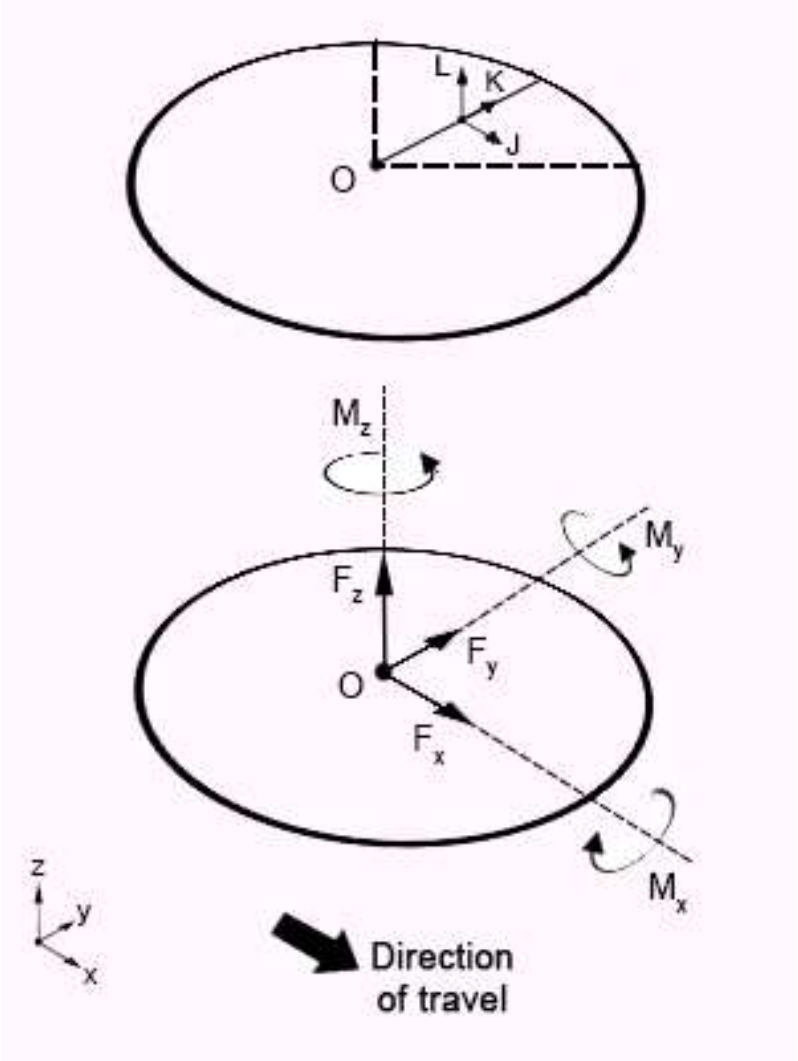

Figure 3.3: Free body diagram showing the notations and coordinate system in 3D.

In three dimensions, the coordinates and forces acting on the system are shown in figure 3.3. Furthermore, the force notation when acting on a single section of the disk is also present. L is used to signify general lift (F_z) in the results section, the torque T is represented by M_z.

3.1 Mathematical models

Two physical models of the designs need to be considered: the aerodynamic and physical models. The first will look at the generation of forces by the flow regime studied. The second will look at the equations required to manipulate the forces in a

controlled manner. In order to begin defining these models some general parameters need to be defined. the first of which is the curvature C in rad. Secondly the aspect ratio AR using the following equation:

$$\mathrm{AR} = x_m/x_0. \tag{3.1}$$

The configuration studied is $C = \pi/4$ and $\mathrm{AR} = 2$. The jet velocity produced by the fan will be referred to as U_j, the disk rotation in the γ axis is referred to as Ω, $\bar{x}$ is the mean distance from the centre. In cases studied the flow regime is mainly influenced by the jet velocity, the Reynolds number can therefore be defined as follows:

$$\mathrm{Re} = \frac{U_j(x_0 - x_m)}{\nu}, \tag{3.2}$$

where ν is kinematic viscosity. The combined velocity of jet and spin at mid chord is defined as U_d it is calculated in 3D using the following equation:

$$U_d = \sqrt{(2\pi\bar{x}\Omega)^2 + (\frac{x_{in}}{\bar{x}}U_j)^2} \tag{3.3}$$

It is derived by using taking the ratio of the disk rotations linear component at $\bar{x}$ $(2\pi\bar{x}\Omega)$ over the jet velocity at that position $(\frac{x_{in}}{\bar{x}}U_j)$. The rotation parameter B is used to determine the ratio of spin added win relation to the jet velocity. Using the mean distance from the centre $\bar{x}$, it can be calculated using the following equation:

$$B = \frac{2\pi\bar{x}\Omega}{U_d}, \tag{3.4}$$

It is derived by determining the ratio of th pin at mid chord to total velocity. The lift coefficient can be calculated using the following equation:

$$c_L = \frac{L}{0.5\rho U_j^2 S_c}. \tag{3.5}$$

where ρ is the air density and S_c is the cross sectional area.

3.1.0.1 Dynamic model

The forces and moments are incorporated into a dynamic system using the following equations.

$$\ddot{x} = \frac{F_x}{m}, \qquad \dot{\alpha} = \frac{M_y}{L_T}, \tag{3.6}$$

$$\ddot{y} = \frac{F_y}{m}, \qquad \dot{\beta} = \frac{M_x}{L_T}, \tag{3.7}$$

$$\ddot{z} = \frac{F_z}{m} - g, \qquad \ddot{\gamma} = \frac{M_z}{I_z}, \tag{3.8}$$

where L_T is the total spin angular momentum in the system as can be calculated by the following equation,

$$L_T = I_D\Omega_D - I_C\Omega_C, \tag{3.9}$$

where $_D$ is the disk and $_C$ is the compressor. They are spinning in opposite directions and the same torque is applied maintain yaw attitude. Each spinning object will attempt to precess in its favoured direction. Assuming both parts have different angular momentum, controlled rotation can be achieved through precession. If L_T = 0, then the system would behave as if it were not spinning, as the gyroscopic effects would cancel out. In this case these corrections are made to equations 3.6 and 3.7:

$$\ddot{\alpha} = \frac{M_x}{I_x}, \tag{3.10}$$

$$\ddot{\beta} = \frac{M_y}{I_y}. \tag{3.11}$$

However, in order to have a static yaw position, torques generated by both parts must counteract. M_z can therefore be calculated using the following equation:

$$M_z = T_D - T_C. \tag{3.12}$$

The angular positions α, β and γ represent the roll, pitch and yaw. Lateral forces (F_x, F_y) occur with control actions. They are due to a change in c_p as was seen in the previous section. Their order of magnitude is computationally measured to be $10^{-4}Nm$ for a disk with an eternal radius of 300 mm. Assuming the side forces to be negligible, forces acting in the global coordinate frame can therefore be simplified to the following equations. This assumption can be made due to measured results later shown.

$$F_x = \sin(\beta)\cos(\gamma)L, \tag{3.13}$$

$$F_y = \sin(\alpha)\cos(\gamma)L, \tag{3.14}$$

$$F_z = \cos(\alpha)\cos(\beta)L. \tag{3.15}$$

3.1.1 Aerodynamic model

For any given sheet of material the pressure difference between the top and bottom surfaces will generate a force in the direction of area with lowest pressure. In order

to determine the vertical force applied to a horizontal sheet the following equation is used:

$$L = \int p_l dA - \int p_u dA. \tag{3.16}$$

In the case of a curved surface the force would be acting at an angle. In order to account for this, the following changes can be made.

$$L = \int p_l \cos(\bar{\theta}) d\theta - \int p_u \cos(\bar{\theta}) d\theta, \tag{3.17}$$

where $\bar{\theta}$ is the curvature deflection from the horizontal plane. $\bar{\theta} = \theta$ for the traditional and $\bar{\theta} = \theta - \pi/4$ for the novel design. Horizontal force components can also be described using the same premise:

$$F_{XY} = \int p_l \sin(\bar{\theta}) d\theta - \int p_u \sin(\bar{\theta}) d\theta. \tag{3.18}$$

The is force generated at the point θ_p where we have the following condition:

$$\int_0^{\theta_p} p_l d\theta - \int_0^{\theta_p} p_u d\theta = \frac{\int_0^{\pi/2} p_l d\theta - \int_0^{\pi/2} p_u d\theta}{2}. \tag{3.19}$$

As can be seen in figure 3.4, the lift can only be smaller than or equal to the surface force. In the traditional design, the lift is maximum when the centre of pressure is at $\theta = 0$ or $x_p = x_0$. In the second case, the maximum lift is obtained at a centre of pressure position $\theta = \pi/4$. These are the positions where the force vector would be vertical. The lift vector (L_c) magnitude and traditional and novel distances (x_p) respectively can be calculated using the following equations:

$$L_c = F_c \cos \bar{\theta}, \tag{3.20}$$

$$x_p = R \sin \bar{\theta} + x_0, \tag{3.21}$$

$$x_p = R \sin \bar{\theta} + (x_0 + x_m)/2, \tag{3.22}$$

where $\bar{\theta} = \theta$ (for traditional) and $\bar{\theta} = \theta - \pi/4$ (for novel).

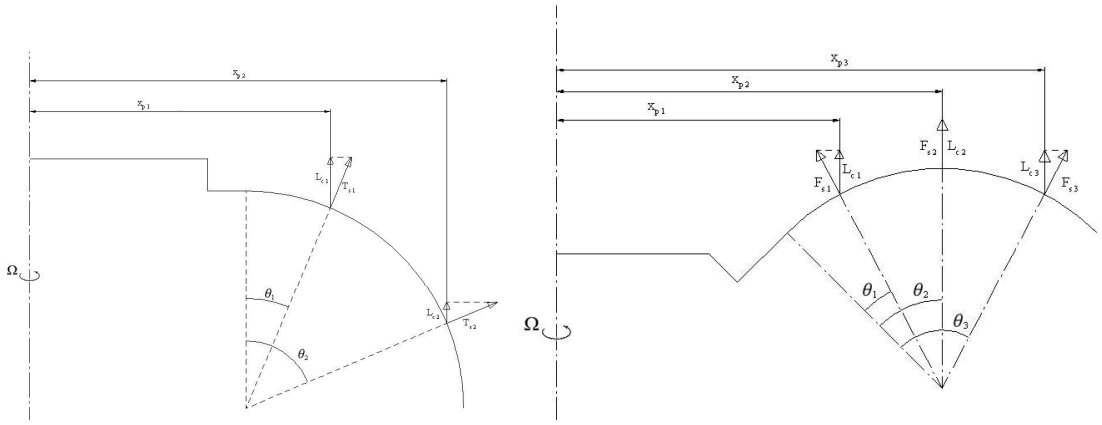

(a) Traditional design (b) Novel design

Figure 3.4: Positions of the centre of pressure and force vectors

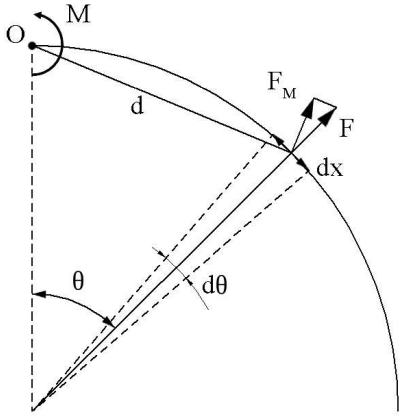

Figure 3.5: Moment diagram of a section of the surface.

In order to determine the centre of lift shown in figures 3.4a and 3.4b, the pressure distribution of the top and bottom surface must be integrated with respect to θ. The data that has been collected from the computational model is plotted against the x axis. As there is a thickness to the surface, let R_l and R_t be the radius of curvature for the bottom and top surface respectively.

$$\theta = \sin^{-1}((x - x_0)/R) \tag{3.23}$$

where $R = R_l$ or R_u. A trapezoidal integration of the top and bottom pressure is used to determine the total force acting on the chord (F):

$$F_c = R_l \int_0^{\pi/2} P_l \, d\theta - R_u \int_0^{\pi/2} P_u \, d\theta \tag{3.24}$$

Let us take the moment (M) about (O), in figure 3.5, due to a force (F) acting on a flat plate of length dx with a lever arm length d. If $d\theta$ is small enough, the total moment about O due to the pressure difference is the sum of the moments of individual sections. The centre of pressure of the curved surface is located at $\theta = \theta_p$, so that: $2\sum_0^{\theta_p} M = \sum_0^{\pi/2} M$. Using the trapezoidal method, the local force F at each data point is calculated. The lever arm (d) and normal force (F_m) are calculated using the following equations. The moments of forces acting on each of the data points are summed together starting at $\theta = 0$.

$$d = 2R\sin(\theta/2), \tag{3.25}$$

$$F_m = F_c \sin\frac{\pi/2 - \theta}{2}. \tag{3.26}$$

Using these the lever arm and force about the moment about O for any point on the surface can be rewritten as:

$$M = -2RF_c\sqrt{2}\sin\theta. \tag{3.27}$$

3.1.2 Control model

This section outlines the mathematical tools used to describe the system from a control aspect. The designs are sectioned into four as seen in figure 3.6b. The centre of pressure's radial distance can be varied within a section by actuating a flap seen in figure 3.6a. These changes generate moments which are used to pitch and roll the system controllably.

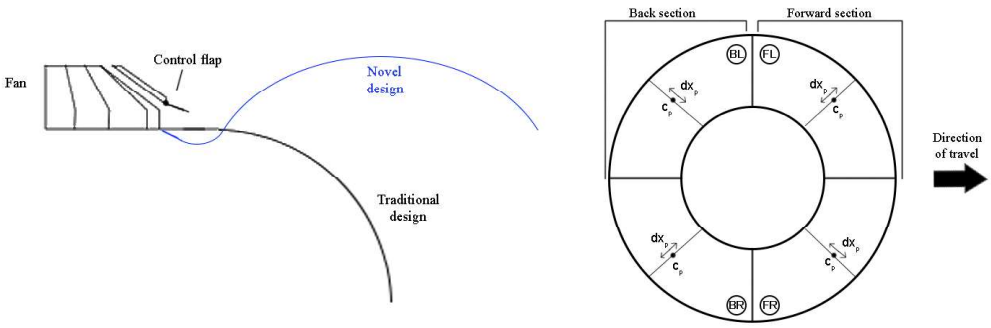

(a) Side section of both designs showing the control flap position.

(b) Top view of control areas in a 4 section system.

Figure 3.6: Control implementation.

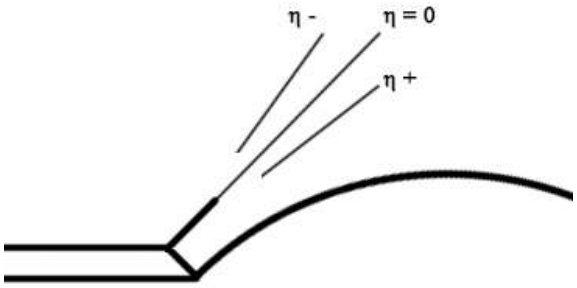

Figure 3.7: Close up digram of the control flap and direction of η.

3.1.2.1 Static flight

Traditional design

In order to calculate the moments in figure 3.6b, the moments of individual sections are calculated. The diagram in figure 3.8 shows the BL-FR or BR-FL sections of the craft. They are the opposing section pairs. At rest, the following relationships are satisfied:

$$L = F\cos\theta_p \tag{3.28}$$
$$K = F\sin\theta_p \tag{3.29}$$
$$M = y_pK - x_pL \tag{3.30}$$

Where $y_p = -R[1-\cos(\theta_p)]$ and $x_p = x_0 + R\sin(\theta_p)$. The moment in the front section is negative and positive in the back (taken clockwise from the centre of mass c_m). In stationary flight all the moments get cancelled out. When the flap is deflected, θ changes by $\Delta\theta_p$. In the front section, $\Delta\theta_p > 0$, and in the back, $-\Delta\theta_p$. The moments in forward flight initiation are:

$$L_F = F\cos(\theta_p + \Delta\theta_p) \quad L_B = F\cos(\theta_p - \Delta\theta_p) \tag{3.31}$$
$$K_F = F\sin(\theta_p + \Delta\theta_p) \quad K_B = F\sin(\theta_p - \Delta\theta_p) \tag{3.32}$$
$$M_F = -y_{pF}R_F - x_{pF}L_F \quad M_B = y_{pB}R_B + x_{pB}L_B \tag{3.33}$$

with,

$$y_{pF} = R[1-\cos(\theta_p + \Delta\theta_p)] \quad x_{pF} = x_0 + R\sin(\theta_p + \Delta\theta_p) \tag{3.34}$$
$$y_{pB} = R[1-\cos(\theta_p - \Delta\theta_p)] \quad x_{pB} = x_0 + R\sin(\theta_p - \Delta\theta_p) \tag{3.35}$$

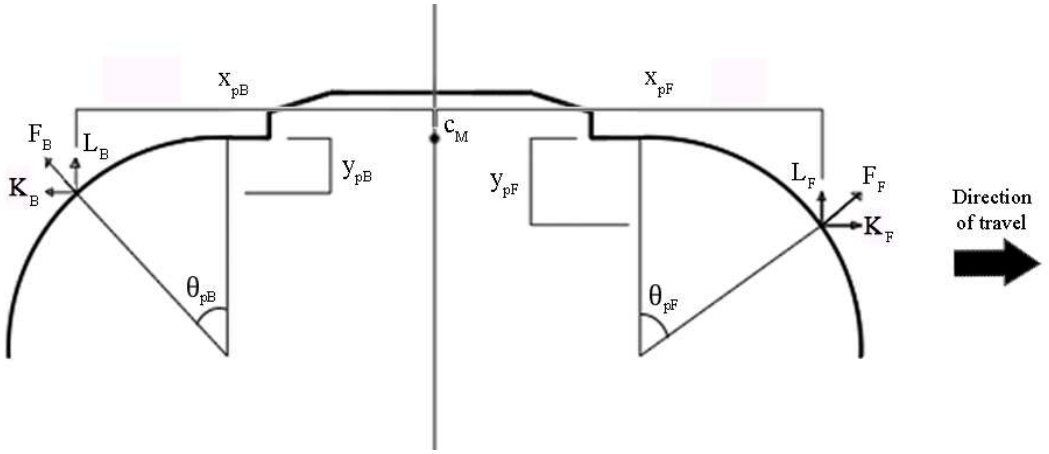

Figure 3.8: Force vectors with active control system initiating forward flight.

By substituting the position and force equations into the moment equation and simplifying we get:

$$M_F = -F\{x_0\cos(\theta_p + \Delta\theta_p) + R[2\sin(\theta_p + \Delta\theta_p)\sin^2\frac{\theta_p - \Delta\theta_p}{2} + ... \\ \frac{1}{2}\sin(\theta_p + \Delta\theta_p)]\} \quad (3.36)$$

$$M_B = F\{x_0\cos(\theta_p - \Delta\theta_p) + R[2\sin(\theta_p - \Delta\theta_p)\sin^2\frac{\theta_p + \Delta\theta_p}{2} + ... \\ \frac{1}{2}\sin(\theta_p - \Delta\theta_p)]\} \quad (3.37)$$

Let section FR-BL be named *Rd* (right diagonal), and FL-BR named *Ld*. The moments in a section $M_{Ld} = M_{Rd} = M_B + M_F$. By using the equations previously derived, the total moment equation is written:

$$M = F\left(2x_0\sin\theta_p\sin\Delta\theta_p + 2R\Lambda\right), \quad (3.38)$$

where,

$$\Lambda = \sin(\Delta\theta_p)\left[\cos\Delta\theta_p(2\sin^2\theta_p + 1) - 2\cos^2\theta_p\cos\Delta\theta_p - \cos\theta_p\right] \quad (3.39)$$

The resultant forces in the *Ld*-*Rd* planes are the lift, $L = 2F\cos(\theta_p)\cos(\Delta\theta_p)$, and the horizontal component $K = 2F\sin(\Delta\theta_p)\cos(\theta_p)$. For nose down pitch, the resultant K acts as "aerodynamic thrust". In a body fixed coordinate frame, we can therefore define the moments and forces acting on the aircraft. The total pitching moment on the aircraft, with no roll, is obtained by the following equation:

$$M_y = (M_{Ld} + M_{Rd})\cos\pi/4 = 2M_{Ld}\cos\pi/4. \quad (3.40)$$

In order to determine the rolling moment equations, let us assume, $M_{Ld} \neq M_{Rd}$. We can use the same reasoning as for the forward flight moments, but with direction of travel being the turn direction.

$$M_x = (M_{Ld} - M_{Rd}) \sin \pi/4, \tag{3.41}$$

with $M_{Rd} > 0$ for a left turn and $M_{Rd} < 0$ for a right turn. The resultant forces K, J, L in the x, y, and z directions respectively are the aerodynamic thrust, side force, and lift. They can be calculated using the following equations:

$$F_z = L_{Rd} + L_{Ld}, \tag{3.42}$$

$$F_x = \frac{1}{\sqrt{2}}(K_{Rd} + K_{Ld}), \tag{3.43}$$

$$F_y = \frac{1}{\sqrt{2}}(K_{Ld} - K_{Rd}), \tag{3.44}$$

with $J < 0$ going right and $J > 0$ going left. Note, in normal forward flight there is aerodynamic thrust. The main component generating forward motion is the redirected lift vector due to an angle of attack created by the moments.

Novel design

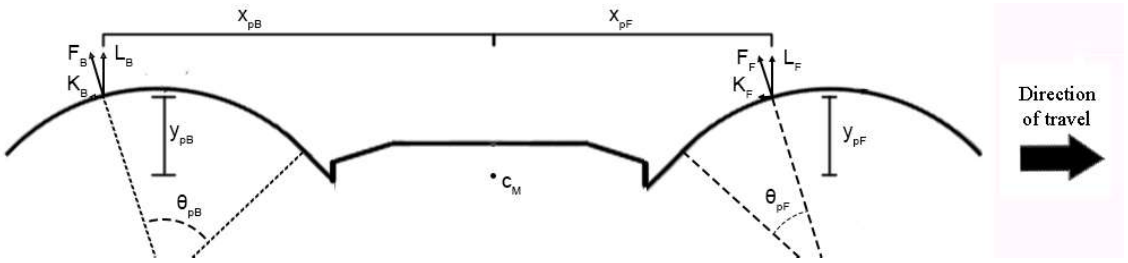

Figure 3.9: Force vectors with active control system initiating forward flight for the novel design.

The moment and force equations for a section of the novel design, during static flight, are as follows:

$$L = F \cos \bar{\theta}_p, \tag{3.45}$$

$$K = F \sin \bar{\theta}_p, \tag{3.46}$$

$$M = y_p K - x_p L \tag{3.47}$$

where,

$$y_p = R[\cos \bar{\theta}_p - \cos \pi/4], \tag{3.48}$$

$$x_p = x_0 + R[\sin \pi/4 + \sin \bar{\theta}_p], \tag{3.49}$$

and $\bar{\theta_p} = \theta_p - \pi/4$. In ideal conditions, the force vector is vertical and the lift is maximal, $\theta_p = \pi/4$, $R = 0$ and $L = F$.

$$M = F\left[x_0 + 2R\sin(\pi/4)\right]. \tag{3.50}$$

In ideal conditions, the flap deflection changes the centre of pressure position $\theta_p = \pi/4 \pm \Delta\theta_p$; $\bar{\theta_p} = \pm\Delta\theta_p$. The equations of force and moments on the front and back sections are as follows:

$$L_F = F\cos\Delta\theta_p, \qquad L_B = F\cos -\Delta\theta_p, \tag{3.51}$$

$$K_F = F\sin\Delta\theta_p, \qquad K_B = F\sin -\Delta\theta_p, \tag{3.52}$$

$$M_F = y_{pF}R_F - x_{pF}L_F, \quad M_B = -y_{pB}R_B + x_{pB}L_B, \tag{3.53}$$

with,

$$y_{pF} = R[\cos\Delta\theta_p)\cos\pi/4], \qquad y_{pB} = R[\cos -\Delta\theta_p - \cos\pi/4], \tag{3.54}$$

$$x_{pF} = x_0 + R[\sin\pi/4 + \sin\Delta\theta_p], \quad x_{pB} = x_0 + R[\sin\pi/4 + \sin -\Delta\theta_p]. \tag{3.55}$$

The resultant forces L and R in the Ld and Rd planes are as follows (where $R > 0$ means forward lift):

$$L = 2F\cos\Delta\theta_p \quad K = 2F\sin\Delta\theta_p. \tag{3.56}$$

By substituting the position into the moment equations and then adding the back and front moments together we get:

$$\begin{aligned} M_F = -Fx_0\cos(\Delta\theta_p) + FR\{&\cos(\Delta\theta_p)(\cos(\Delta\theta_p) - 2^{-1/2})... \\ &- \sin(\Delta\theta_p)[2^{-1/2} + \sin(\Delta\theta_p)]\}, \end{aligned} \tag{3.57}$$

$$\begin{aligned} M_B = Fx_0\cos(-\Delta\theta_p) - FR\{&\cos(-\Delta\theta_p)(\cos(-\Delta\theta_p) - 2^{-1/2})... \\ &- \sin(-\Delta\theta_p)[2^{-1/2} + \sin(-\Delta\theta_p)]\}, \end{aligned} \tag{3.58}$$

$$M_{Ld} = M_{Rd} = -2^{1/2}\sin(\Delta\theta_p)RF. \tag{3.59}$$

The diagonal moment resulting from a deflection similar to the one necessary for forward flight in the traditional design is negative, therefore the craft will pitch in the opposite direction. However, both reaction vectors would be in the direction of flight. Further research is required to determine whether the reaction force will provide a considerable amount of "forward lift". It could potentially be used for rapidly changing directions, as the force would act before the craft tilted. For further calculation, the deflections on front and back sections will be reversed. $M_{Ld} = M_{Rd} = 2^{1/2}RF\sin\Delta\theta_p$. In order to calculate the pitch and roll moments, the following equations are used:

$$M_y = 2^{-1/2}(M_{Ld} + M_{Rd}) = RF(\sin\Delta\theta_{pLd} + \sin\Delta\theta_{pRd}) \tag{3.60}$$

$$M_x = 2^{-1/2}(M_{Ld} - M_{Rd}) = RF(\sin\Delta\theta_{pLd} - \sin\Delta\theta_{pRd}) \tag{3.61}$$

In order to add a roll component, the change in position ($\Delta\theta_p$) needs to be different for each diagonal. If $\delta\theta_{pRd} > \delta\theta_{pLd}$ the craft turns right, and left if $\delta\theta_{pRd} < \delta\theta_{pLd}$. The resultant area forces of two opposing sections L, K, and system-wide forces F in a reversed control system as previously stated are as follows:

$$L = 2F\cos\Delta\theta_p, \tag{3.62}$$
$$K = -2F\sin\Delta\theta_p, \tag{3.63}$$
$$F_z = L_{Rd} + L_{Ld}, \tag{3.64}$$
$$F_x = \frac{1}{\sqrt{2}}(K_{Ld} + K_{Rd}), \tag{3.65}$$
$$F_y = \frac{1}{\sqrt{2}}(K_{Ld} - K_{Rd}). \tag{3.66}$$

Alternatively we can take the case, $\theta_p = \pi/4 + \Delta\theta_p$. Then $\bar{\theta_p} - \Delta\theta_p = 0$ for the back section, and $2\Delta\theta_p$ for the front. The equations of force and moments are as follows:

$$L_F = F\cos(2\Delta\theta_p), \qquad L_B = F, \tag{3.67}$$
$$K_F = F\sin(2\Delta\theta_p), \qquad K_B = 0, \tag{3.68}$$
$$M_F = y_{pF}K_F - x_{pF}L_F, \quad M_B = x_{pB}L_B, \tag{3.69}$$

with,

$$y_{pF} = R[\cos(2\Delta\theta_p) - \cos(\pi/4)], \quad y_{pB} = R[1 - \cos(\pi/4)], \tag{3.70}$$
$$x_{pF} = x_0 + R[\sin(\pi/4) + \sin(2\Delta\theta_p)], \quad x_{pB} = x_0 + R\sin(\pi/4). \tag{3.71}$$

The total moment in a section (M_{Rd}/M_{Ld}) is given by the following expression:

$$M_B = F\left(x_0 + \frac{R}{\sqrt{2}}\right), \tag{3.72}$$
$$M_F = -F\{x_0\cos(2\Delta\theta_p) + \frac{R}{\sqrt{2}}[\cos(2\Delta\theta_p) + \sin(2\Delta\theta_p)]\}, \tag{3.73}$$
$$M_{Ld} = M_{Rd} = F\{2x_0\sin^2(\Delta\theta_p) + \frac{R}{\sqrt{2}}[1 - \cos(2\Delta\theta_p) - \sin(2\Delta\theta_p)]\}. \tag{3.74}$$

The resulting pitch (M_y) and roll (M_x) moments can therefore be derived.

$$M_y = \frac{1}{\sqrt{2}}(M_{Ld} + M_{Rd}), \quad M_x = \tfrac{1}{\sqrt{2}}(M_{Ld} - M_{Rd}). \tag{3.75}$$

If $M_{Ld} = M_{Rd}$, in pure pitching, the moment can be simplified. $M_x = 0$.

$$M_y = \frac{F}{\sqrt{2}}\left[4x_0\sin^2(\Delta\theta_p) - 4R\sin(\pi/4 - \Delta\theta_p)\sin(\Delta\theta_p)\right]. \tag{3.76}$$

Expansion to more control surfaces

The number of control surfaces used can be increased for better control. In order to find the moments involved at n control surfaces per section, let us take a FL as seen in figure 3.6b. The section is divided equally into n subsections with each section numbered symmetrically to figure 3.10 (with $n = 1$ being the normal section to the direction of flight). The force acting on a certain subsection can be calculated using

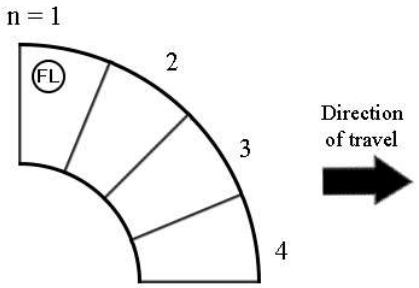

Figure 3.10: Diagram of expansion notation on the FL section.

the following equation:

$$F = \frac{F_c x_p \pi}{2n} \tag{3.77}$$

The moments can be resolved in the Ld_n and Rd_n planes as previously. Using the $2n$ diagonal moments and forces the total pitching and rolling moment are calculated.

$$M_y = \sum_{i=1}^{n} (M_{Ld} + M_{Rd})_i \cos \Gamma_i, \tag{3.78}$$

$$M_x = \sum_{i=1}^{n} (M_{Ld} - M_{Rd})_i \sin \Gamma_i, \tag{3.79}$$

with, $\Gamma_i = (1-i)\pi/2n + \pi/4$. The thrust and side forces can can be calculated using the following equations:

$$F_x = \sum_{i=1}^{n} (R_{Ld} + R_{Rd})_i \sin \Gamma_i, \tag{3.80}$$

$$F_y = \sum_{i=1}^{n} (R_{Ld} - R_{Rd})_i \cos \Gamma_i. \tag{3.81}$$

$$\tag{3.82}$$

Making n very big will return accurate moment values for a realistic gradual centre of pressure position x_p variation between sections. Assuming θ_p and F_c are not

constant within a section, we have the following relationship for $\lim_{n\to\infty}$:

$$M_y = \sum_{i=1}^{n}(M_{Ld} + M_{Rd})_i \cos\Gamma(i) = \int_{\gamma=0}^{2\pi} F_c x_p \cos(\gamma)\, d\gamma, \tag{3.83}$$

$$M_x = \sum_{i=1}^{n}(M_{Ld} - M_{Rd})_i \sin\Gamma(i) = \int_{\gamma=0}^{2\pi} F_c x_p \sin(\gamma)\, d\gamma, \tag{3.84}$$

with $\gamma = 0$ in flight direction, $\pi/2$ normal to flight (left), π opposite to flight, and $3\pi/2$ normal to flight in the right direction.

3.2 CFD analysis

Settings used in the computational fluid dynamics model used were tested against similar flow regimes with known results. After describing the validation process this section will show the different computational and design models that were investigated.

3.2.1 Validation

In order to validate the computational method used, three test cases are chosen: flow over a curved surface, from over a rotating flat plate, and axial flow over a spinning sphere. Each analytical solution from chapter 2 is then compared to the appropriate computational model.

3.2.1.1 Jet over a curved surface

CFD analysis is conducted in ANSYS. In order to compare the numerical and computational methods, the following parameters are set: $R = 1m$; $b = 0.01m$; $U_j = 0.3\ m/s$. These parameters were chosen to be within the range of the mathematical model. The mesh shown below in figure 3.11 is generated using an inflation algorithm on the curved surface. This is used to insure that the finest meshing is done where the change in velocity is greatest. The growth ratio (R_G) and maximum thickness(t_{max}) of the inflation directly influence the accuracy of the results. In this particular case, the inflation parameters are number of layers, n_L= 100, t_{max} = 0.5m (greater than the slot height in order to ensure the totality of the jet boundary layer is modelled). The maximum distance from the surface calculated in MATLAB is 0.210m and R_G= 1.08 using the method described in section 2.3.1.

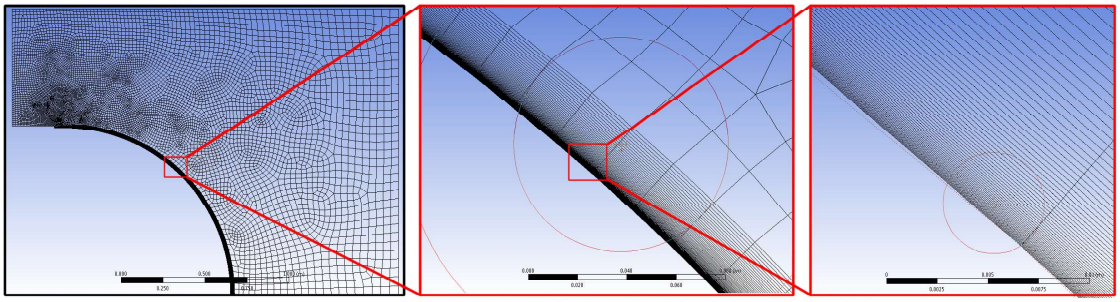

Figure 3.11: Mesh used in Coanda jet simulation, showing under different magnifications the inflation process (t_{max}=0.025, $R_G = 1.05$, $n_L = 75$)

From the analytical model in section 2.3.1 we can calculate the maximum normal distance from the surface modelled numerically, which in this case is 0.1308m. A normal to the surface is drawn on the CFD post processing program of that length. The horizontal and vertical components of velocity are plotted against x and subsequently exported to MATLAB to be processed and compared.

In figure 3.12, it can be seen that the velocity profiles are similar but do not quite match up. The computational results are "stretched out"compared to the theoretical. It is most probably due to the first layer height of the inflation in the mesh. By changing the mesh size, the velocity profiles shrink and expand relative to one another.

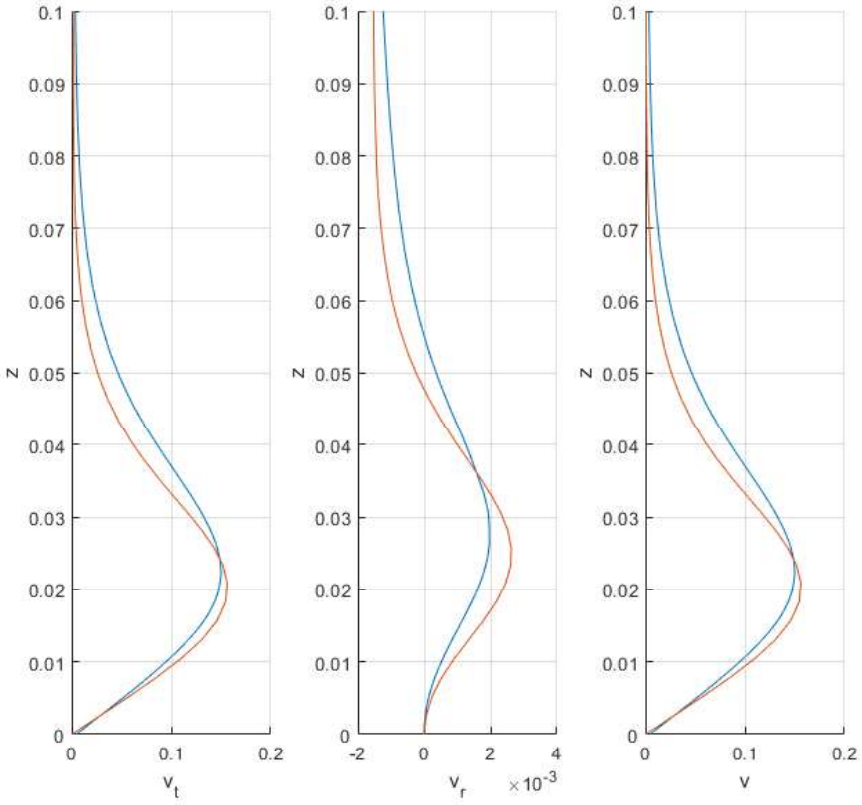

Figure 3.12: Theoretical (blue) and computational (red) tangential (v_t), radial (v_r) and total velocities (v) against distance from surface (y).

3.2.1.2 Rotating flat plate

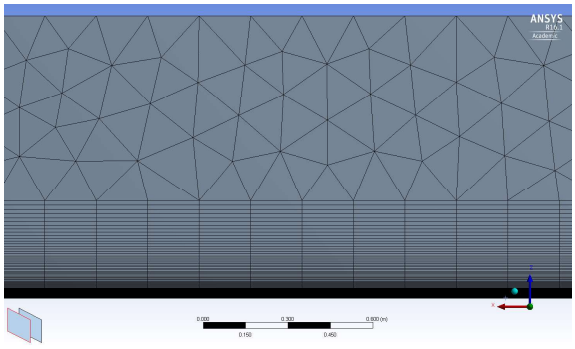

Figure 3.13: Geometry of the mesh parameter shown in the flat plate configuration.

In order to accurately model the swirling boundary layer flow over a flat plate an inflation algorithm, such as in the Coanda case, is used in the meshing process as shown in figure 3.13. The mesh does not need to be fine away from the rotating surface, as the boundary layer in this system is very small. The bottom surface is subject to a rotation of 10 rev.s^{-1} while the other boundaries are simply zero pressure gradient boundary conditions.

As shown in figure 3.14, the experimental and theoretical results for the tangential and radial velocities match up very closely. The theoretical and computational values of v however seem to have a slight offset. The theoretical and computational profiles for this case are much more similar than for the other cases; it is probably due to the simplicity of the problem and mesh. The results formed by these setting are within an acceptable range of the analytical model

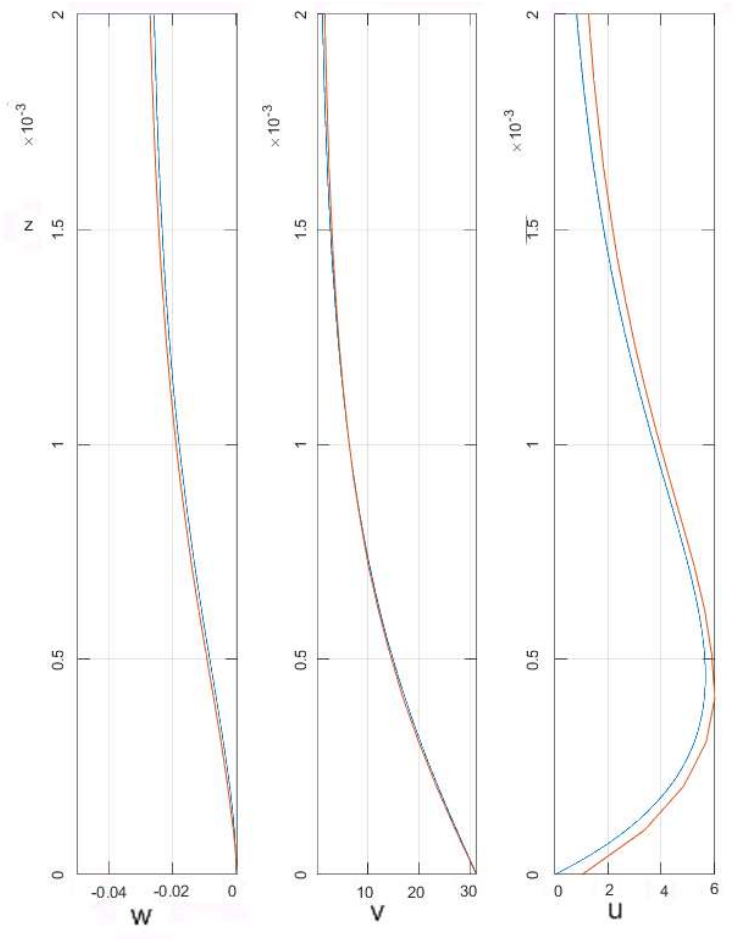

Figure 3.14: Comparison of theoretical (blue) and computational (red) velocity profiles.

3.2.1.3 Rotating sphere in axial flow

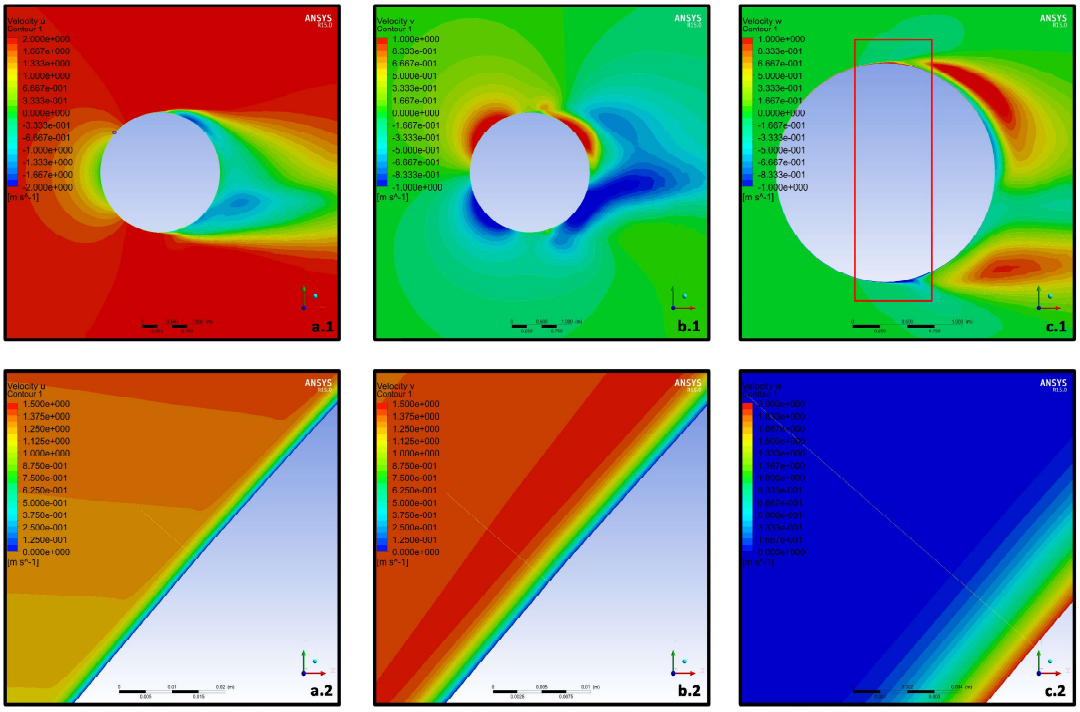

Figure 3.15: The x, y, and z velocity components (a, b and c respectively) are shown from a general perspective (1) and on the boundary layer level (2). The free stream velocity is 1 m.s^{-1}

The computational modelling for the case of a rotating sphere in an axial flow is done similarly to the other two cases. An inflation algorithm is used on the surface in order to assure the formation of the boundary layer. The sphere's surface is set up as a wall boundary with an angular velocity of 1 Hz axially aligned with the free stream flow. The red box in figure 3.15 shows the range at which the flow would begin to become turbulent. The very small blue box in a.1, represents the frame of a.2. The yellow line in all the close images is the range of points at which data is exported to be compared with the theoretical results (the line is of constant length). As is clearly shown in the closer images, the boundary layer is successfully formed.

As opposed to the Coanda case, the velocity profiles computationally measured are shrunken on the y in comparison to theoretical values. It looks as if there has been a very large increase in the rotation parameter. This is not a one time occurrence, the computational and theoretical velocity profiles of this case do not match, it might be due to the CFD not properly modelling the upstream flow.

The modelled area's size may be too small and the rotating disk area of influence surpasses the upstream boundary. Changing the mesh might adversely affect its performance. Furthermore, the computational transverse velocity curve reaches its limit at a negative number (the limit should be 0).

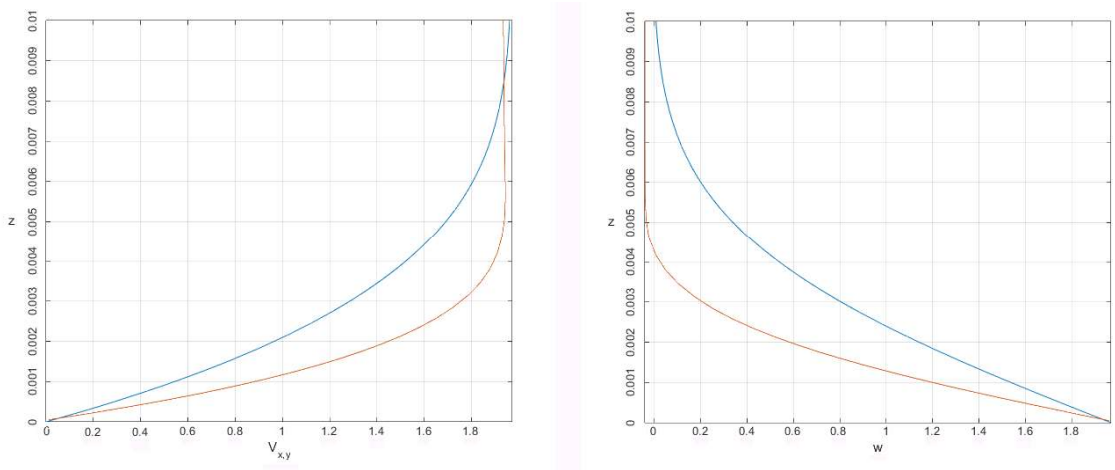

Figure 3.16: Theoretical (blue) and computational (red) total velocity in the x, y plane ($V_{x,y}$) and the transverse velocity (w) against the distance from the surface (z). Calculation made at $\theta = \pi/4$

3.2.2 Designs and measurements

3.2.2.1 Design choices

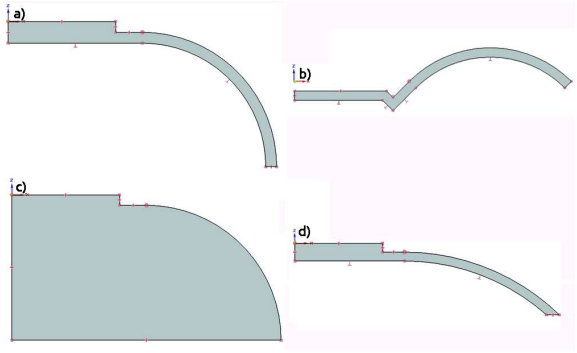

Figure 3.17: a) traditional; b) novel; c) flat bottom; d) half span

The first design investigations that were conducted in ANSYS were used to determine the optimal geometric properties between the given choices (shown in figure 3.17). The first of these designs is the traditional design used in already existing UAVs. The second is identical with a flat bottom to determine how much the under geometry is affecting lift. The third spans only $\pi/4$ in an attempt to eliminate separation due to equatorial eruption [35] experienced by the traditional design at the edge of the disk. The last design has a $\pi/2$ span but the input jet is pointed upwards at $\pi/4$. This investigation seeks to determine the which of these four designs would be best suited for a rotating application.

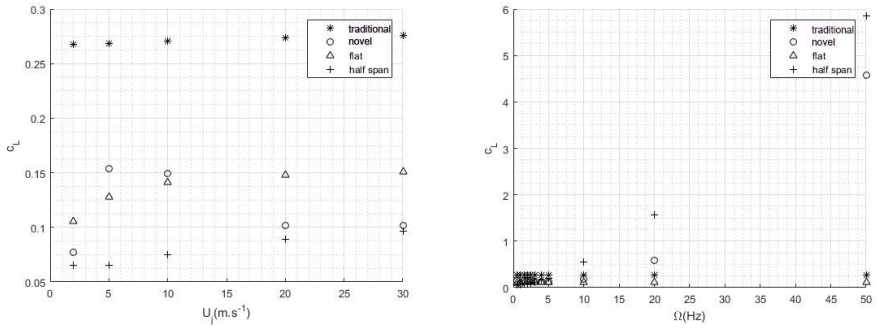

(a) $\Omega = 1$ Hz (b) $U_j = 2$ m.s^{-1}

Figure 3.18: Comparison of the lift coefficients of different designs

ANSYS workbench was used to model the flow for each of the geometries, with varying input jet velocities for $\Omega = 1$ Hz and varying angular velocities for $U_j =$

0.5 and 2 $m.s^{-1}$. BSL EARSM was chosen as a turbulence model as it is the most accurate turbulence model [29] (it is the closest to $k-\omega$ SST model referred to in previous experiments [29]). It is used to determine the stability of each design under both jet and angular velocity inputs. The lift coefficient is calculated using equations from the previous section. Resulting lift coefficient is shown in figure 3.18.

Figure 3.18a shows that the lift coefficient produced by the traditional and flat bottomed designs are higher than for the novel and half span ones. The reason for this is a higher deflection of thrust by the surface downwards, bringing it closer to a fully vertical flow when leaving the surface. However, with a higher rotational component, shown in figure 3.18b, the novel and half span designs start to see a higher coefficient. This is due to the traditional design being adversely affected due to the separation of flow at the equatorial region, a phenomenon called eruption [35]. This happens in the equatorial region, when the centrifugal forces acting on the fluid cause separation and radial ejection.

3.2.2.2 Simulation settings

This section describes the settings used in ANSYS CFX to generate the detailed computational models. These models are later used to determine the boundary layer's behaviour and surface pressure distributions.

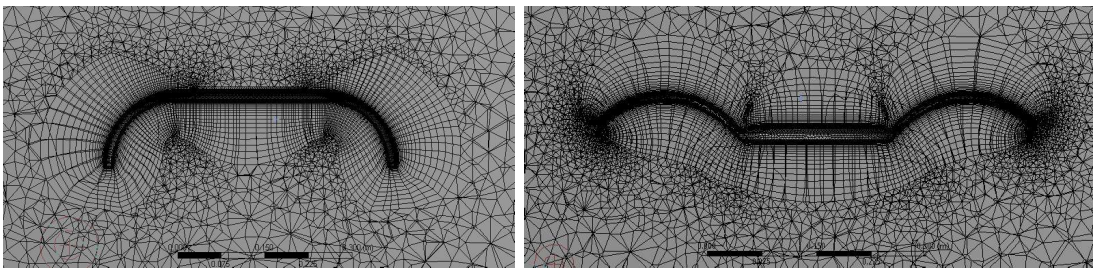

(a) Traditional design. (b) Traditional design.

Figure 3.19: Mesh used in the three-dimensional simulations.

Figure 3.19 shows the final meshes used in the computational analysis for both the traditional and novel designs. The settings used to generate these meshes are shown in the following table.

Parameter	Traditional	novel
Relevance	fine	fine
Smoothing	medium	high
Transition	slow	slow
Span angle	fine	fine
Inflation		
Number of layers	45	30
Growth factor	1.2	1.2
Max thickness (m)	0.15	0.1

Furthermore, the surface of the traditional design's disk was map faced meshed. This process could not be successfully reproduced on the novel design. Finally the solver settings used are the same for both designs and are as follows:

Type	RMS value	Advection model	Turbulence model	Turbulence numeric
Steady state	10^{-4}	High resolution	BSL EARSM	First order

3.2.2.3 Simulation outputs

Using the tools provided within the ANSYS software, a set of parameters were chosen to evaluate the design being used, the first of which is the velocity profile of the flow. Pressure distribution on the surfaces is the parameter of interest, and finally the forces and moments generated. In order to extract data from this software, points or lines need to be defined where the data is to be sampled, notably on the surface. This can easily be done using the post analysis ANSYS software and is shown in figures 3.20 and 3.21.

Boundary layer

The generated jet flow follows the surface curvature, therefore the proper reference frame to study the flow is [θ,y^*], where y^* is the normalized distance from the surface with respect to the nozzle height.

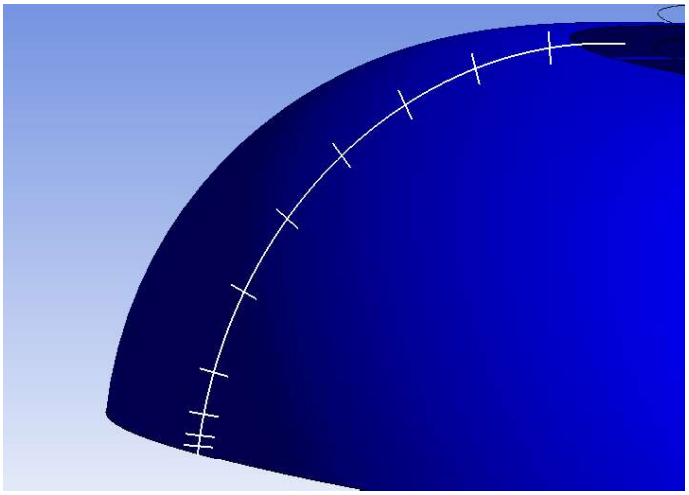

Figure 3.20: Lines used to measure boundary layer velocities.

As can be seen in figure 3.20, lines normal to the surface are drawn at regular θ intervals. This allows the software to probe these areas and return the 3D velocity vector at each discrete point on the lines. Furthermore it can be seen that there are curves running parallel to the surface, creating a 2D grid used to sample the velocity profile in a relevant manner. Both of these probe lines can be used together to determine the flow evolution as it travels over the surface, which can then be compared to cases shown in the validation section.

Pressure distribution

In order to extract the relevant and correct information, four curves are generated using two planes, one on the xz axis and one on the yz axis. Computational pressures can be averaged out over the different curves in order to get a more accurate estimate of the pressure.

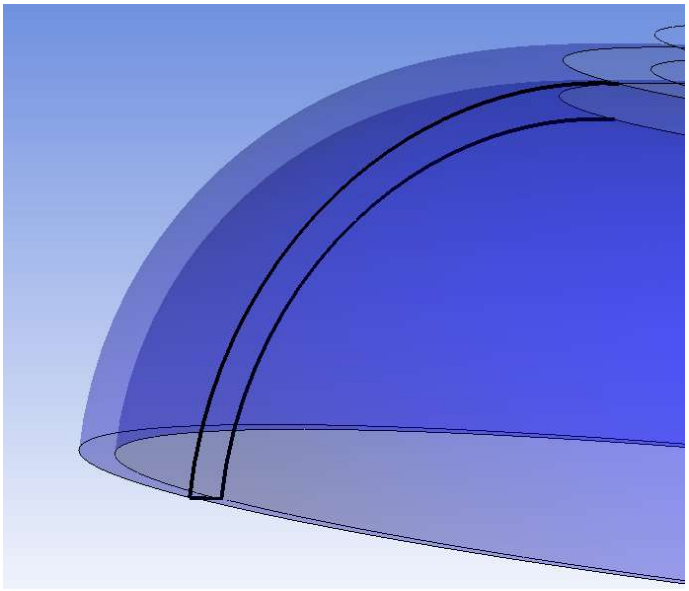

Figure 3.21: Curves used to probe pressure readings and planes used to generate them.

Lift generation

Forces and moments act on the surface as a whole. ANSYS has a tool to estimate a force exerted on surfaces. This tool is used on both the top and bottom surface of the disk to measure the lift. These results are then used to compared with experimental data.

Upwards force is also generated by deflected thrust, therefore an extra component needs to be added to the computational model. A flat horizontal surface is defined from the edge of the disk out to the fluid model's limits and is used to measure the jet thrust that is left over after the flow has left the disk.

Furthermore, this function is also used to determine the thrust of the jet as it leaves the compressor. This is used to determine the efficiency of upwards force (e.g. is it better than just having the compressor pointing down?).

3.2.2.4 Control investigation

A computational model was run to explore the moments generated by a control surface deflection. The first notable difference between this model and the final experimental setup is that four control surfaces are used rather than three. This happened during the design iteration of the experimental setup. Secondly, they span the entire control region rather than just half. One control surface was deflected and resulting moments and forces were recorded. The experimental procedure however

returned the lift coefficients for a system where all controls were deflected. They covered a span of 120^o while one control surface in the CFD spans 90^o. The physical experiment should therefore vary a third more than the computational.

In order to estimate the lift coefficients of such a system from the CFD data, the following conversion is applied:

$$c_L = c_{L0} + 4\delta c_L, \tag{3.85}$$

where c_{L0} is the lift coefficient at no deflection, and δc_L is the changed in lift coefficient experienced by moving one control surface. It is assumed that the change in lift coefficient is due to a force increment experienced in the affected region. Therefore, if all four regions were affected, the change in lift coefficient would be fourfold, the area affected by a change in lift is four times larger.

In order to estimate what moments would be generated with control surfaces of any angle of area up to 180^o, the following equation is formed to describe the moments generated by one control surface.

$$M = \int_{-\Delta}^{\Delta} \delta L_c x_p \cos\Delta d\Delta, \tag{3.86}$$

with δL_c being the change in lift generated by the control surface in a 2D plane, x_p the centre of pressure, and Δ the span of the control surface. It can be assumed that δL_c and x_p are the same for the same control angle but different spans, we can therefore integrate and get the following relationship:

$$M_2[\sin(\Delta_1) - \sin(-\Delta_1)] = M_1[\sin(\Delta_2) - \sin(-\Delta_2)], \tag{3.87}$$

which can further be reduced to

$$M_2 \sin\Delta_1 = M_1 \sin\Delta_2. \tag{3.88}$$

This relationship can also be used with the linear approximation coefficient for moments. Similarly, as the control surfaces on the experimental apparatus do not cover the entirety of the nozzle exit, the physical estimated lift coefficient can be calculated with the following equation:

$$\delta c_{LC} = \delta c_L \frac{n\Delta}{2\pi}, \tag{3.89}$$

where δc_{LC} is the change in lift coefficient due to control surfaces being deployed, n is the number of control surfaces, and δc_{LF} is the change in lift coefficient if the entire nozzle experienced a control action. It can be calculated using the following equation from the CFD data,

$$\delta c_L = 4\delta c_L. \tag{3.90}$$

3.3 Experimental setup

3.3.1 Rig evolution

A benefit of the mount seen in figure 3.23 is that it was mounted from only one side. Being top mounted, it could easily be fit into a wind tunnel or be subject to a different set of experiments. Due to design limitations that will be discussed, this however did not generate any useful data. The main aspects that have been the most heavily modified since starting testing are the air supply, the sensors, and the hub/mounting. The motor, controller and disk have not been changed throughout. Figure 3.22 shows the initial simplified design concepts. The tube was meant to connect all the cables, air supply and to mount the rig.

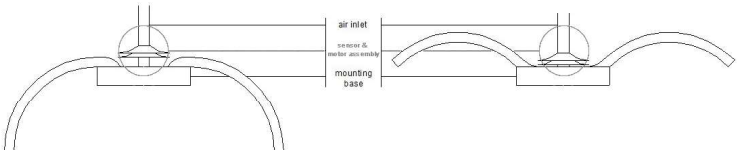

Figure 3.22: Initial design configuration

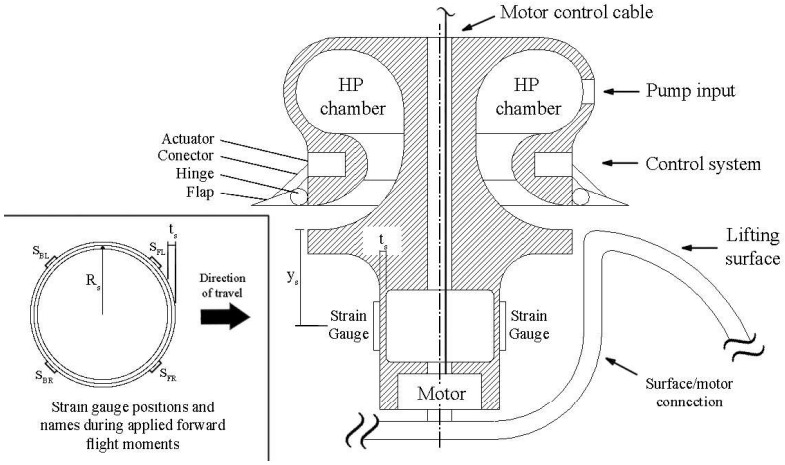

Figure 3.23: Close up of the mount design

3.3.1.1 Air supply

Compressed air

The flow was initially generated by a pipe leading to an external supply. The chamber used to guide the air on top of the surface can be seen in figure 3.23.

While some results were seen using this method, multiple iterations were made before scrapping this approach. Issues mainly occurred with the piping. Some connections would be loose or the pipe would not have a consistent pressure due to other experiments being run. Another issue with this approach was the lack of flow control. The air was regulated by a hand operated valve. This method while not ideal, only had to be changed when the whole experiment needed to be moved to a different laboratory in order to use a more accurate load cell, discussed in section 3.3.2.

Radial compressor

The next evolution of the flow generating device was a radial compressor, seen in figure 3.24a. In order to drive it, a planetary gear system was designed 3.24b. The compressor could not be top driven as that is where the inlet resided. Furthermore, there was not enough space between the bottom of the compressor and motor driving the disk to put in a second motor purely for this purpose.

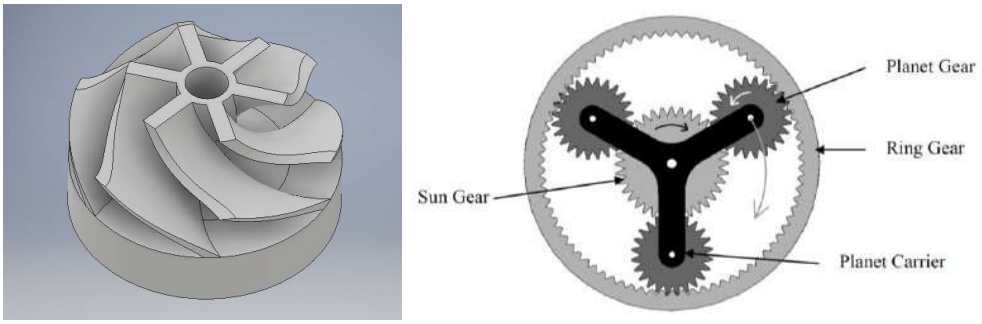

(a) Radial compressor.

(b) Planetary gear system.

Figure 3.24: The second major iteration of the air supply system.

During initial testing of the compressor (without the gearing system), flow velocities measured were the same order of magnitude as from the compressed air supply ($\tilde{1}$ to 10 m.s^{-1}). The planetary gear system was initially 3D printed but the tolerances were not high enough. The vibrations experienced by the system were too great. The next iteration used a laser cut gear system in order to lower tolerances. However, the acrylic used was not strong enough and gear teeth failed. In the next interaction of this concept wheels were used instead of gears as the torque generated by the spinning disk was only measured to be around 0.05 Nm.

The wheels designed were 3D printed in order to have the required gear ratio. In order to maximize the friction, the contact surface of the wheels was masked with a rubber tape one side and an abrasive tape on the other. It worked for a short period of time, but the tapes used deteriorated and the system would start slipping. This

approach was eventually abandoned for a top mounted electric ducted fan that was provided by a different research group.

Electric ducted fan

An electric ducted fan had been acquired as the following method of air supply. With a maximum power of 1.9 KW, it generated an axial flow. The maximum power was never achieved, the maximum was 65% of full thrust. It was mounted vertically over a deflector plate. The compressor used was nearing the end of its life cycle throughout the tests. It had been bought a few years ago and no replacement that fit the case could be found. The test were left with in an incomplete dataset seen in section 4.4.2.

3.3.2 Load cell

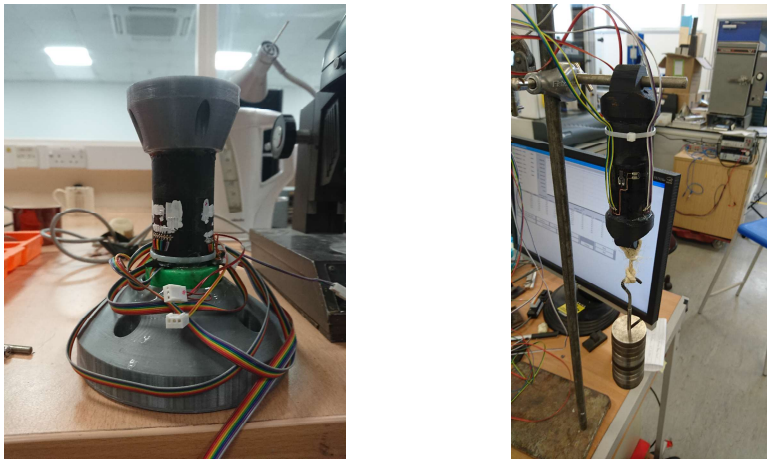

(a) Side view. (b) Calibration test.

Figure 3.25: The first iteration of the load measuring device.

In order to measure the forces in all six axes, a load cell was designed (seen in figure 3.25). The load cell consisted of PVC pipe with three half Wheatstone bridges spaced 120^o to measure axial strains acting on the pipe. Offset by 60^o, three quarter Wheatstone bridges were used to measure the torsional strains acting on the pipe. This method was initially chosen over purchasing a load cell due to the limited budget.

A series of calibration tests were carried out, the setup used in the axial portion of testing can be seen in figure 3.25b. The results of the calibration test can be seen in figure 3.26. While it seems that results are measurable at the desired scale, there in fact seemed to be something off with the data. Signal amplitudes of the

shear strain seem to decrease with a higher moment applied. While it is a consistent oddity that can be taken into account, other issues with this approach are present.

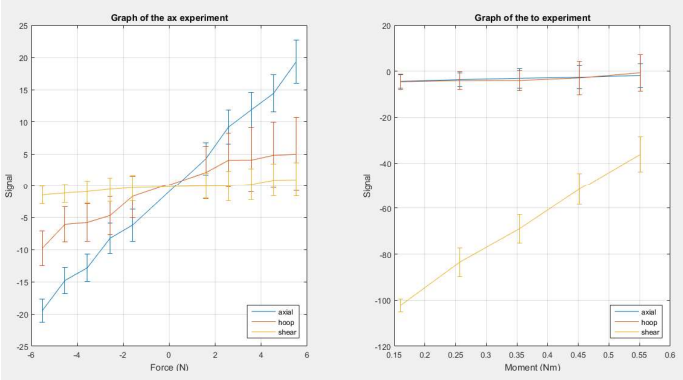

Figure 3.26: Results of the calibration tests.

The first issue is a drift present when the sensor is running for any amount of time seen in figure 3.27a. Another issue which reduced the result accuracy is a change in signal when the air supply is turned on (seen in figure 3.27b), probably due to cooling of the strain gauge by convection, as the tests were run in a box.

Luckily, a load cell purchased by another research group was not being put to use any more. The load cell in question required a PC which was set up in a different lab. Moving the experiment entailed redesigning the air supply.

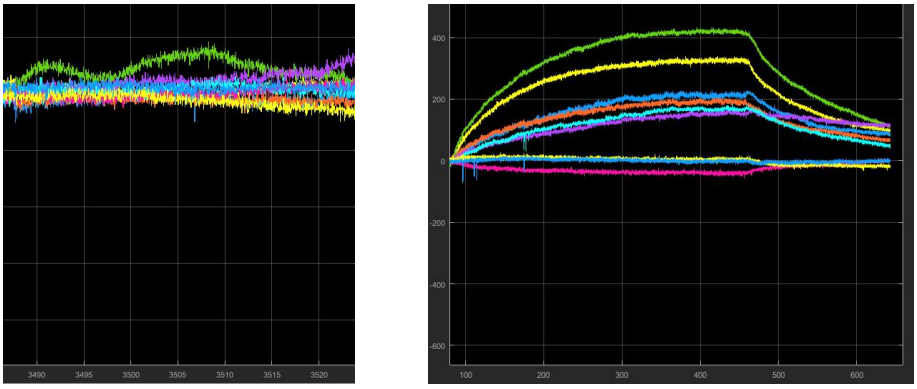

(a) Drift of the sensor when no load is present.

(b) Effect of turning on and back off the air supply.

Figure 3.27: Issues present while using this sensor.

3.3.2.1 Measurement devices

Disk rotation

The first iterations of the experimental setup used a slotted disk mounted on the motor shaft to periodically block a light gate. The first light gate was makeshift, and involved an IR LED and sensor. This method returned false positive triggers and had to be scrapped and replaced with an off-the-shelf light gate. The slotted disk used was too thick and damaged the light gate. The disk could not be made thinner as it would warp and eventually damage the light gate.

Few off-the-shelf encoders were purchased in order to solve the problem. Unfortunately, there was no obvious way to securely mount the encoder onto the motor for extended periods of time.

Airflow

In the first phases of testing, airflow measurements were conducted using a hand held anemometer. While this method worked, the accuracy was questionable as the position of the device could not be reliably reproduced between runs.

The next iteration saw the use of a pitot-static tube located at the outer edge of the disk. Two main issues can be found in this approach. Firstly the pitot tube had a diameter of about 1 cm, while the nozzle height used throughout the experiments is also 1 cm. Air velocities at the top, middle and bottom of the tube would therefore be considerably different. The second issue is that measuring the flow at the end of the disk is not entirely representative of the regime (for example in the case of separation). The final iteration of airflow measurements can be seen in figure 3.28, where two taps are mounted separately at the nozzle exit.

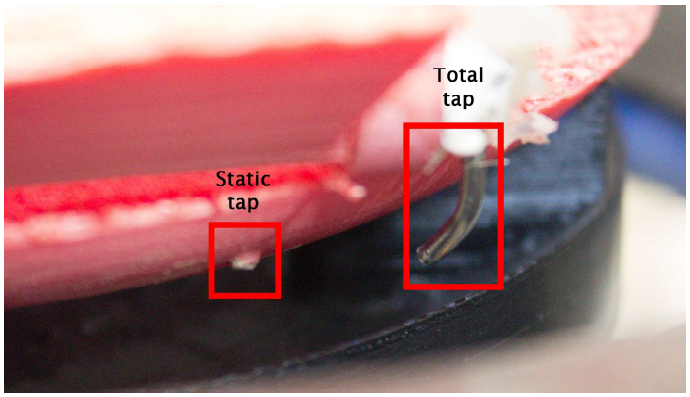

Figure 3.28: Image of the static and total pressure taps mounted on the nozzle exit.

3.3.3 Final build

3.3.3.1 Overview

The experimental setup used primarily consists of four sections described below. The experimental control is done through an Arduino, while the load cell is a standalone system. All systems are linked through a Matlab interface synchronising load cell readings with the experimental configuration. The MATLAB synchronisation implementation can be seen in APPENDIX 1 in the main loop section starting line 576. The angular and jet velocity are being read in real time. When an load cell measurement is required it takes highest priority. When completed the loop continues and the buffer of velocities is emptied into memory.

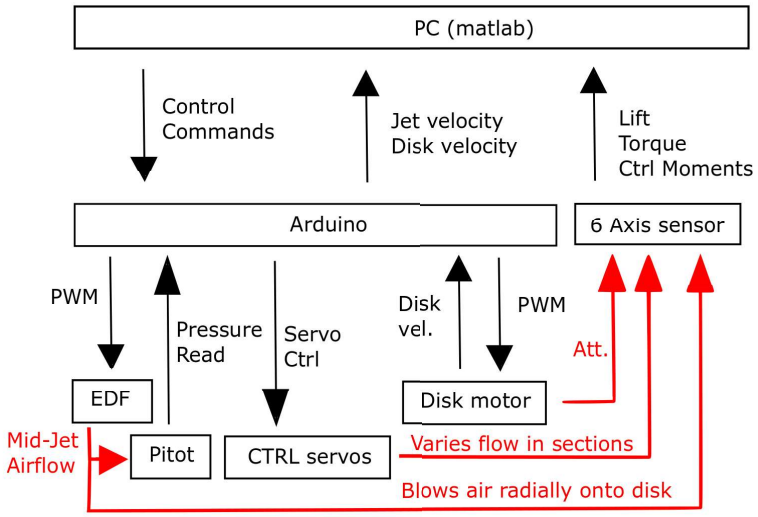

Figure 3.29: System diagram: black are digital and red are physical interactions.

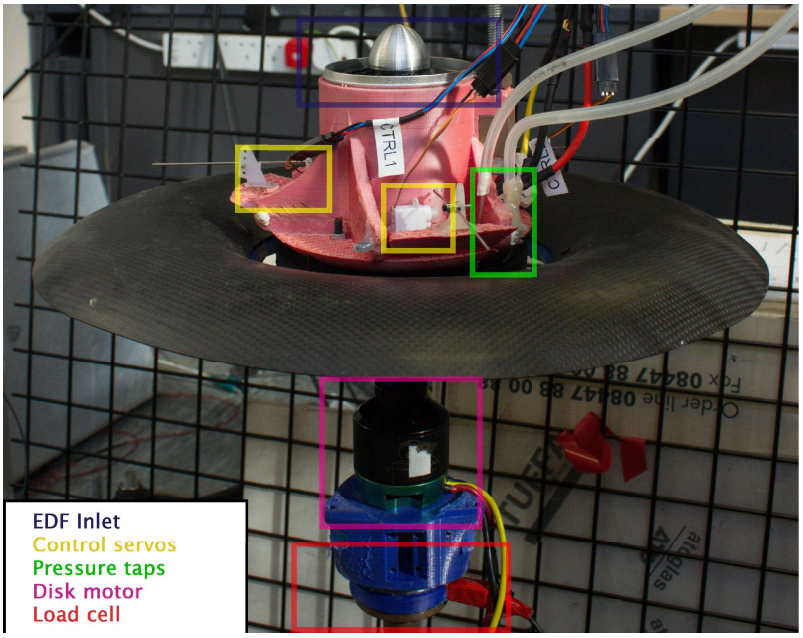

Figure 3.30: Image of the experimental setup with relevant systems highlighted.

Disk

The shape and size of the disk is identical to the model used in the computer modelling. In order to build it in carbon fibre, a mould was first made out of MDF wood on a CNC lathe. Carbon fibre was chosen due to its high tensile strength relative to its weight. The main stresses experienced by the part are radial due its rotation. The wooden mould was coated with a filling paint and sanded down. A fibre glass mould was made from the first mould. This mould is needed in case more than one part needs to be created. Both moulds and the finished CFRP disk are shown in figure 3.31.

(a) Wooden mould (b) Fibre glass mould (c) CFRP part

Figure 3.31: Disk build steps

Control systems

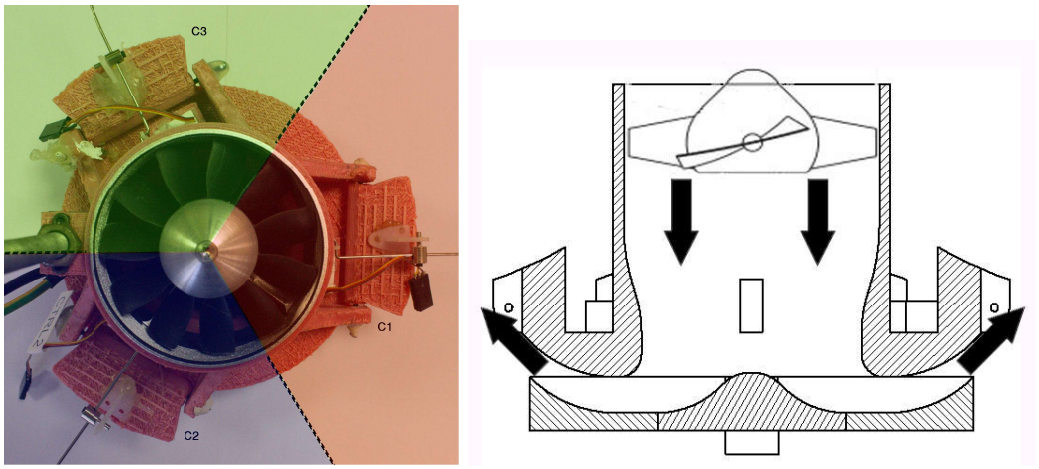

(a) Top view of the central hub section (b) Section of the EDF mount.

Figure 3.32: Overview of the top mounted assembly.

Three actuators are used to control flaps spaced at 120^o. They cover an angular area of 50^o. As shown in figure 3.32a, the EDF is centrally located with the flaps controlling outwards radial flow. The air initially gets deflected by a cone after the EDF and is directed by three ducts outwards, seen in figure 3.32b. Flaps are located at the centre of the duct. They are used to minimise the interference of one control surface with another, but coupling is inevitable. Two modes of control are encoded into the Arduino: homogeneous control, it sets all three control surfaces at the same angle;

heading control. it sets each surface to a specific angle in order to create pitching moment in the direction of desired travel calculated by the following equation,

$$\eta_i = \cos[\gamma_d + i\frac{\pi}{3}]\eta_r + \eta_{min}, \tag{3.91}$$

where, n_t is the total number of surfaces. This equation assumes that the maximum lift will be reached at the maximum angle (η). The reference frame of this control equation places the centre of C_1, C_2, C_3 (as shown in figure 3.32a) at headings of 0^o, 120^o and 240^o respectively, with γ_d in radians.

Airflow measurement

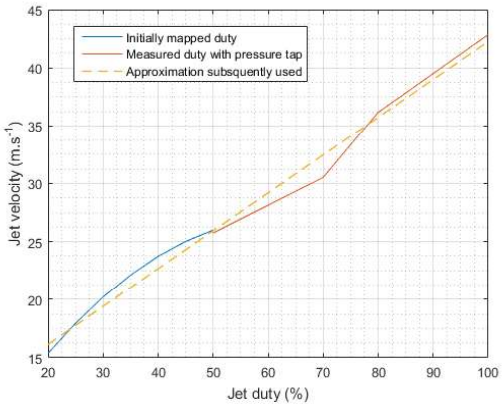

Figure 3.33: Measured jet velocity for low and high duty cycles.

Jet measurements were initially taken with a pitot static tube mounted at the edge of disk. Air flow readings were not very accurate due to the high turbulence of the flow. It was then attempted to map the airflow as a function of EDF duty. However, the power supply was not consistent (battery for higher loads, and 10A limited power supply for longer tests), whic caused the mapping to not work too well beyond the range of 50% duty. Finally, a pressure tap was mounted directly at the nozzle exit seen in figure 3.28. It can be seen in figure 3.33 that the initially mapped jet duties and measured duties line up more or less so that an approximate conversion can be made between the two and adapted to older data that did not have an airjet measurement.

In later stages of tests the jet flow rate is more accurately measured with the tube mounted at the nozzle centre. The jet velocity profile at the nozzle outlet is assumed to be parabolic and the measured velocity is the peak. The computational investigation however used a flat velocity profile as shown in figure 3.34. Comparing the lift generated to the computer simulation is done by evaluating it with respect

to the mass flow rate of the air. It can be calculated in both cases by the following equation,

$$\dot{m} = 2\pi x_{in} h\rho \int_0^h \dot{x}\delta y. \tag{3.92}$$

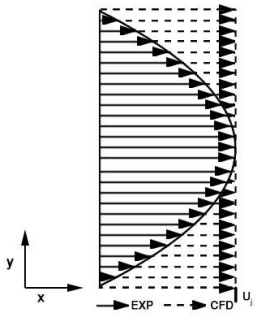

Figure 3.34: Diagram to represent the comparison of velocity profiles between the experimental and computational

The velocity profile equation in the experimental set up is assumed to be as follows:

$$\dot{x} = U_j(1 - \frac{y}{2h})^2. \tag{3.93}$$

We can therefore substitute the velocity $\dot{x}$ into equation 3.92, to get a simpler mass flow rate equation:

$$\dot{m} = 4U_j h x_{in}\rho\pi/3. \tag{3.94}$$

The Pitot and static taps mounted on the nozzle walls and exit are used to measure the total and static pressure. The conversion to jet velocity is done using the following equation:

$$U_j = \sqrt{2\Delta p/\rho} \tag{3.95}$$

where ρ is taken to be 1.225 kg.m^{-3} and Δp is the difference between static and total pressures. Due to the fan used, the jet turbulence is very high and the measurements taken are not accurate. In order to correct for that, the measurements are taken at consistent known duties of the motor. Figure 3.35 shows the airflow measurement taken at the maximum duty cycle. The mean velocity shown is calculated from all the experiments run with the maximum duty cycle as Ω does not influence the measurement.

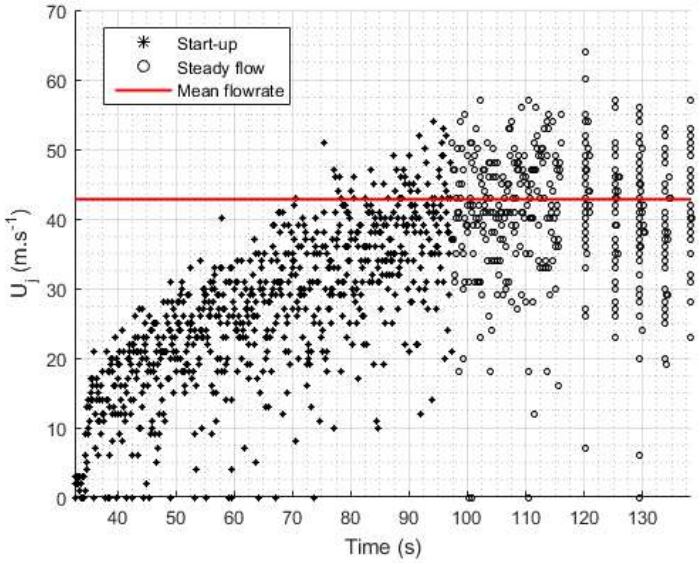

Figure 3.35: Data gathered within one air velocity measurement at $\Omega = 50$ Hz and $U_j \sim 43$ m.s^{-1}.

The final U_j measurements with relation to the Duty cycle of the EDF are shown in table 3.1.

Duty (%)	20	25	30	35	40	45	50	55	60	65
Error (ms^{-1})	2.19	2.72	3.04	4.01	4.23	4.15	3.51	3.49	4.13	4.07
U_j (ms^{-1})	9.38	13.6	18.1	21.5	24.4	26.1	28.5	30.6	32.5	35.9

Table 3.1: Error in the airflow measurements.

3.3.3.2 Arduino Controller

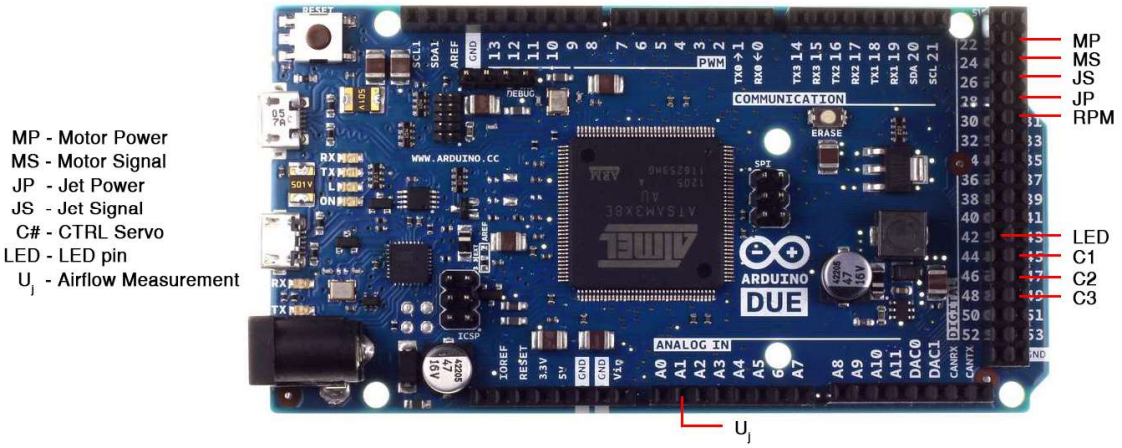

Figure 3.36: Arduino pinout.

An Arduino due is used to control the experimental system. It was initially chosen due to its high number of analogue pins, necessary to read all of the different strain gauges of the first sensor used. The pins assigned in the final iteration of the rig can be seen in figure 3.36. In order to control the system in real time, an Arduino architecture was designed which was comprised of the following modules with the full code available in Appendix 2.

Start up sequence

Once the Arduino is powered on the initialisation is done in the following order:

1. The serial port is activated first, this ensures that the system will not activate without a serial connection.
2. The pins are then assigned their respective properties (INPUT,OUTPUT,SERVO).
3. Interrupts are then initialised, there are five in total and are described in the functions section.
4. The motors are initialised. The controller checks for power on the respective pin for each motor before starting the sequence. The ESC requires that, upon start up, the PWM range is sent through.
5. Once both motors are initialised, the control surfaces are set to their minimum angle (most open state).

6. The air pressure is calibrated.

7. Finally "ready" is sent through the serial port to the PC.

Main loop

Each cycle of the main loop messages are checked. All other operations are done once every 5000 cycles, OR 0.1 μs, in order to give time for all the interrupts and messages to be handled. The rig is static and therefore does not need a feedback loop, otherwise, it would be run each cycle. The other executed operations are as follows:
• Sending the data.
• Controlling the motors, only if the motor in question is initiated and set to be on.
• Checking the status if required for the LED. The motor and jet both are at desired velocity.

The LED is on only when the disk and jet are both at desired velocity. This is used to insure experiments are not run outside of the desired parameter set.

Message handler

Nine messages are currently assigned:

start disk.	set bool to true
stop disk.	set bool to false, reset the timer to 0% duty
set disk velocity.	listens for a 32bit int, sets desired velocity
start jet.	set bool to true
stop jet.	set bool to false, reset the timer to 0% duty
set jet duty.	listens for a 32bit int, sets desired duty
set control angle.	listens for a 32bit int, updates all controls
set heading.	listens for a 32bit int, runs the heading calculation
calibrate pressure.	runs the pressure calibration

Table 3.2: Message list readable by Arduino

Motor control

Both motors are controlled in similar ways. Two interrupts per motor are used to generate the PWM signal required. The first one (M_up) on a timer of 20ms (PWM period) and the second (M_down) on a timer that varies between 1ms and 2ms (PWM duty). M_up writes a high signal on the desired pin and initiates the M_down

timer. M_down write a low signal and stops the M_down timer. The M_up timer is constantly running since the motor initialisation. In order to increase or reduce the duty M_down's timer is changed. The desired disk velocity is set by the user. It is then controlled with a proportional feedback loop using the rpm sensor. The jet however is not set with U_j, as the large fluctuation in air velocity measurements will cause an sudden changes to the desired duty. Under these conditions, it will not find stable operation. The user therefore inputs a desired duty between 0% and 100%, a proportional controller is used to throttle the increase in desired duty and avoid unnecessary shock loading.

Air velocity measurement and calibration

The jet velocity is calculated from the difference in pressure as shown in section 3.3.3.1. In order to calibrate the pressure, one hundred sample points are taken and the voltage zeroed. This operation is to be done when the jet and disk are both stopped otherwise the air velocity reading will be offset. The velocity is calculated similarly to the calibration measurement, a large sample is taken in order to calculate the mean voltage. The air velocity calculation is only called during the data sending function that connects to the PC.

3.3.3.3 Data acquisition and user input

MATLAB software, seen in figure 3.37, was developed to communicate with the load cell and controller. Before any commands or measurements can be taken connection must be established by clicking one or both of the connecting buttons. They can be used individually in case only the Arduino or sensor need to be tested. Once connected the software completes three main purposes. Commands are sent to the controller in order to alter the tested configuration. Data is acquired from the different sensors and saved in an easily accessible format. The GUI also offers basic data analysis and visualisation after each experiment. The full code is available in appendix 1.

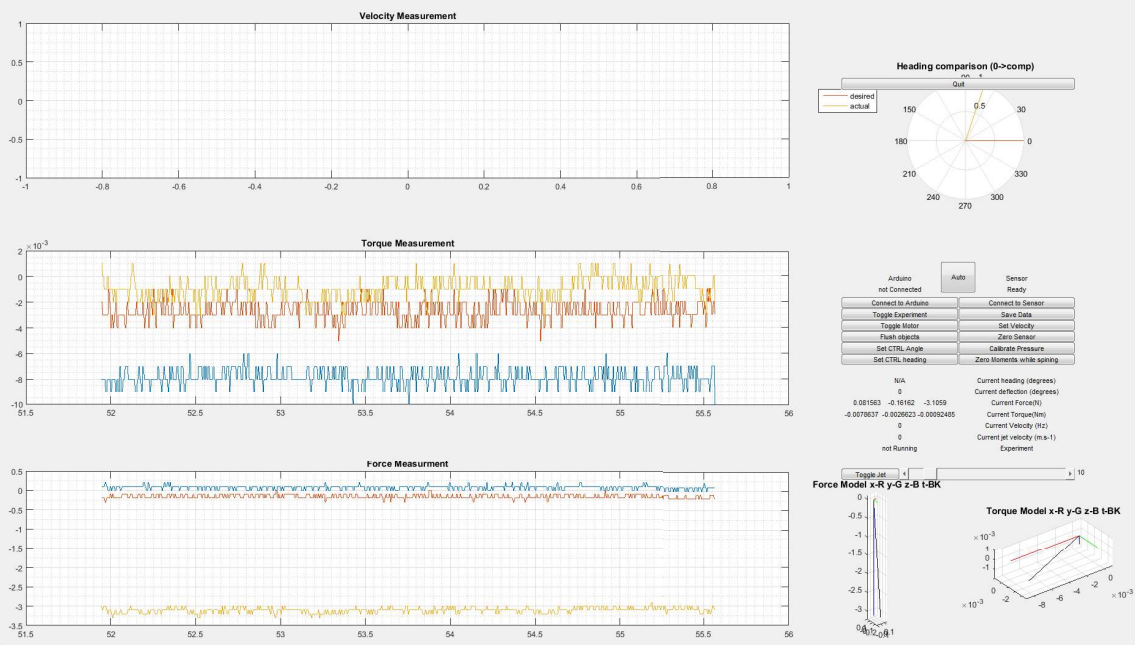

Figure 3.37: GUI of data acquisition script when loaded with a 3N weight.

Connection

Connect to Arduino will open a prompt with all the available serial ports. Upon selection it will open the serial port selected, which restarts the controller. Once the controller's start up sequence is completed it sends a "ready" message. If the message is not received before a time out the port is closed so that connection can be reattempted. The text will change through "not connected", "connecting", and "ready" if connection is successful.

Connect to Sensor will open a prompt asking for the experimental sample time, set to 1 s by default. After confirming the selection, the UDP (User Datagram Protocol) port is opened and the software listens. If the connection is successful, the correct data format will be detected before time out and the text will progress in the same way as the controller.

Controls

All controls that affect the experimental set up will send a message through the serial port. It is then read by the controller's message handler.

Toggle Experiment will start the data acquisition protocol. During this process, the screen is locked and a loading bar shows the progress. This process generally takes longer than the selected sample time.

Save Data prompts the user to select a file name and then saves the data structure in the preallocated directory `"data"`.

Toggle Motor and **Toggle Jet** turn the respective components either ON or OFF. The slider present next to **Toggle Jet** controls the duty and is represented by the number on the right.

Set Velocity prompts the user to input the disk's desired angular velocity, in Hz. The input is then sent to the controller.

Flush objects closes all currently connected ports. This command is used in the case of a communication issue with either device.

Zero Sensor update the stored zero offset. The load cell measurements slightly fluctuate therefore before most experiments the device is zeroed.

Set CTRL Angle will prompt the user to set the control surfaces' angle. In this setting all three actuators are set at the same angle.

Calibrate Pressure is used to zero the sensor attached to the pilot static tube.

Set CTRL Heading prompts the user to set a desired direction of travel in degrees between 0 and 360. 0 is aligned with the load cell's x axis. The desired direction is sent to the controller which determines the required actuator settings.

Zero Moments while spinning was used to determine what effect control actions had on the disk while spinning. This method was unsuccessful.

Auto is used to run a batch of experiments. It will prompt the user the desired number and configuration of experiments. Once selected, it will continuously measure the system to insure no leftover oscillation from previous experiments is present and the sensor is stable. After zeroing the system, the motor and jet are turned on. Once the correct velocities are achieved an LED connected to the controller will light up and any user input will trigger data acquisition. After the predetermined number of measurements is taken, the motor and jet are both turned off.

Data Acquisition

Two sources of data are handled by this system. The controller sends current jet and disk velocity measurements through serial while the load cell sends the forces and torques through UDP. While the application is connected to the Arduino it receives the jet and disk velocities and plots them in real-time. In order to ensure the system reads this data correctly, it is sent through the serial port as two 16 bit integers packaged as a 32 bit packet. The integers sent are the measured decimal value to three decimal places.

Due to the high sample rate of the load cell, the application developed is not able to handle real time data acquisition and analysis. In order to circumvent this issue, a buffer system is used. The load cells' sample rate is known and used to determine a measurement's size. The acquisition rate of sensor is 2 KHz. For a measurement of 2s, it takes 5-10s for the computer to empty the buffer into local variables. When

an experiment is initiated, the buffer is filled and data is slowly being loaded into MATLAB variables. During this process, the jet and disk velocities are buffered until it is completed.

At the end of a measurement, it is logged in a structure along with all other experiments since the application was initiated. The data structure contains the true time, jet and disk velocities measured since connection. The configuration settings of each experiment are also saved along side the experimental data. This includes the disk and jet velocities, desired duty and control settings.

Data Visualisation

Velocity Measurement plots the velocities sent through the serial port from the controller in real time. **Torque Measurement** and **Force Measurement** will update after every experiment to show the measured torque and force respectively. This information is also available in the text under the control panel. Velocities will update in real time while the forces and torques will update once an experiment is complete. The numbers represent averaged value in each axis.

The two plots on the bottom right show the averaged values and resultant force. This plot was used to easily visually determine the relative and absolute forces and torque measured by the load cell during the troubleshooting period. **Heading Comparison** shows the desired (yellow) and measured headings (red). This plot is only active when a heading is selected.

3.4 Summary

The computational model and experimental setup have the same geometric parameters regarding the curved surface and nozzle. Both setups are capable of inducing flow through jet and rotation. Control surfaces are present in both. In the computational model, there is four flaps spanning 90^o each. However in the experimental rig, there is only three control surfaces spanning 40^o each, with gaps between the flaps.

The computational and experimental setups are capable of measuring in six degrees of freedom, as well as, the jet's nozzle and disk's angular velocity. The computational model however can also probe the pressure and velocity at any point in the fluid domain.

The computational setup uses a steady state BSL EARSM turbulence model. It incapable of simulating vortices, vibrations and unsteady regimes. The experimental setup experiences vibrations, lowering the data's accuracy. Furthermore, it is not capable of measuring the nozzle boundary profile, or the pressure distribution on the surface, only the jet's maximum velocity is measured at the nozzle's centre. No active flow control is present.

Chapter 4

Results

Computational and experimental results are discussed in this section. Firstly the boundary layer of the flow and pressure distribution on the surface are computationally derived. These comprise the first two sections in this chapter attempting to examine the mechanisms producing lift. Analytical models described in the previous chapter attempt to fill the gap between the first and last two sections in this chapter. The third section presents the lift findings, both computational and experimental. The forces and moments are measured at $\eta = 0$ for a range of Ω and U_j. Finally, results generated by implementing a control flap are presented. The computational and experimental systems differ in the section as explained in chapter 3. Computationally one flap will set at a range of angles, while experimentally all the flaps are actuated. Corrections to the data are made to make the results comparable.

4.1 Boundary layer

The surface pressure is a direct result of the boundary layer forming along the surface. In order to examine the boundary layer, we define v_θ, v_ω, and v_r respectively as the velocities in θ, ω, and z as shown in figure 3.1. In order to transform from the xy Cartesian plane, the following equations are used:

$$v_\theta = \sqrt{u^2 + v^2}\cos\theta' \tag{4.1}$$

$$v_r = \sqrt{u^2 + v^2}\sin\theta' \tag{4.2}$$

where $\theta' = \theta - |\tan^{-1}(v/u)|$. u and v are the velocity components in x and y respectively. v_ω is equivalent to w, the velocity component in the z coordinate of the CFD model. In order to render these dimensionless they are scaled on U_d. The following equation shows how to calculate U_d in the 2D.

$$U_d = \sqrt{U_j^2 + [x_0 + R\sin(\pi/4)]^2\Omega^2} \tag{4.3}$$

As can be assumed from the pressure distribution plots, the boundary layer will vary depending on θ. It will expand but its maximum velocity will be reduced by more than just the inverse square. Four positions along θ are therefore taken to examine the boundary layer evolution: $\theta = \pi/8$; $\pi/4$; $3\pi/8$; $63\pi/128$, with the final position attempting to investigate the equatorial behaviour of the flow. For a jet only flow, we can ignore the transverse velocity v_ω. The CFD results can be seen in the following figures. Further more the jet nozzle height $h = 0.01$m.

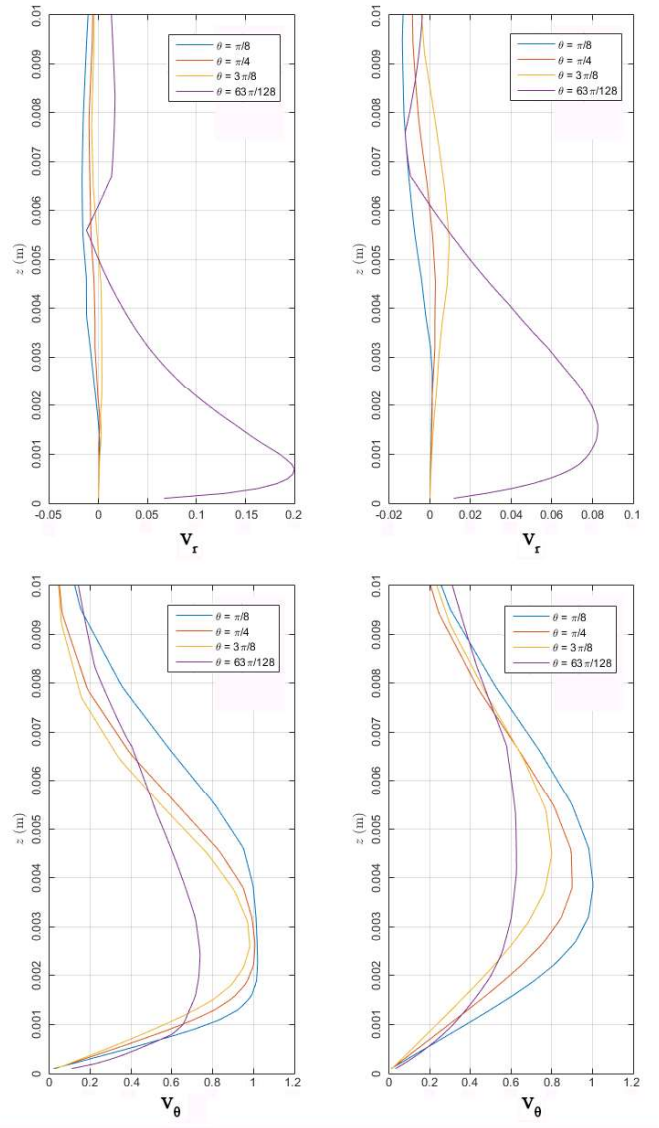

Figure 4.1: Radial (v_r) and tangential (v_θ) velocity magnitudes (they are divided by U_j) at different θ positions for $U_j = 5$ and 1 $m.s^{-1}$ respectively.

As can be seen in figure 4.1, the flow gains a significant radial velocity component at $\theta \simeq \pi/2$ ($\theta = 63\pi/128$). The maximum scaled value of v_r increases from 0.08 to 0.2 for U_j varying from 1 to 5 $m.s^{-1}$. The increased radial velocity can be interpreted as the angle of flow leaving the surface $\alpha = \text{atan}v_r/v_\theta$. Furthermore, the boundary layer thickness is smaller and the velocity gradient is stepper for higher values of U_j. For the case of 5 m/s at $\theta = \pi/8$, the layer is flat at $0.02 < z < 0.04$ due to the profile of the jet at input (x_in). The CFD software's input profile is a constant U_j at varying $z < h$, where h is the slot height. The boundary layer therefore is not fully formed at $\theta = \pi/8$ where the measurement is taken. Lastly, it can be seen from figure 4.1, as z increases at positions of $\theta \leq 3\pi/8$, $v_r < 0$; this can be interpreted by a down flow of surrounding air outside of the boundary layer.

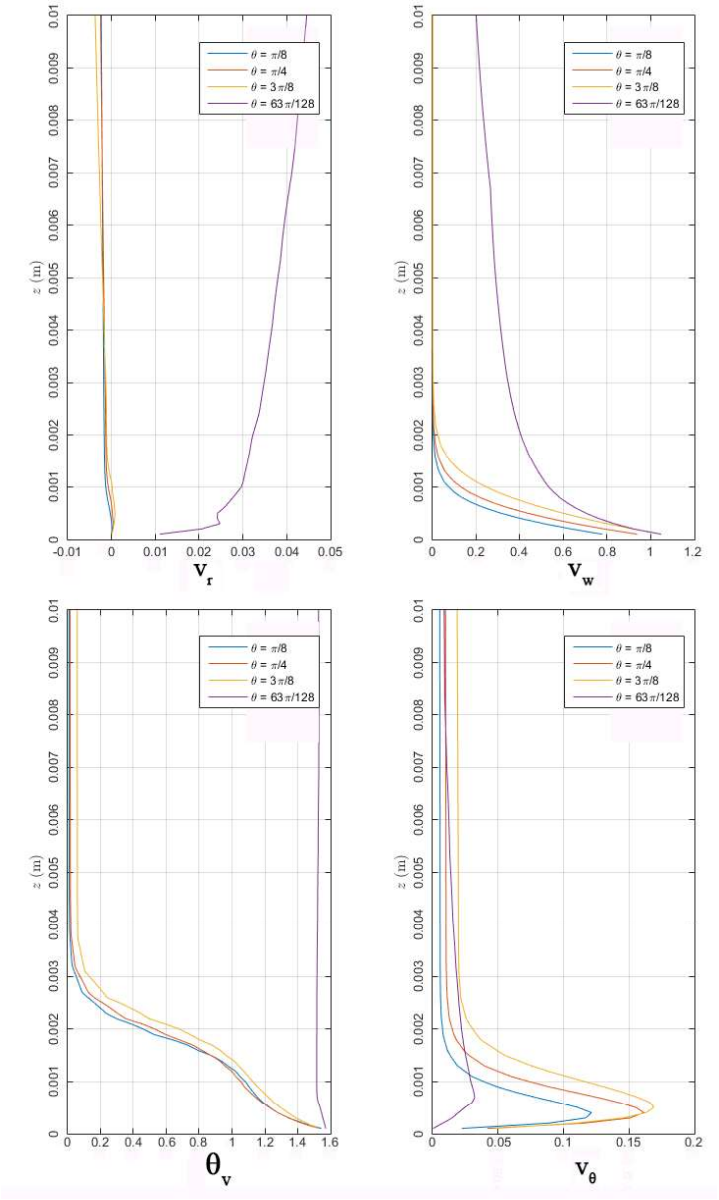

Figure 4.2: Dimensionless tangential (v_θ), radial (v_r), and transverse (v_ω) velocities and surface velocity angle (θ_v in rad) at $\Omega = 20\ rev.s^{-1}$ and $U_j = 0$.

The surface velocity angle (θ_v) is the tangential velocity angle to the surface; where 0 is pure v_θ and $\pi/2$ is pure v_ω ($\theta_v = \tan^{-1}(v_\omega/v_\theta)$). As can be seen in figure 4.2, the flow behaves very differently in the equatorial region: v_θ is very much reduced, v_ω stays significant further from the surface, and v_r is positive and of much greater magnitude. The maximum v_θ for a purely rotating flow is located at $\theta \simeq 3\pi/8$, at higher θ the velocity magnitude drops again. At non-equatorial

regions, the flow close to the surface is flowing in the γ direction and changes to θ as it gets further from the surface. similarly to the pure jet case, the radial velocity (v_r) in the non-equatorial region is negative suggesting a down flow of ambient air. Furthermore, as the angular velocity decreases the boundary layer thickens; for $\Omega = 1\ rev.s^{-1}$, $\theta_v \sim 0$ at $z \sim 0.01$ m, in a non-equatorial region.

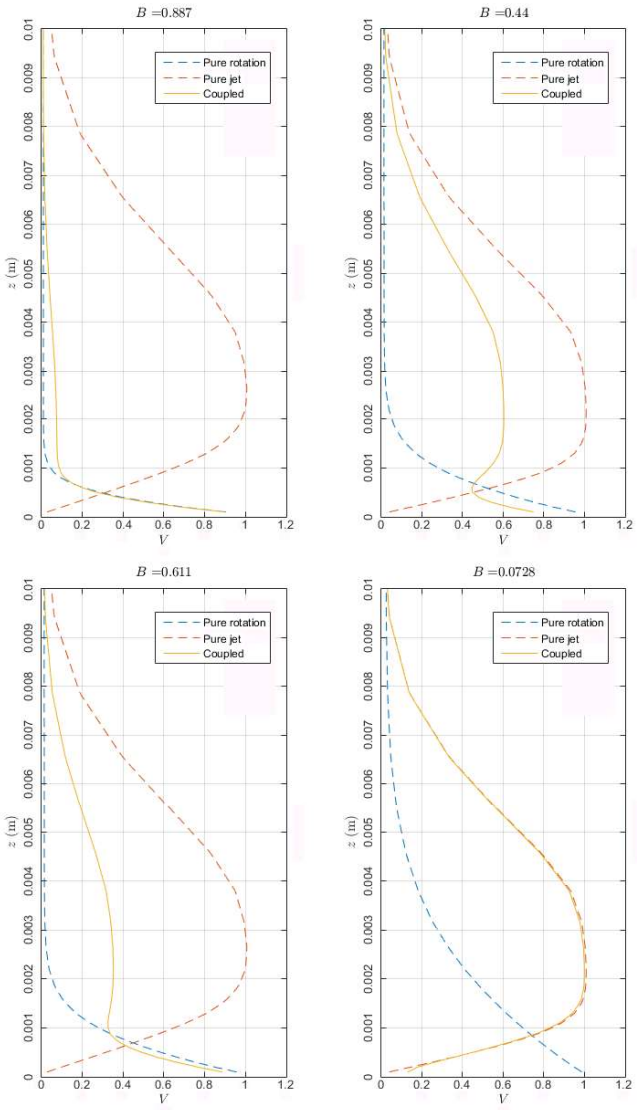

Figure 4.3: Variation of total dimensionless velocity (V) with distance from surface (z) at $\theta = \pi/4$, for different rotation parameter B,

As can be seen in figure 4.3, the boundary layer shape is similar to a jet-only case if B is close to 0, and similar to a rotation-only case for B closer to 1. The velocity

(V) at $z \simeq 0.003$, seems to be proportional to the jet only velocity with a factor of $(1-B)$, which means the velocities induced by the disk and the jet are compounded. The plotted velocity contains both tangential and transverse components. It can be assumed that the velocity close to the surface ($z \sim 0$) is mainly v_ω, and at $z > 0.003$, mainly v_θ. In the region $z < 0.003$, the velocity is a combination of tangential (v_θ) and transverse (v_ω) velocities.

4.2 Pressure distribution

This section shows the computational models of pressure distributions on both the traditional and novel design. It will explore the variation in pressure due to jet and angular velocities using the rotation parameter B. The relative pressure to ambient is used to illustrate this. Using a pressure coefficient proved to be ineffective as there is no free stream velocity. Furthermore, the total pressure located under and over the disk vary due to jet blown on the upper surface. Attempting to use U_d as a free stream velocity would also give unreasonable results in the case of high B. this is due to U_d being the value at mid-chord with the edge having much higher velocities and associated pressures. Finally varying the nozzle height (h) would change the pressure as it effectively changes the mass flow rate over the disk. An equation for a pressure coefficient can be derived if the all these variables are taken into account.

4.2.1 Traditional model

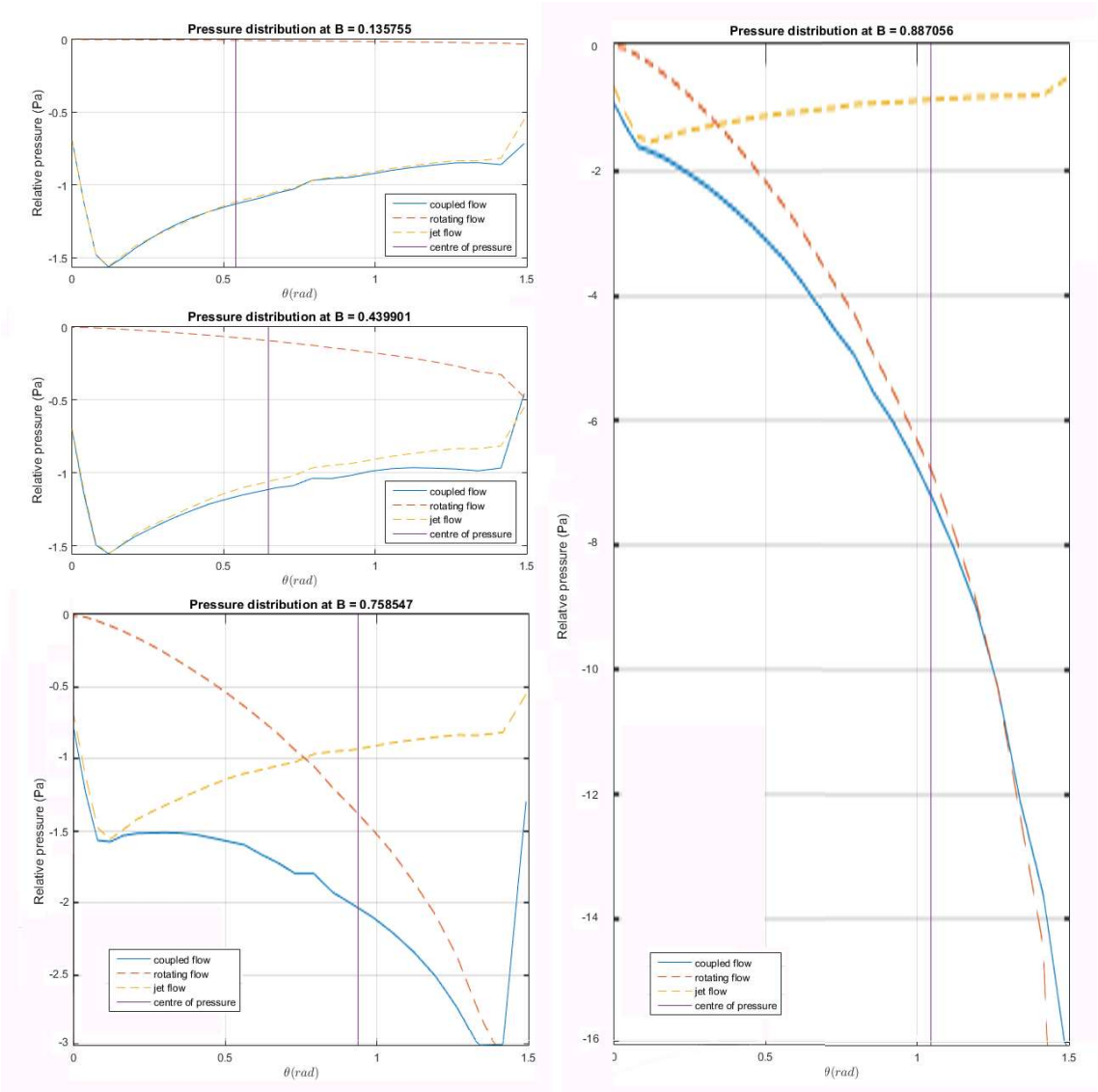

Figure 4.4: Variation of upper surface pressure distribution with B.

Figure 4.4 shows the transition of the pressure distribution from a jet-dominant to a spin-dominant system. Similarly to the flow velocity in the previous section, the pressure distribution produced by a jet and spin induced flow seems to be compounded from its individual configurations. Furthermore, the pressure distribution transitions continuously from a spinning to jet configuration. Figure 4.5 shows c_p and the force vector for spin and jet only cases. Because the transition is continu-

ous, any desired centre of pressure position between the two cases can be achieved using the appropriate configuration. This is useful for easily programming a PID controller for the UAV.

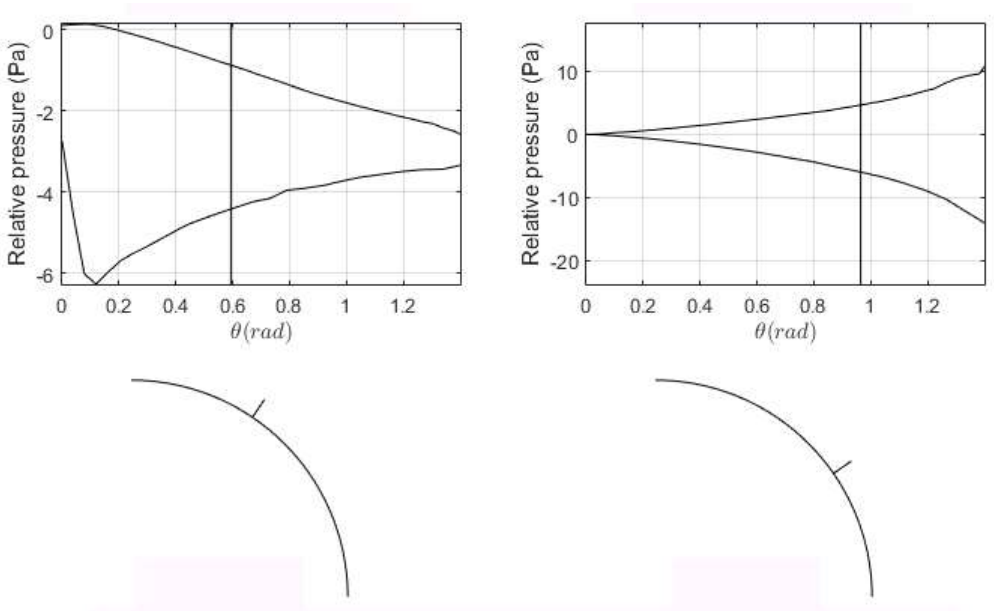

Figure 4.5: Pressure distribution for jet only (10 m/s, left) and pure spin (50 Hz, right) inputs individually (on the top) with respective force vector positions on the surface (on the bottom).

A simplified model of the pressure distribution, based on the individual cases, is estimated using polynomial fitting of the value at certain points on the surface. As can be seen in figure 4.6, the model is more or less accurate (within 10% of the computationally estimated data). The model does not take into account the equatorial regions ($\theta_{max} = 1.5$). The equatorial region will not affect the lift generation very much as it will only contribute to the horizontal component of the force vector. The positions θ_a and θ_b are used in the upper surface modelling. As can be seen in figure 4.4, at $\theta_a = 0.1$, the pressure magnitude on the upper surface is the same as for a jet only case. The simplified model can be further improved by taking into consideration the flat rotating bottom surface under the motor. The flow in that region can easily be modelled using the Von Karman equations described in 2.3.2.

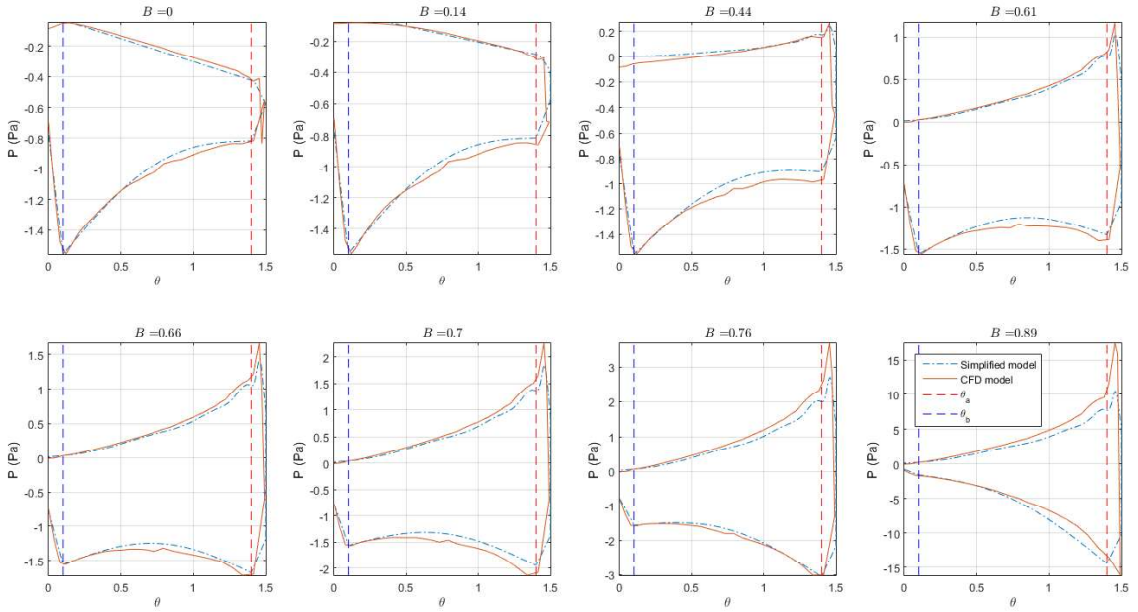

Figure 4.6: Simplified model described shown along side computational model at $U_j = 5$ $m.s^{-1}$.

Figure 4.6 shows an attempt to generate a simplified model of the pressure distribution given any jet and angular velocity. The pressure at points a and b can be polynomially fitted to U_j and Ω. The following equations model the behaviour of the pressure distribution between these two points.

At $\theta_b = 1.4$, the pressure magnitude is equal to a jet only case for B close to 0, a rotation only case for B close to 1, and a combination of both in between. After some trial and error, the pressure magnitude can be approximated by $\sqrt{P_f^2 + P_s^2}$, where P_f and P_s are the jet-only and rotation-only pressure respectively. The required pressure values are estimated using a polynomial fitting tool at θ_a and θ_b with the data set already available. The edges of the distribution (for $\theta < 0.1$ and $\theta > 1.4$) are modelled linearly. The distribution curve at $\theta_a < \theta < \theta_b$ is modelled using the following function:

$$P(\theta) = \Theta(P_b - P_a) + 0.1\sqrt{P_a^2 + P_b^2}\sin(\pi\Theta), \tag{4.4}$$

where

$$\Theta = \frac{\theta - \theta_a}{\theta_b - \theta_a}. \tag{4.5}$$

The bottom surface distribution can be modelled linearly, in the jet only case, with a change of gradient at θ_b. The pressure magnitude is modelled using a polynomial fit. In a purely rotational case, a fourth-order Gaussian fit (as shown in equation 4.6, where n is the order) is used to approximate the pressure distribution.

The fit is chosen in the case of $\Omega = 10$ Hz and is shown in figure 4.7. The scaling is done using a polynomial fit of the mean value of pressure distribution at the bottom surface with respect to Ω.

$$y = \sum_{i=1}^{n} a_n e^{-(\frac{x-b_n}{c_n})^2} \tag{4.6}$$

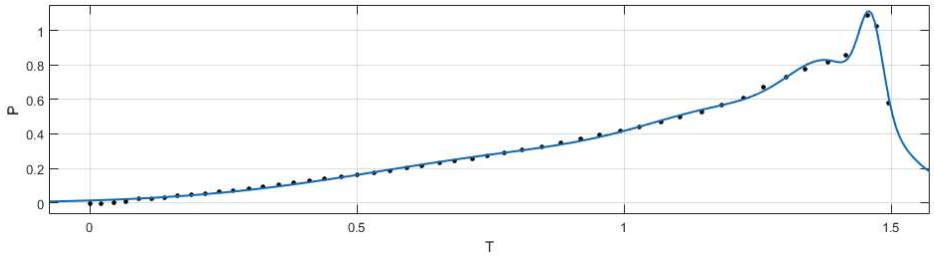

Figure 4.7: Pressure distribution, at $\Omega = 10\ rev.s^{-1}$ (dotted), and Gaussian fit (line).

As for the top surface, it can be assumed that, for B close to 0, the distribution is that of a jet only case. For B closer to 1, the distribution is that of a rotating flow. In the case where both are taken into account, the flowing relationship is created:

$$P = (1 - \bar{U}^2)P_f + \bar{U}^2 P_s \tag{4.7}$$

where $\bar{U} = R\Omega/(R\Omega + U_j)$. However, scaling using the rotation parameter B or Ld does not accurately portray the flow. Further work must be done on this section of the model in order to determine the main variables that influence the bottom surface.

4.2.2 Novel model

The pressure distribution modelled on the novel design can be seen in figures 4.8 & 4.9. One thing to note is that the top left plot in both figures represent the same data point. In figure 4.8, the increased angular velocity affects the pressure distribution on the surface in two areas. At the beginning of disk (low θ), the pressure increases on the top to reduce the total pressure gradient acting in the region. For $\theta > 0.5$, higher angular velocities decrease the pressure on the top surface while increasing it on the bottom. In this region of the disk the pressure gradient across the disk increases with angular velocity. Furthermore, the pressure variation due to spin is much less significant than in the traditional design's model.

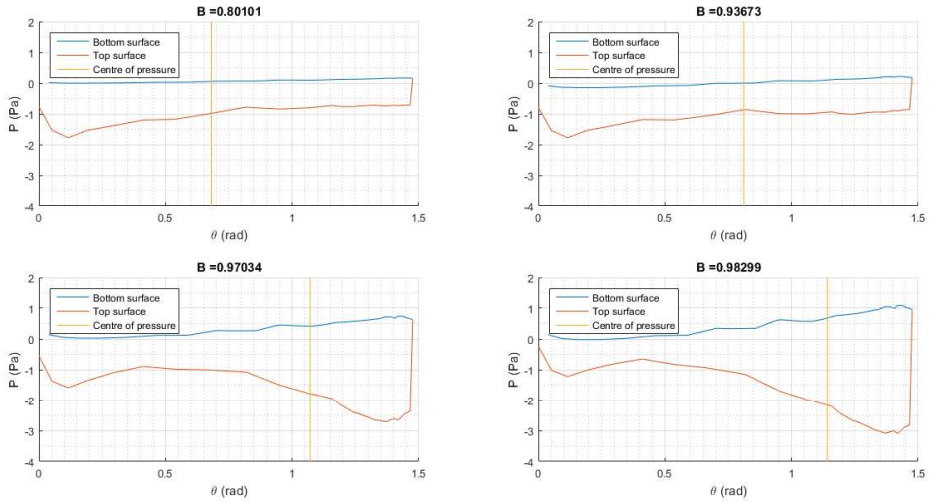

Figure 4.8: Pressure distribution generated by the computational novel design model with an increasing angular velocity.

Figure 4.9 shows the variation of pressure distribution with an increasing jet velocity input. The variation in pressure is much greater due to jet velocity. It can be noted that the increase in pressure gradient is affecting the whole disk, with the highest peak at the surface's start. Contrary to the spinning case, the bottom surface is not affected by a change in jet velocity.

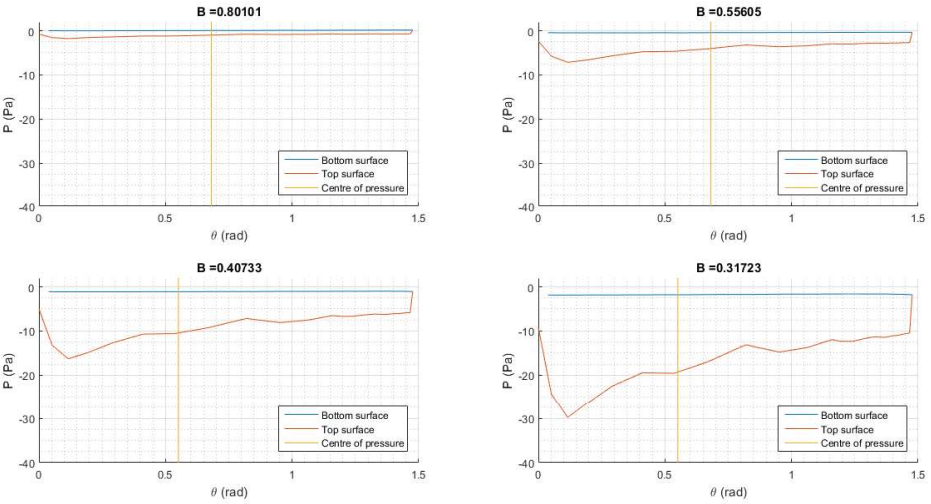

Figure 4.9: Pressure distribution generated by the computational novel design model with an increasing jet velocity.

4.3 Lift Generation

Using the experimental setup described in the methods sections, a set of parameters were used to map the range of lift generated by the novel design. The examined parameters in this section were the jet velocity and the disk rotation. Jet flow rate could not be directly controlled due to turbulence which prevented the use of a stable feedback loop. Disk angular velocity however could be controlled using a feedback loop as the variance of angular velocity due to disturbances was minor.

Each test made in this section lasted two seconds. The sensor was reset between tests, and fifteen tests were conducted per data point to ensure a good measurement as the vibrations were quite substantial. As seen in figure **??**, their magnitude may exceed 2N at high jet velocities.

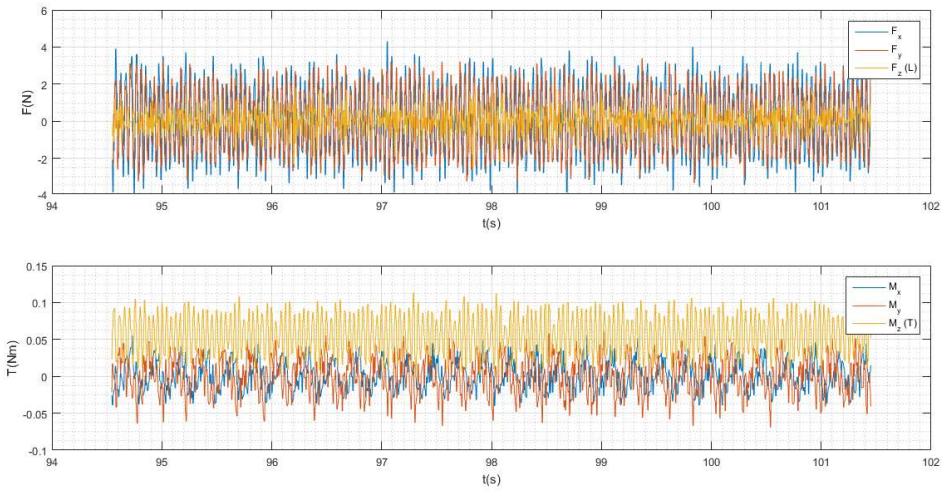

Figure 4.10: Force and torque generated by the system at $\Omega = 30$ Hz and $d = 0\%$.

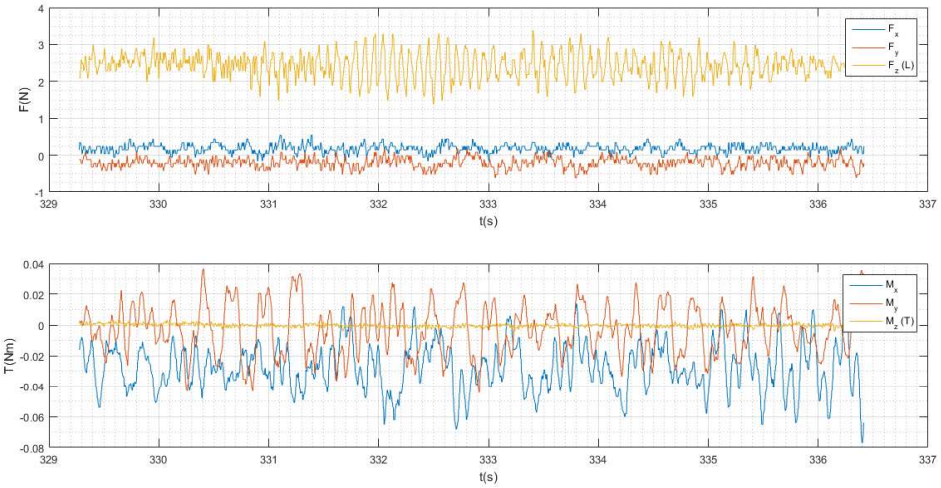

Figure 4.11: Force and torque generated by the system at $\Omega = 0$ and $d = 50\%$.

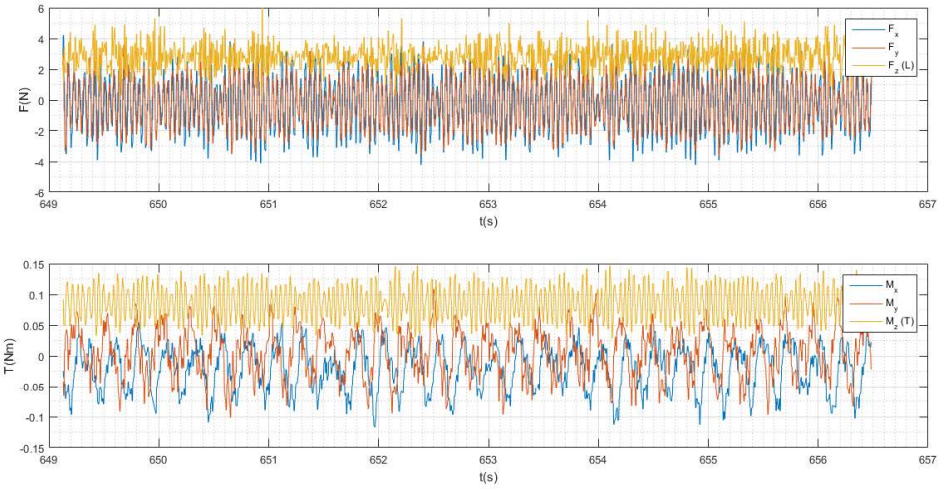

Figure 4.12: Force and torque generated by the system at $\Omega = 30$ Hz and $d = 50\%$.

In figures 4.10, 4.11, 4.12, samples of the forces and moments exerted by the system can be seen. These different samples may be statically invalid without a larger sample size but do describe different aspects of the system quite well. The first two describe the system as pure rotation and pure jet respectively while the third describes it a a combination of both.

Note that in figure 4.10, the moment oscillations present are of a higher frequency and seem more periodic than in figure 4.11. The presence of non periodic variance in

figure 4.11 suggests that flow turbulence directly affects the system. Furthermore, it can be seen that, barring the oscillations, a purely rotating system will generate a torque in the Z, while a purely jet driven system will generate a force in the Z.

Figure 4.12 shows that in a combined environment the oscillations present in both individual systems compound. Vibrations that were not seen in the force measurement of a purely jet condition can be observed in a combined system. Similarly, the torques present in this figure show that both the aperiodicity of a purely jet driven flow and the periodic oscillations of a rotating system are both present. Furthermore, it can be seen that the lift generated in figure 4.11 is not impacted by the addition of disk rotation. Similarly, the torque generated by the disk's angular velocity is not greatly affected by the addition of a jet.

In order to map the lift, torque and other forces for any given set of inputs in a steady system each test, which is shown in figures previously discussed, can be represented by an average value and a variance from the mean. Further analysis of the data is also done by examining amplitudes in the frequency domain using the FFT function in MATLAB.

Two type of error calculations can be found in the lift measurements. The first is due to the vibrations that can be seen in figure 4.10. The second is due to changes between different runs. Both of these are calculated and shown in figure 4.13.

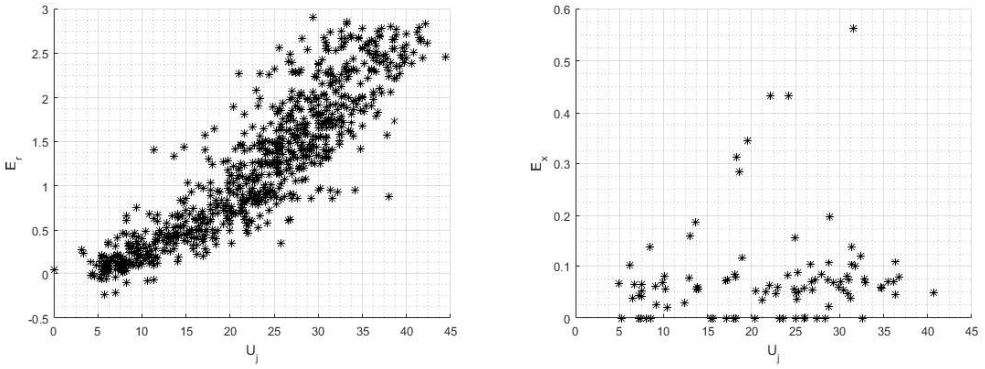

(a) Vibration variation (b) Lift variation between runs

Figure 4.13: Standard deviation of lift measurements

It can be seen that the amplitude of oscillations measured as a standard deviation from the mean increases with a higher jet velocity. The air supply used was not designed for this purpose and the jet leaving the nozzle would be highly turbulent. Higher jet velocity would therefore increase the vibrations experienced by the system. Other oscillations can be observed in figures 4.10, 4.11 and 4.12, such as the moments exerted by the spinning disk. We perform an FFT on the cases shown above: the lift and moment in the x axis will be used as an example.

All experiments were run for 2 seconds at a sample rate of 2 kHz. The FFT was performed using the MATLAB built in function. The magnitude of the complex number returned is plotted against the appropriate frequency domain. A peak finding algorithm is then used to easily identify recurring values.

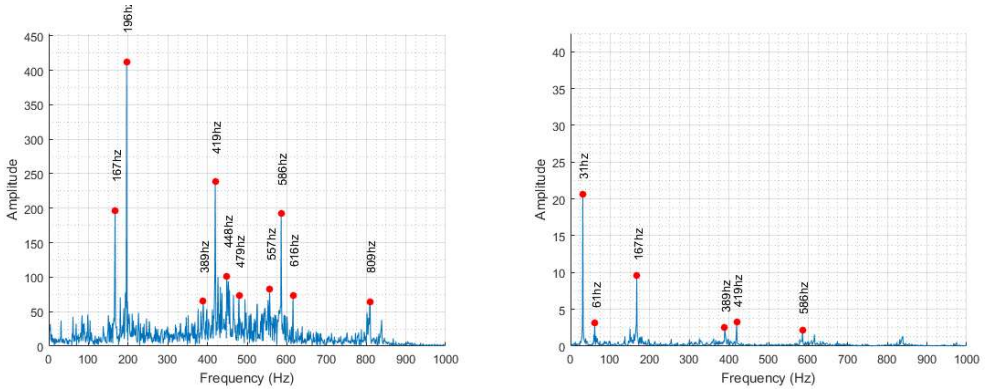

(a) L (b) M_x

Figure 4.14: FFT analysis of $\Omega = 30$Hz, $U_j = 6$ m.s^{-1} and d= 0

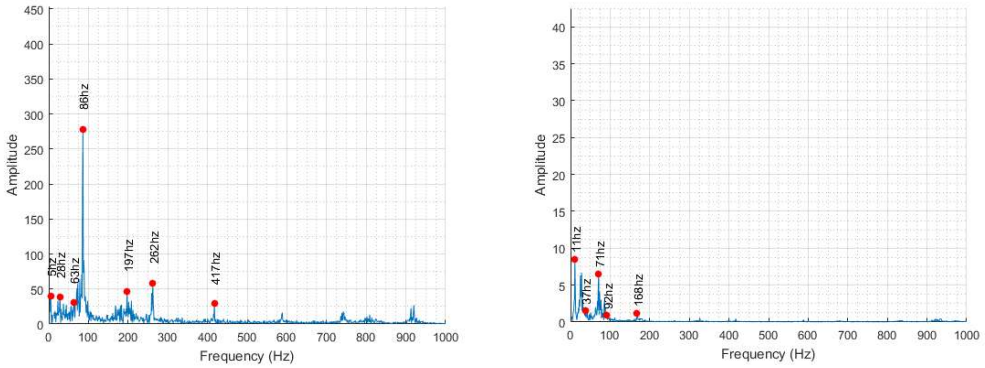

(a) L (b) M_x

Figure 4.15: FFT analysis of $\Omega = 0$Hz, $U_j = 28.8$ m.s^{-1} and d= 50

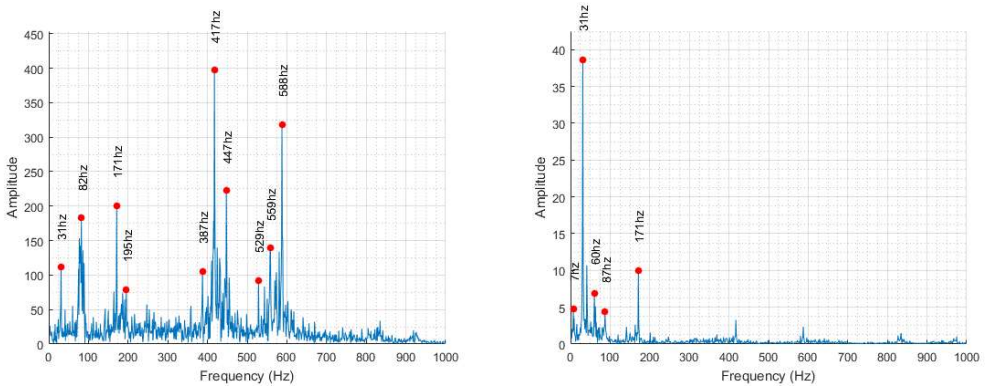

(a) L (b) M_x

Figure 4.16: FFT analysis Ω = 30Hz, U_j = 30 m.s^{-1} and d= 50

The first point to note is that the disk rotation can be seen to have an effect in figures 4.14b, and 4.16. Interestingly, the disk rotation only appears to affect the vertical force component when a jet is already present. Furthermore, in figure 4.15b, the vibrational frequency is quite low, hinting at the formation of large vortices forming over the top surface. They are not present in the CFD, and could be forming due to attachment to the control flap. Control surfaces are continuous around the perimeter in the computational model. In the experimental setup, the flap protrudes out the housing which could be causing vortex formation. In order to determine if an underlying mechanism is generating some of the forces in this system, the frequency analysis can be averaged for the experiments with the same parameter set.

The presence of a persistent vibration of the moments M_x was found throughout the experiments with no disk rotation at the frequencies of 12, 26 and 71 Hz. This could be due to some harmonics of the fan's wake. Furthermore, in the cases where fan wake influenced the lift measurements we can map the motor frequency to set duties, this can be seen in figure 4.17.

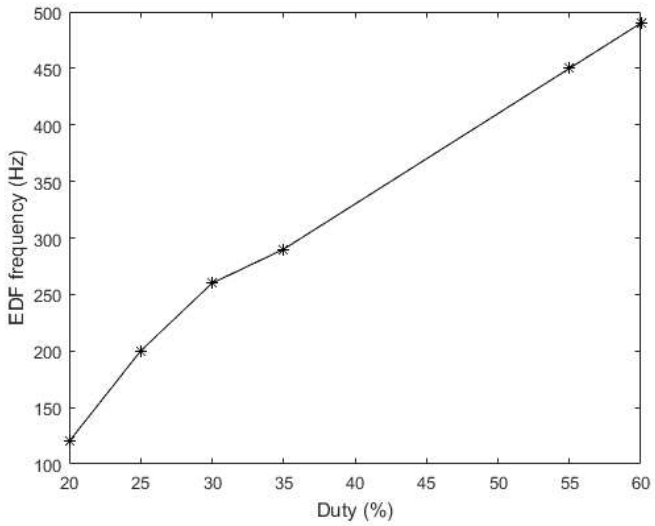

Figure 4.17: Motor frequency as a function of duty.

Using equation 3.94, we can calculate the mass flow rate for the experimental results. The mass flow rate for the computational data be can calculated using the following equation:

$$\dot{m} = 2\pi x_{in} h U_j \tag{4.8}$$

The lifts measured in both cases are seen in figure 4.18. The data measured from the experiment and the computational model both have disk velocities ranging from 0 to 30 Hz with no noticeable change in lift generated. The disk's rotation therefore does not seem to affect the flow in this regime. However, these initial lift experiments were run at a deflection angle of 0^o from the surface or 45^o for the horizontal plane.

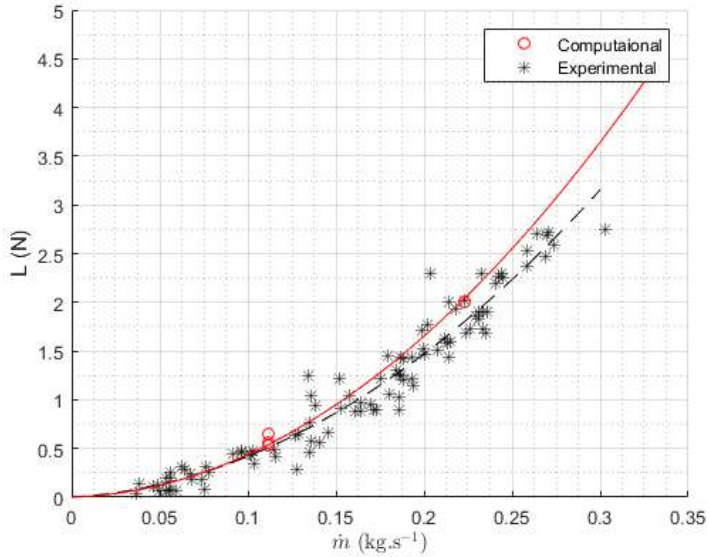

Figure 4.18: Variation of lift with mass flow rate

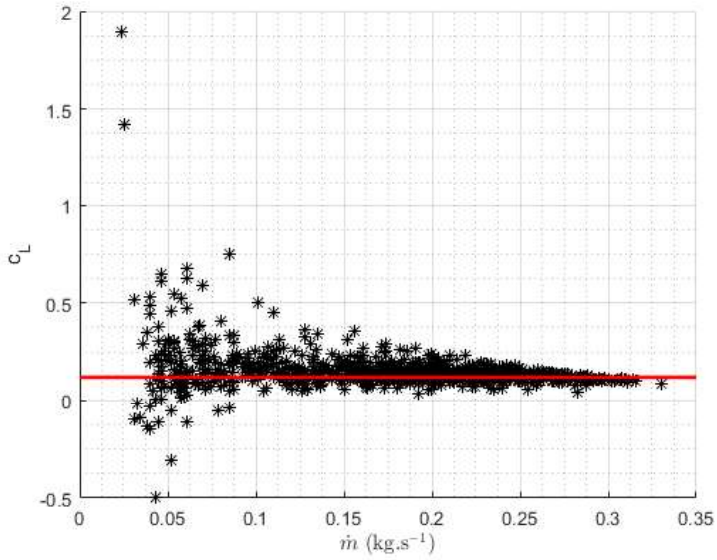

Figure 4.19: Lift coefficient with respect to the mass flow rate

Using equation 3.5, we can calculate the lift coefficients. They can be seen in figure 4.19. It can be seen that the lift coefficient at higher mass flow rates tend towards a certain value. By taking the mean value of the coefficient for duties higher than 50, it is calculated to find $c'_L = 0.073$. Disk rotation was initially thought to

cause the lift coefficient variation that is seen at lower mass flow rates. However, the variation seems to be due to unsteadiness. At lower jet velocities, the FFT analysis of the moment in x exhibit the same peaks as seen in figure 4.27a. This will be further discussed in chapter 5.

The lift coefficient is thought to be tending to a constant (c'_L) for this flight configuration within this aerodynamic regime. The aim of control surfaces on this design is to vary the lift coefficients on different sections of the disk to generate control pitch and roll moments.

Generating the flow necessary to generate a significant amount of lift will produce a yaw moment by the central radial compressor. In order to balance the compressor and generate control moments in the yaw axis, the disk rotation is used. The torque generated by the rotating surface can be seen in figure 4.20. within the range that has been tested, the torque does not seem to be affected by the jet velocity, but purely by the Ω.

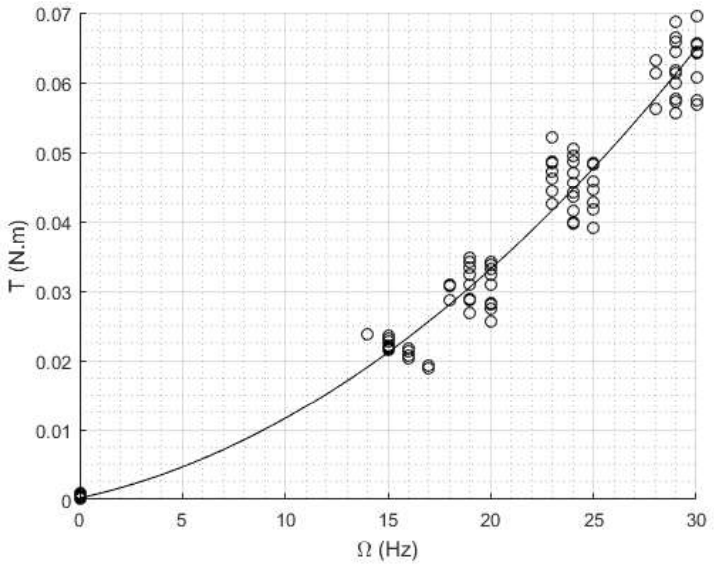

Figure 4.20: Variation of torque generated with respect to the angular velocity of the disk.

4.4 Control results

4.4.1 Computational

The recorded lift coefficients were corrected using equation 3.85 and can be seen in figure 4.21a. The curve resembles the lift curve of an aerofoil therefore the slope will be defined as $b = 0.0015$. It is calculated by taking the average gradient in the middle section and is shown in figure 4.21a. $c_{L0} = 0.0676$ in this system configuration. Similarly, using the estimated lift coefficient response we can calculate the predicted experimental $b = 0.0005$. This is because the of the change in affected area as explained in section 3.2.2.3, 1/4 of the disk for the CFD and 1/3 for the experimental.

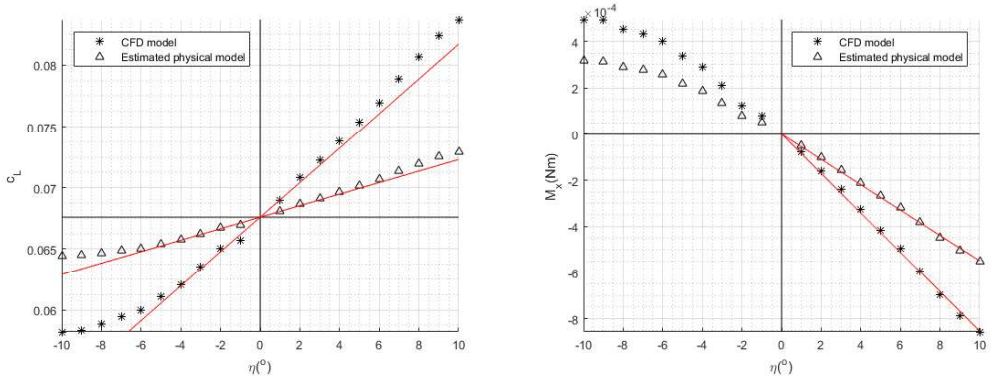

(a) c_L and the lift curve. (b) Moments and simplified model

Figure 4.21: Control model in the case of $U_j = 5$ m.s^{-1} and $\Omega = 5$ Hz.

The moments generated in the configuration studied can be seen in figure 4.21b. The regions with negative beta are clearly non linear. This could be due to the centre of pressure position varying. In positive control angles (η) we can estimate a linear fit with a gradient of $\delta M_x = 8.5346\text{e}^{-5}$ Nm/^{o}. This moment response is due to the quarter of the disk being affected by the control action. In the experimental setup the area that would be affected is different, therefore the moment would be different. In the experimental setup, the controls are separated into three areas. Furthermore, the control surfaces only span 40^o. The estimated moments generated can be calculated and are shown in figure 4.21b. The experimental setup is expected to produce $\delta M_x = 5.4859\text{e}^{-5}$ Nm/^{o}.

The lift coefficients shown as the CFD model are the values generated as c_{LT} which should be the maximum c_L response. The total affected area in the experimental setup is a third of the total area. As for the M_x, the area affected by one control surface is 90^o and 40^o for the computational and experimental models.

4.4.2 Experimental data

Between the experimental tests discussed in the previous section and the results that follow, the jet had to be dismantled for repairs and maintenance works. The control angles referred to in this section are not accurately correlated to the one before this.

The experimental procedure is intended to be identical whereas rather than varying the disk velocity, all of the control surfaces were changed in unison. The margin of error for η is +/- 5^o from the absolute measurements of the horizontal. This is due to the curvature of the flap, among other constraints. While this accuracy would be preferred, it is not necessary for a control system. While being constrained to a stable linear region (as seen in figure 4.30), the controller only needs to increment in the desired direction.

The lifts generated during these tests are shown in figures 4.22 and 4.23. The tests at Ω = 30Hz were not completed as can be seen in figures 4.23 and 4.24. The lift generated by a non spinning configuration with η = -5^o varies drastically at low jet velocities and levels out at high flow rates. During testing this was noticed, and placing a hand over the compressor revealed by observation that the air would be travelling upwards. The flow's attachment to the control surface caused a full separation from the disk and redirected it upwards. Another point of note was the high lift produced at $\eta = 5^o$.

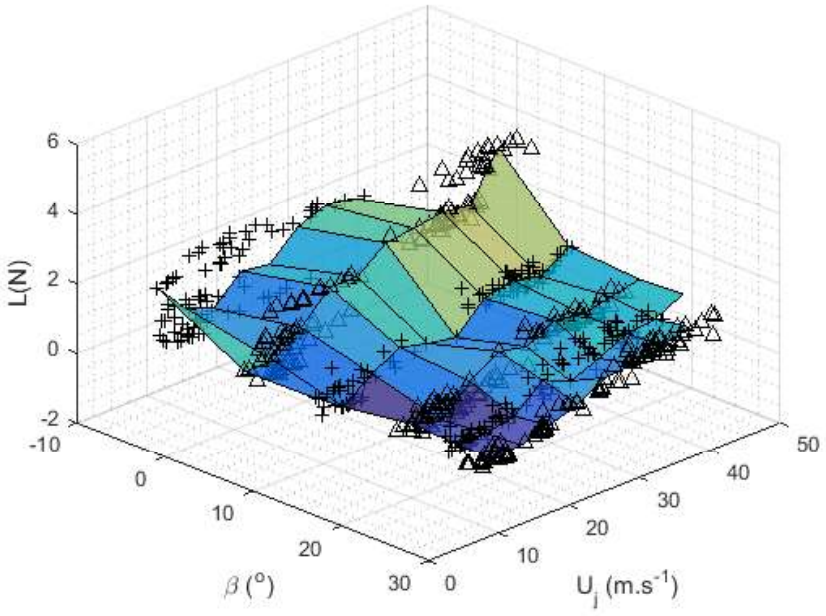

Figure 4.22: Lift variation with control angles at Ω = 0.

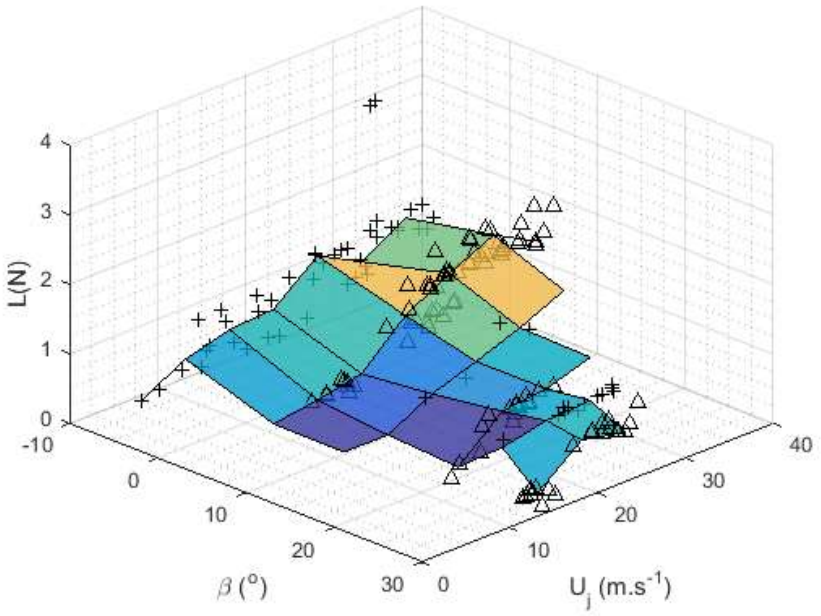

Figure 4.23: Lift variation with control angles at Ω = 30 Hz.

The lift coefficients produced by the various test conducted can be seen in figure 4.24. The red lines show the estimated tending lift coefficient (c'_L). For the incomplete dataset, c'_L is just calculated using the mean lift coefficient of the available data. c_L at η = -5^o varies more at low jet velocities for the stationary configuration than a rotating one. This can be due to increased adhesion to the disk caused by the boundary layer formed by the rotation.

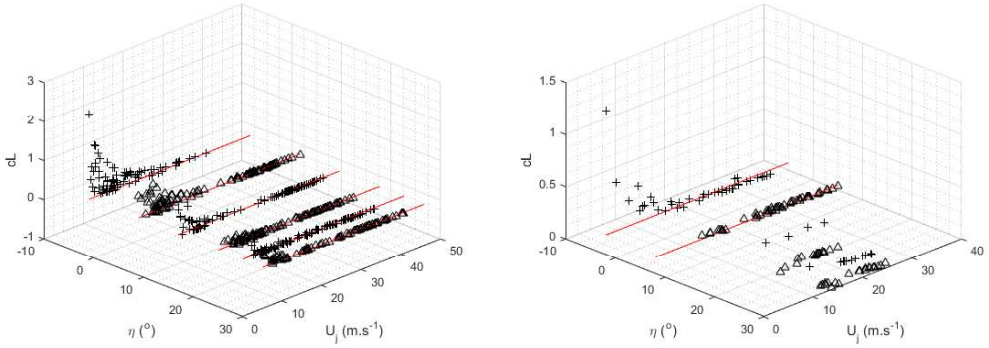

(a) Ω = 0. (b) Ω = 30 Hz.

Figure 4.24: Lift coefficient variation with control angles

Let us take the cases with the highest and lowest lift produced in the configuration $\Omega = 0$, $d = 20$, and $\eta = -5^o$. The parameter averaged lift in cases 1 and 2 referred to in figure 4.25 is the average lift over all fifteen tests that were conducted with these parameters. The main difference that can be observed between figures 4.25b and 4.25a is the presence of large oscillations.

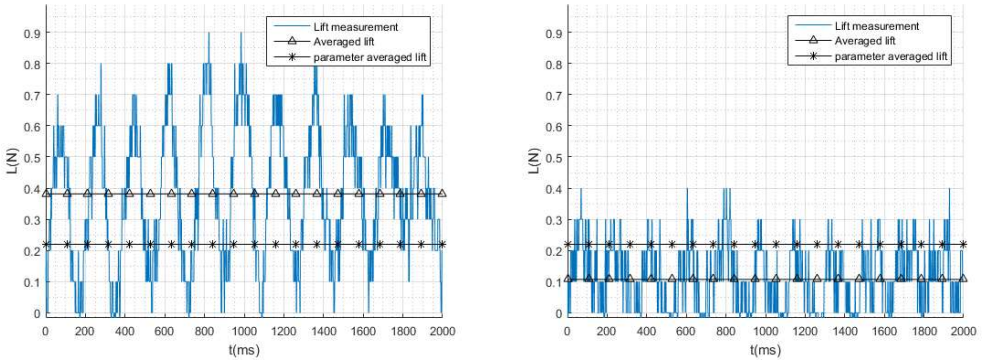

(a) Case 1. (b) Case 2.

Figure 4.25: Lift as a function of time.

The oscillations are present in figure 4.26. One notable difference that could hint at the source of the amplification is the distinct off-phase oscillation in the x and y directions. The moments in figure 4.26 do not exhibit a visual dominant frequency. Off-phase moments as seen in figure 4.26 can only be observed under two conditions. Either the global centre of pressure is not in the centre-line of the disk or the centre of pressure should be rotating around the disk. This could be explained by vortex shedding from the control surfaces.

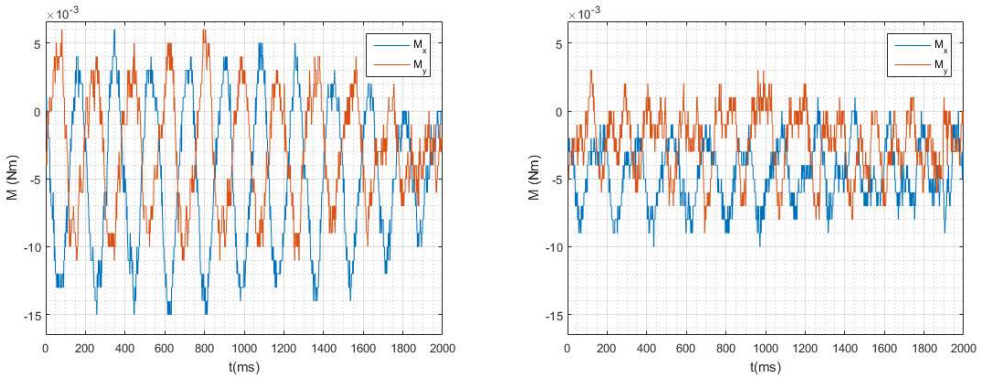

(a) Case 1. (b) Case 2.

Figure 4.26: Moments as a function of time.

The FFT analysis of the lift and moment in all directions is similar, therefore let us just look at M_x in figure 4.27. The amplitude recorded at a frequency of 12 Hz is much greater in case 1. Interestingly, the amplitude at a frequency of 24 Hz is higher in the second case. With the information from figures 4.26 and 4.27, we can determine an apparent mechanism for the unsteady regime.

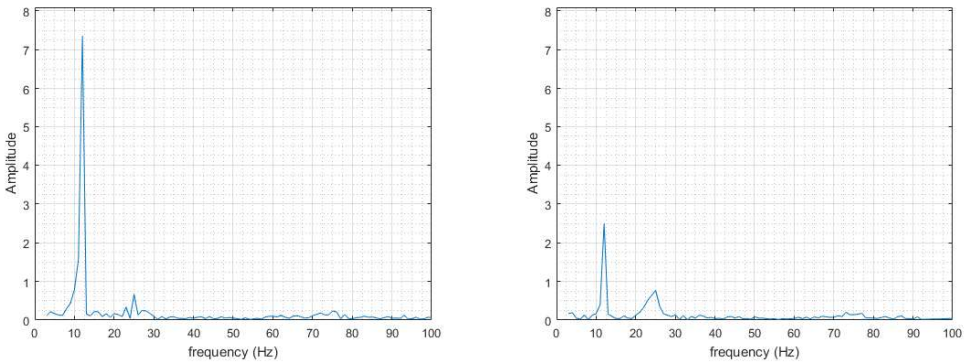

(a) Case 1. (b) Case 2.

Figure 4.27: FFT analysis on moments in x.

In the first case, large vortices seem to be forming at a frequency of 12 Hz generating a larger amount of lift than would be experienced than in a steady system. This is discussed in more detail in chapter 5. The second case shows a system where the eddies broke up and energy was transferred to the second smaller faster oscillating vortices. This shows that the system in this configuration is unstable.

The particularly high lift coefficients observed for $\eta = 5^o$ appear to stem from high frequency harmonics as seen in figure 4.28b. This is the only configuration of η in which more than two peaks occur at such high frequencies. Frequencies that consistently experience high amplitudes in this configuration are 420, 470, 530, and 580 Hz.

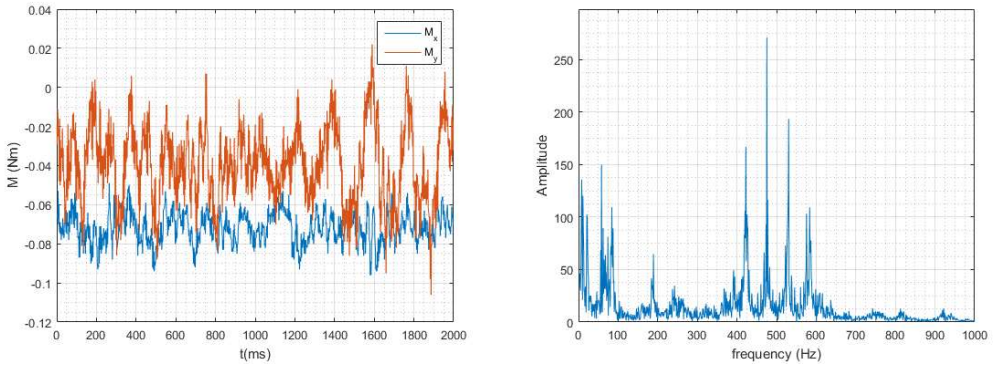

(a) Moments produced. (b) FFT analysis of the lift produced.

Figure 4.28: data for $d = 55$, $\Omega = 0$, and $\eta = 5^o$.

The influence of the EDF's wake must be the cause of a high c_L in this control configuration. This deduction is made by correlating the range of frequencies in figurse 4.17 and 4.28b. Furthermore, all of the tests conducted at η = -5^o and 0^o and $d = 55$ exhibit dual amplitude spikes at about 450 and 500 Hz. With a control angle of η = -5^o harmonic aero-mechanical resonance seems to occur. This agrees with the presence of two peaks at 420 and 580 Hz in figure 4.14. These frequencies probably represent the mechanical resonance of the carbon fibre disk.

The steady state system can be represented by figure 4.15. The energy distribution through frequency domain is more even. In most case peaks will be present at 12, 24, 86, 171, 420 and 580 Hz. Vibrations at a frequency of 86 Hz are not present in an unsteady regime. However, they can be observed in all steady state measurements taken. This frequency is probably due to the duct geometry. At a high enough nozzle pressure gradient, the flow exits in a steady state turbulent flow. This resonance's frequency is probably associated with the aspect ratio of the nozzle. furthermore this frequency is never observed at lower jet velocities. When the jet velocity exceeds a certain amount this frequency is present. This could explain the drop seen in the transition phase in figure 4.30a.

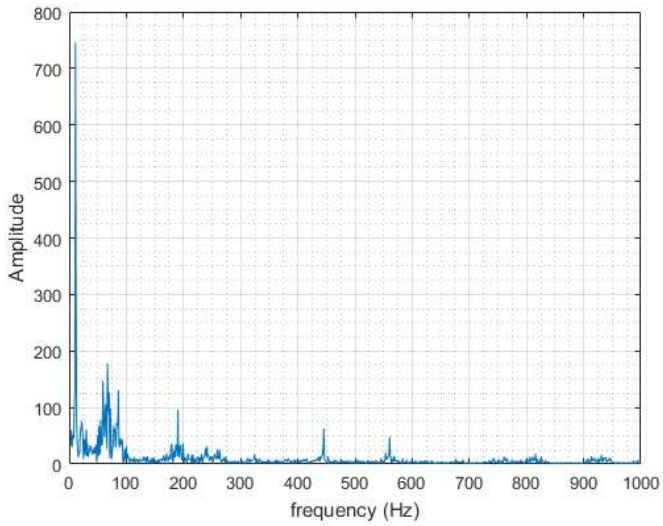

Figure 4.29: FFT analysis of the lift generated for the case of $\eta = 26^o$, $d = 55$, and $\Omega = 0$.

Figure 4.29 shows the FFT analysis for a configuration that is stalling. One notable difference between this and a stable regime, is the lack of a distinct peak at 80Hz. This phenomenon is also observed in figure 4.28b, it seems to mark the transition in and out of the stable regime. In the case of a stalling configuration, the adverse pressure gradient at the nozzle may be too great. This could explain the loss of efficiency through the system.

Figure 4.30 shows c'_L values and hypothesised flow regimes that have been observed during testing. The high lift coefficient experienced in the stationary configuration of $\eta = 5^o$ is thought to be due to an unsteady aerodynamic phenomena. Furthermore, figure 4.22 shows a wide range of lifts generated for any given jet velocity in the case of an open control surface. In the case of a rotating system, unsteady behaviour is not observed in the lift measurements. Before starting the experiments, the flow regime was expected to remain within the stable region as seen the CFD results.

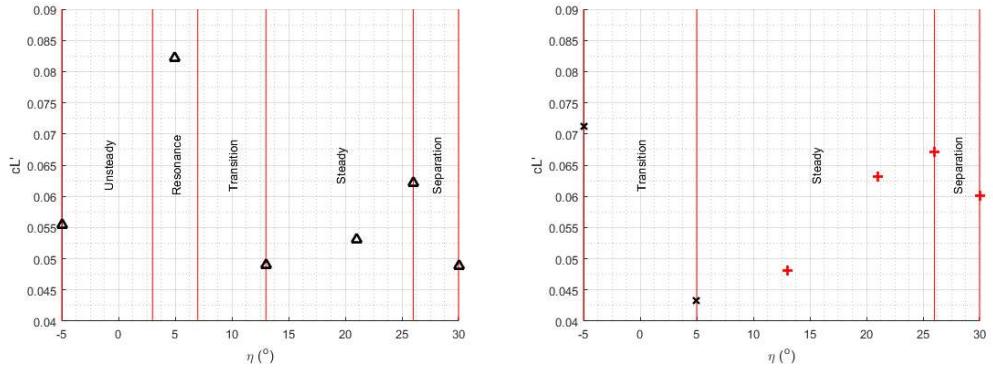

(a) $\Omega = 0$. (b) $\Omega = 30$ Hz.

Figure 4.30: Mean lift coefficient with respect to the control angle used and hypothesised flow regimes. The red markers show the less accurate measurements.

For $\Omega = 0$, b is calculated to be 0.001 in the region of $13^o < \eta < 26^o$. For $\Omega = 30$ Hz, assuming the region between $\eta = 13^o$ and 21^o is linear and the same regime as figure 4.21a, b is calculated to be 0.0019. This value is much greater than the value estimated from the computational model.

Chapter 5

Discussion

Results presented in this report show the underlying mechanisms of a rotating Coanda based craft. Two designs are investigated to varying degrees. This chapter will first discuss the results presented in the previous section. Then, the design choices made along with their physical implications and possible improvements. Finally the control implementation will be discussed.

5.1 Results Summary

The boundary layer and pressure distributions generated by the computational model are initially compared to the various analytical models discussed. The behaviour of the flow is directly reflected in the pressure distribution. Using this insight, the experimental results will be discussed and compared to their computational analogue. Key aspects of the system observed in the experimental lift measurements will be determined. In conjunction with the computational control data, the experimental data is examined. Forces and moments share similar oscillation frequencies over multiple experiments in most data sets. Finally, the different modes are discussed.

5.1.1 Boundary layer and pressure results

The boundary layer velocity profiles in figure 3.12 closely resemble those generated by the computational model of the traditional design seen in figure 4.1. In this instance, the tangential velocities are the most important variable to compare as it is representative of the flow behaviour. However, one difference is radial expansion. Since the mathematical model is two dimensional, if $x_{in} << x_m$, or U_j is too small, the boundary layer loses too much energy and separates. If the flow regime does not change, which it does not appear to, the two dimensional model can be used to

calculate the full model's boundary layer velocity profile. Radial expansion can be taken into account by multiplying the tangential velocity with x_{in}/x.

Furthermore, the flow generated by a flat rotating plate seen in figure 3.14 closely resembles the computational results shown in figure 4.2. Specifically, the transverse velocity profile. Due to the curvature of the surface, it could therefore more likely be compared to a rotating sphere [35], indeed the tangential and radial velocities (V_θ,V_r) are similar to the ones seen in this paper [35]. In the case of $\theta \sim \pi/4$, centrifugal forces acting on the fluid were seen to cause an outwards eruption of the boundary layer, much like a rotating sphere. The model should be adjusted in the future to account for a greater distance from the centreline.

In figure 4.3, influence of the two sources of energy on the boundary layer can be observed. Using a non-dimensional transformation on the velocity, predictable flow regimes are observed. The boundary layer transitions continuously from a state of jet to rotationally induced flow. The rotation parameter B is introduced to estimate the flow state. This variable varies from 0 to 1 or from purely jet to purely spin.

The pressure distribution and centre of pressure of the traditional design computational model can seen in figure 4.5. The change of pressure profiles is assumed to be continuous from $B = 0$ to 1 if there is no regime change. Both the computational and mathematical models may fail to accurately model turbulence that may lead to separation.

An in depth analysis of the pressure distribution generated by the novel design was not conducted. The in depth pressure analysis was conducted before the design was iterated. Figure **??** can give us some insight into the similarities and differences between the two designs. First of all, it can be assumed that, like the traditional design, the jet's influence is greatest at the centre and dissipates outwards. On the other hand, the rotation influence is weak in the centre and increases outwards. The novel design's pressure distribution is therefore also assumed to continuously transform from $B = 0$ to 1. The jet only pressure distribution seen in figure 4.4 closely resembles the one in figure 5.1. However a direct comparison cannot be made as it is not clear exactly what jet velocity is used. Furthermore, the dimensions and reference frame used by the team are different. Their disk is larger, and they are plotting against x not θ.

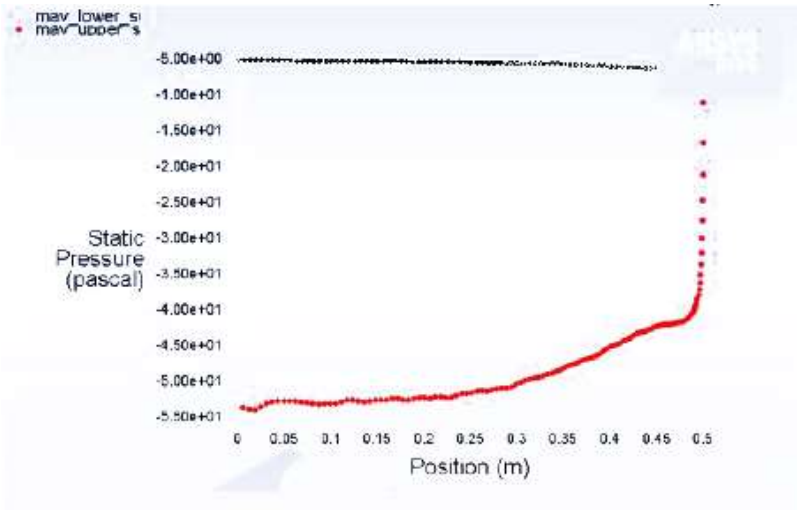

Figure 5.1: Pressure distribution modelled by another team [27].

In a jet only situation, both designs would experience very similar flows. However, the fluid expansion would have a slight effect on the velocity profiles, because $\delta\theta/\delta x$ is not the same for both designs. The flow at a given θ would experience a different expansion depending on the design. Furthermore, the jet angle leaving the disk plane is different for both designs. The traditional design redirects all of the remaining jet downwards contributing to thrust. The novel design's exit angle is $\pi/4$, limiting the vertical force to $1/\sqrt{2}$ of the traditional design's. Similarly, the lift generated in a traditional jet only configuration is limited, compared to the novel design, due to the reduced horizontal disk area. In the old design, potentially lift generating pressure differences are wasted pulling the disk's edge outwards.

Looking at a purely rotating system, the downstream half of the novel and upstream half of the traditional designs would be influenced in the same way. The new model experiences higher pressure in the top surface of the inner half of the disk as seen in figure 4.9. Here, the centrifugal forces acting on the fluid creates a higher pressure than a flat surface would. On the bottom surface, a lower pressure is measured in that region, and induced radial flow away from the surface due to the rotation is experienced. The pressure gradient across the surface is dependent on its concavity or convexity.

5.1.2 Lift tests

The first series of experimental tests consisted of inducing a jet only flow on the rotating disk with $\eta = 0$. Three-axis forces and moments were measured through the load cell. Computational data was generated using the same configuration. However, the velocity profile at the jet nozzle is flat: this is accounted for by comparing

the forces with respect to mass flow rate. Another difference between the computational and experimental models is the control span Δ. Computationally, they cover the entire circumference, whereas experimentally, they cover 120^o. Gaps between the control surfaces are thought to cause unsteady flow under certain conditions. Furthermore, the sharp upward turning in the nozzle, flow may be exiting at a shallower angle than the ideal 45 ^{o} condition used in CFD. This effect is most noticed by the offset of control surface response.

The lift results can be divided into two sections. The first of these is the case study, where three cases were selected: a spinning only, a jet only, and a combined configuration. These cases are selected in order to better understand the system's range of response. The second section consists of aggregating the data, determining the lift curve and comparing it to the computational model.

5.1.2.1 Case study

Figures 4.10-4.12 show the data measured in three different configurations. The chosen data points represents the three possible states of the system. A purely rotating configuration, seen in figure 4.10, exhibits no apparent directional forces. However, a moment is clearly observed in the third dimension. This torque is produced by the aerodynamic friction acting on the rotating disk. Furthermore, two distinct oscillatory frequency are observable in this figure: a high frequencies vibration exhibited by all channels while moments in x and y exhibit what seems to be vibration at the frequency of rotation.

Figure 4.11 depicts clear lift generation with negligible horizontal forces in the case of a jet only flow. The lift exhibits a clear steady vibration, which is thought to be directly linked to the frequency at which the compressor runs. The observed moments vary with no clear frequency or oscillatory pattern. This could be the product of a turbulent flow exiting the compressor. No torque was measured in the third dimension, as the disk is free spinning when the motor is not powered.

Much like the velocity profiles and pressure distribution results, the jet and rotational effects are compounded. Figure 4.12 shows aspects of the two previous figures: firstly, the lift in figure 4.11 and torque in figure 4.10 are both present. Secondly, the high frequency oscillation in the horizontal forces, due to the disk's rotation present in figure 4.10, can be observed. In figure 4.12, the moments in x and y seem to exhibit both the disk's angular velocity and unsteady aspects of figure 4.11.

Figures 4.14-4.16 show a vibrational analysis performed on the dataset using a fast Fourier transform. This analysis is performed in order to isolate different aspects of the flow and better understand the underlying mechanisms affecting the system.

Interestingly, the disk's angular velocity is observable in figure 4.14b but not

figure 4.14a. However, the high frequency oscillation previously discussed can be seen in both these figures. The visible peaks are located at 167 Hz, 419 Hz and 586 Hz. These oscillations are thought to be the structural harmonic frequencies of the disk. Spinning the disk, much like taping it, causes an excitation. The structure response is to vibrate at its resonant frequency. This frequency is present, with a varying degree of amplitude, in every dataset.

Two notable frequencies in figure 4.15 are 89 Hz in the lift and 11 Hz in the x moment. The first is thought to be the frequency of a steady turbulent flow exiting the nozzle. The second is thought to be attributed to vortex shedding off the control surface. Data discussed in the following section further illustrates these two points. Furthermore, a small peak can be seen at a frequency of 417 Hz. From figure 4.17, we can stipulate that it is probably due to the fan's wake.

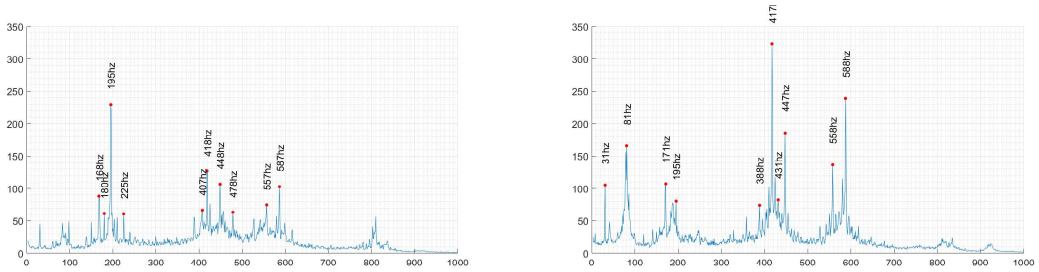

(a) $\Omega = 30$ Hz, $d = 0$.

(b) $\Omega = 30$ Hz, $d = 50$.

Figure 5.2: Aggregated FFT data of the lift measurements.

Figure 4.16 shows the FFT analysis of the combined configuration of both previous cases. All but one of the frequencies previously discussed are visible here, 11 Hz. This is explained by the disk rotation dissipating the vortices previously mentioned. Furthermore, the amplitude of high frequency oscillations present in the lift measurements (417 Hz and 588) are both greater than in figure 4.14. The increase cannot be accounted with pure addition of the amplitude present in figure 4.15a. This hints at some type of harmonic resonance. This can also be observed in figure 5.2, where the FFT data is aggregated for all tests run at the specified configuration.

5.1.2.2 Uncontrolled experimental data

The uncontrolled experimental data is first aggregated to produce figure 4.17. By examining the average FFT value for all the tests done without any disk angular velocity, we can determine the frequency at which the jet operates. The methodology used to generate these results is the same as figure 5.2. Furthermore, the operational frequency seems be in the same range as the structural resonance previously discussed.

Figure 4.18 shows the lift with respect to the mass flow rate for both the computational and experimental data. The mass flow rate is used to counteract the previously discussed difference between the computational and experimental velocity profiles. In this figure, the sets of results shown are very similar. The lift variation presented in the results also concurs with other teams [26, 28] as seen in figure 2.4.

The lift coefficient further describes the possible flight configurations. In a controlled system, c_L appears to converge towards a specific value as the mass flow rate increases. The configuration-specific lift coefficient c'_L, in this case, is estimated to be 0.073 in this case. Because it is independent of both rotation and jet velocity, we can assume it a geometric property. Parameters that can affect the lift coefficient are the aspect ratio AR, the curvature C, and the nozzle height h. Another way the flow can be affected is the variation of η. While similar to changing h, varying η also deflects the flow. Due to the attachment, flow will attempt to follow the flap. A change in nozzle height would not affect the flow direction.

The torque measurements necessary for the yaw control of the craft are seen in figure 4.20. The torque generated follows a continuous parabolic curve. The disk, therefore, can be used as an anti torque for the compressor. Using this curve, a controller can be implemented to counter a large range of torques. Due to the similarities between the lift and torque curves, we can also infer that this mechanism will scale with the power of the compressor. This assumes that the torque produced by the compressor correlates linearly to the lift.

5.1.3 Control data

Over multiple design iterations, the experimental configuration deviated from the computational model used. The size and geometry of the disk and jet nozzle have been conserved, but the geometry and number of control surfaces have changed. The CFD model contains four flaps spanning 90^o each. The experimental setup uses only three flaps, each spanning 40^o. The difference in number and span can be taken into consideration using methods described in chapter 3. One difference that cannot be taken into account is the effect of gaps between the flaps. This section will first discuss results gathered computationally, followed by a discussion on the experimental data, and a description of the observed flow regimes.

5.1.3.1 Computational

As can be seen from figure 4.21a, the lift coefficient varies linearly when η is positive. In the negative region, the gradient decreases with η. In figure 4.21b, the moments generated behaves similarly to the lift coefficient. Constraining lift within the linear regime will facilitate control of the system.

Due to differences with the experimental setup, an estimate of the lift coefficient

variation is also shown in figure 4.21a. The computational model's flap actuation affects three times more area than the experimental model. Assuming no regime change occurs, the change in lift generated would therefore be threefold in the computational case.

5.1.3.2 Experimental

The experimental dataset produced for the spinning configuration is incomplete. Due to a terminal technical fault, for $\eta > 5^o$, the maximum duty cycle tested is 35%. Furthermore, the absolute accuracy of η is +/- 5 ^{o}, with a relative accuracy of 0.5 ^{o}.

Figures 4.22 and 4.23 present the lift measurements in different control configurations. The most open configuration, in figure 4.22 is observed to have a different lift slope than other configurations. This can be explained by low frequency vortex shedding further explored in cases 1 and 2. Notably, the lift produced is not consistent for a given jet velocity. For $\eta = 5^o$, much higher lift is observed. However, some inconsistency is present at higher flow rates. This is thought to be due to harmonic resonance explored in case 3 seen in figure 4.28.

The lift generated by a spinning configuration, seen in figure 4.23, does not present any signs of unsteady flows forming. Even in the most open configurations, the lift follows a clear curve. This strongly suggests the vortices discussed previously are being dissipated due to the disk's rotation. Furthermore, the presence of upwards flow off the control surface during non spinning test could also be explained by vortices forming on the flaps.

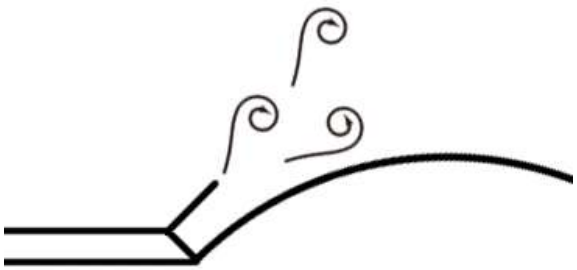

Figure 5.3: Diagram showing the postulated vortex forming.

The lift coefficients can be seen in figure 4.24. The configuration lift coefficient (c'_L) is calculated by averaging the lift coefficients generated at high flow rates. At lower jet velocities, the lift coefficients vary more, reducing the accuracy. Due to the limited data however, c'_L is calculated by averaging all the points in limited datasets. These datasets lack an asymptote in figure 4.24b. Notably, for η = -5^o

in figure 4.24b, all the values of c_L are much greater than the configuration lift coefficient for low jet velocities. This is not observed in any other dataset.

Unsteady regime

Cases 1 and 2 presented in the control section of the results are used to better understand the discrepancy of lift generated at $\Omega = 0$ and $\eta = -5^o$. The first case produced a much higher lift than the second as can be seen in figure 4.25a. The lift also seems to oscillate much more heavily than in case 2. Similarly, the x moment generated in the first case oscillates more than the second, as can be seen in figure 4.26.

The FFT analysis of the moments present in both cases is seen in figure 4.27. The peak present in figure 4.27a is located at 11 Hz. While also present in the second case, its amplitude is diminished. However a secondary peak, located at the second harmonic of this frequency, is observed to have a higher amplitude in figure 4.27b. Furthermore, this peak is less defined that the first. This potentially indicates a more chaotic flow.

In the unsteady regime, the flow seems to fluctuate from case 1 to 2. Due to the large opening of the jet nozzle, the flow would preferentially attach to the flap. It is postulated that large eddies with a frequency of 11 Hz form over the surface. These eddies would dissipate into smaller vortices in the next harmonic. This could explain figure 4.27. Larger eddies generally hold more energy, therefore would create a higher lift, as seen in figure 4.25.

Resonance

In the case of $\Omega = 0$ and $\eta = 5\ ^o$, it seems lifts generated are much higher than all other cases. Figure 4.28a shows a much greater moment about the x axis than the y axis, neither of which are negligible. This is indicative that the high lift is only being generated on one side of the disk. Furthermore, the FFT analysis depicts four peaks in the range of 400-600Hz. No other configuration generated similar results. A greater number of high energy peaks indicates some kind of harmonic resonance. Furthermore, the first peak is located at 417Hz. This frequency seems to be the structural resonance of the disk, it was not statically tested.

This can be caused by the wake. In this case the compressor's frequency is 450Hz. The wake could be exciting the disk at its resonance frequency. The vibrations in turn could increase the lift generated by the system. Similar results were shown using vibrating aerofoils. Vibrations cause vortex shedding on the leading edge. The vortices were found to increase the lift produced by the aerofoil [36]. One possible reason that this phenomenon is not observed in all configurations of $d = 55\%$, is the flap opening. In the case of a smaller η, the flow would preferentially

attach to the flap, rather that the surface. For higher η, the amplitude of vibration due to the wake is reduced, while vibrations of ≈ 80 Hz gain energy. While a much higher lift can be achieved using this process, more studies must be done before this phenomenon can be entirely understood.

Steady state

The non-controlled experiments were framed in a steady regime. One notable characteristic of this flow is the presence of a vibration at 80 Hz. This oscillation is independent of jet velocity, and is only present when the flow exceeds a certain velocity. This behaviour could be due to the nozzle height slightly choking the jet. This would dissipate the compressor's wake. The resulting frequency of the steady turbulent flow would be dependent on the nozzle's geometry.

Separation

The final regime that is observed in the data collected is separation. The main characteristics of this regime can be observed in figure 4.29. Under separation conditions, high amplitudes at 11 Hz are present. This could indicate low frequency vortices forming. Due to the large deflection of the flap (30^o), the jet's relative velocity to the control surface is similar to the unsteady case. Furthermore, the normally distinct peak at 80 Hz is not present. In its place, a range of frequencies have similar amplitudes. This might be indicative of the adverse pressure gradient being too great at the nozzle. The energy normally carried in the missing peak is dissipated over multiple smaller peaks.

Furthermore, the change in lift coefficient due to a control action (b) in the case of $\Omega = 30$ Hz is much greater than expected. This is probably due to the lack of data and inaccurate results. The case for $\Omega = 0$ is more compelling, but b is still much greater than expected. This may be due to the effective length of the experimental flap being longer. An offset can be seen in figure 4.30, as $\eta = 0$ is expected to be in the middle of the stable regime. This can be due to the flow exiting the nozzle at a different angle than expected. In order to improve understanding of the different regimes, more data must be collected, specifically, around the case of resonance, and ensuring linearity within the presumed stable region.

5.2 Design comparison

This section will attempt to compare the traditional and novel designs from the results presented. While based on the same principles, each configuration has different benefits and disadvantages. Furthermore, possible improvements can be stipulated from the observations made in this section.

5.2.1 Non spinning design

Before discussing the effect spinning has on the system, mechanisms present in jet only configurations are discussed for both the traditional and novel designs.

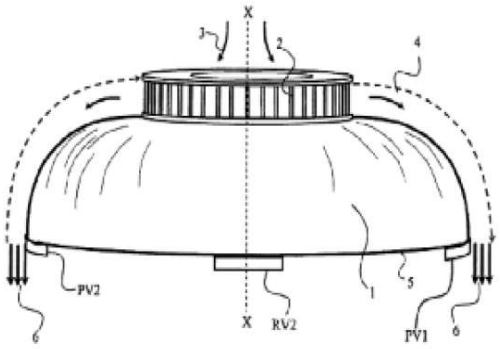

Figure 5.4: Traditional design diagram [2].

The traditional non-spinning configuration currently being researched by various groups [2,25–28] is primarily based on the Coanda effect. Downwards flow generated by the propeller is deflected and blown over a curved surface. The jet follows the curvature due to the Coanda effect. Upwards force is produced due to the jet leaving the surface vertically. Furthermore, entrainment of surrounding air by the jet creates a more efficient jet in the same way a high bypass turbofan is efficient. A larger quantity of air moving slower is more efficient to a small quantity of air going fast. Entrainment slows the jet but adds mass to the flow. Different ways of understanding the mechanisms include looking at the momentum of the flow or the pressure difference between the top and bottom surfaces.

Assuming the flow is stationary at the inlet, the force generated on the body is a reaction to adding momentum to the flow. In this case, it will be sum of the momentum added by the fan and by entrainment. The particles of air at the inlet are accelerated to a given velocity according to their position in the boundary layer. Surrounding air, initially stationary, is also accelerated downwards but to a smaller velocity.

Looking at the pressure acting on the system, it was shown in chapter 3 that the top surface experiences a lower pressure than the bottom surface. The curvature, if not too sharp, will produce the low pressure field necessary to turn the flow along the surface and form an area of low pressure. This is explained by assuming the flow isn't initially affected by the curvature, so that a low pressure area and recirculation would occur between the bottom shear layer and surface. This, in turn, reattaches the flow and exerts a lower pressure on the surface.

5.2.1.1 Novel design

The novel design has a notable disadvantage to the traditional design, the jet exit angle. The curvature's span is 90 ^{o} ranging from -45^o to 45^o. Looking at it from a thrust perspective, this design would, at a maximum, utilise $\frac{1}{\sqrt{2}}$ of the available thrust. This conclusion can be reached by looking at the air's change in momentum. Much like the traditional design, air is assumed stationary at the inlet. Particles would be accelerated much in the same manner as the traditional design, reaching similar velocities at the edge of the surface. However, the particles would be travelling at 45^o from the horizontal plane. The change in momentum contributing to the lift would be scaled, much like the thrust, by $\frac{1}{\sqrt{2}}$.

Looking at the pressure distribution, it seems that the novel design has an advantage. The centre of pressure for both designs is located between $\pi/6 < \theta_p < \pi/3$. Assuming similar flows, the novel design will produce more lift due to the directionality of the force. Indeed, the resultant force vector would be more vertical in the novel design than the traditional design. This contradiction can be explained by the fact that the pump is neglected in this analysis of the system. The pump is used in the traditional design to induce lateral momentum to the flow, while the vertical force is due to interaction with surface. In the novel design, the pump generates a diagonal flow moving up and outwards. This pushes the entire system downwards. In a non-spinning configuration the traditional design seems to be more efficient then the novel one.

5.2.2 Spinning design

The yaw control in the MAV seen in figure 5.4 is achieved using fins seen in figure 2.3a. The propeller produces a swirling flow. The actuated fins redirect the flow downwards. This creates a moment counteracting the propeller's torque. This method of controlling the yaw may not be very effective with higher jet velocities. Spinning the disk can be used as an alternate mode of control.

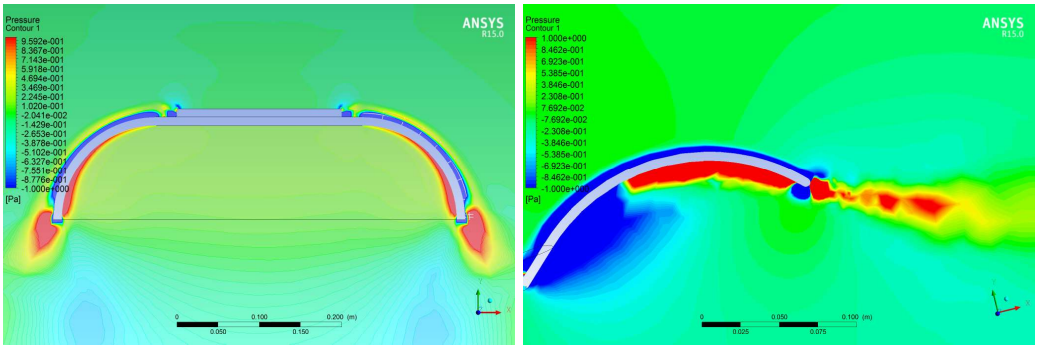

(a) Traditional design. (b) Novel design.

Figure 5.5: Effect of high disk rotation seen on a relative pressure colour map of a 2D slice. The areas in red signify high pressure regions, while the blue ones represent low pressures. Forces in the system act from red to blue.

The disk rotation adds momentum to the fluid radially. In horizontal areas this may increase the momentum of the already existing boundary layer. The rotation's influence is greatest at the disk edge due to its distance from the axis of rotation, while the jet's influence, on the other hand, is weakest as it is the furthest away from the inlet. The flow is therefore flung outwards as can be seen in figure 5.5b and 5.5a.

The traditional model is not compatible with a rotating surface. As seen in figure 5.6, eruption will eject the flow outwards. Thrust from redirecting the jet downwards is lost when rotating the surface. However, in the novel design, the exit angle is closer to the surface (as seen in figure 5.5b angle and does not cause separation. For these reasons the physical experiment was designed around the novel design where the influence of a rotating surface can be examined.

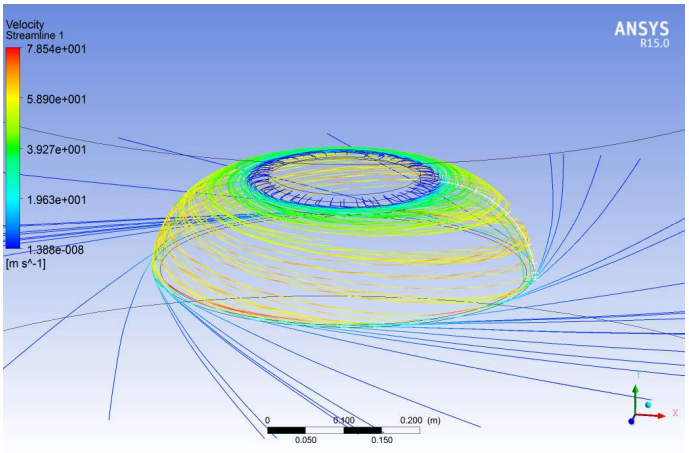

Figure 5.6: Streamlines of air leaving the compressor.

It is important to note that the velocities induced by both sources compound. The individual velocity vectors are normal to each other, therefore, would not slow the flow induced in any given direction. The downwards velocity from the jet is still present, but the added velocity from the rotation is not redirected downwards. This could explain why the disk's rotation has a negligible effect on the lift produced in chapter 4.

5.2.3 Other design considerations

The chosen **aspect ratio**, defined in chapter 3, will affect the design's performance. Because this is a radially expanding flow, the jet velocity in a frictionless system is inversely proportional to the square of the distance travelled. If AR is high, separation can occur due to an adverse pressure gradient. This issue can be easily overlooked if the computational model is two dimensional and the results are extrapolated. Furthermore, if the aspect ratio is too small, very little entrainment would happen and the flow would not be as efficient.

The **cross sectional area** in forward flight of the novel design is smaller. This reduces the drag generated during flight, potentially increasing the maximum flight distance that can be achieved.

Performance enhancing mechanisms (PEMs) can be designed in order to increase the generated lift. As previously mentioned, a considerable amount of momentum is lost to outwards velocity in the novel design. A lip around the outside of the disk redirects the flow downwards. This lip is stationary in order to avoid any extra radial momentum. Using such a PEM, would redirected momentum generated by the disk's rotation, normally directed radially, downwards. This would heavily influence the observed lift curves, as currently rotation does not affect them.

5.3 Control and stability

Discussion of the system's control aspects is first focused on the moments generated and their effect on the system. Due to rotating elements, gyroscopic effects must be taken into account. The potential stability of each design will then be discussed.

5.3.1 Control moments

Two mechanisms are used to generate all the necessary control moments. Pitch and roll are controlled by the actuated flap at the nozzle exit, whereas the disk's angular velocity controls the yaw.

5.3.1.1 Pitch and roll

The flap mechanism tested both computationally and experimentally is shown to produce pitching and rolling moments. Due to the rotation of two components in the system, a nose down pitching moment can have one of three effects. If the angular momentum of the disk is greater than the compressor, the system will precede in the direction of rotation. The same can be said about the compressor. In both of these cases the angular velocity is calculated using the precession equations (eq 3.6). Furthermore, the angular momentum used in these equations is from an external point of view. The system, as a whole, will therefore never exhibit as much gyroscopic effect as if only one of the components was spinning. If the angular momentums were to cancel out, no gyroscopic effect would be observed on the system as a whole. This is because the angular momentum from the point of view of an external observer is 0, and the angular acceleration can be calculated using equations 3.10. However, while no gyroscopic effects are felt by the system as a whole, the shaft connecting the two parts will experience bending moments. If the shaft is flexible enough, precessing is observed to occur.

5.3.1.2 Yaw

In the control investigation that is performed, a rotating surface would be preferred as it completes three purposes. Gyroscopic stability can help reduce angular acceleration and constraints on the controller's performance. Frictional torque produced by the disk provides yaw control and counteracts the compressor's torque. Rotationally induced flow could prevent separation or increase the lift generated. It is observed to stabilise what would be a unsteady flow in a stationary configuration. Furthermore, using a spinning surface provides an additional advantage to anti torque fins. The spinning surface produces torque scalable to the lift generated. This method of control would enable the system to perform well from very small to very large torques. Fins would only work within a narrow torque range by comparison.

5.3.2 Stability

The control mechanisms are similar for both the traditional and novel designs. However, their stability response will vary. The main parameter that will determine the system's stability is the relative position of the centre of mass to the aerodynamic centre. The latter is assumed to be located on the centreline at the same height as the centre of pressure. In an uncontrolled configuration, when a control action is performed, the centre of lift will move horizontally in the direction of the moment. Furthermore, the centre of pressure's position will differ around the disk. In order to simplify the model, we take $\theta_p = \pi/4$ and ignore the effect of control moments. The aerodynamic and mass centres, under these conditions, can be seen for both designs

in the following figures. The centre of mass is assumed to be below the compressor's base. This is where the batteries would be mounted.

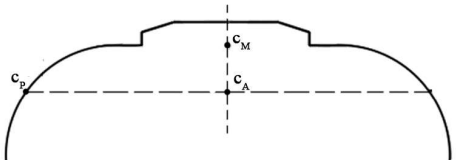

(a) Traditional design.

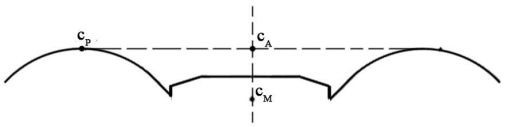

(b) Novel design.

Figure 5.7: Mass and aerodynamic centres of designs.

5.3.2.1 Traditional design

The centre of lift is below the centre of mass in this design. This makes it possible for this design to tip over if the pitch angle is too great. This happens when the weight vector does not pass through the centre of pressure disk as seen in figure 5.8. Other issues can occur if the craft's forward flight velocity is too great. The drag vector would pass underneath the centre of mass, creating a forward pitching moment and increasing the flight speed. This describes another tipping condition of the design. These problems can be overcome by limiting the mobility and implementing an active control system.

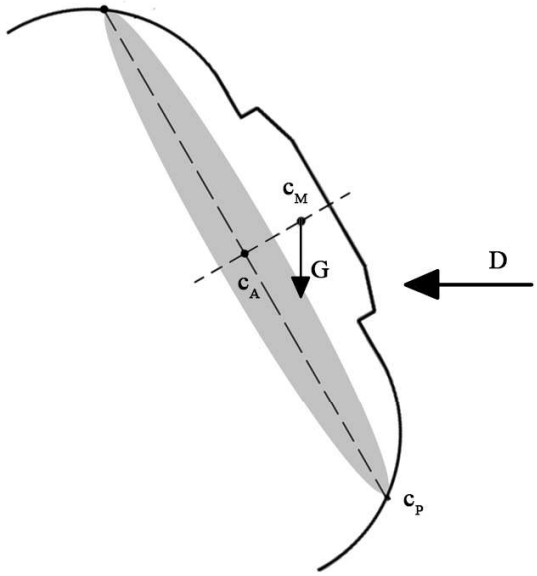

Figure 5.8: Tipping conditions for the traditional design.

5.3.2.2 Novel design

Unlike the traditional design, in this configuration, the centre of mass is located below the centre of lift by a considerable margin as seen in figure 5.7b. This enables the craft to recover from pitch angles greater than 90 ^{o} without implementing active control. In forward flight, the drag vector would pass through, if not over, the centre of mass. This creates a moment counteracting the pitch. The system will inherently attempt to level out. Trim for forward flight can therefore be implemented without the use of an active control system.

Extrapolation and case study

Extrapolating from the data generated by the experimental setup. Assuming the flow regime, and aspect ratio are similar. A configurational lift coefficient of 0.073 can be used to extrapolate the force generation of different size aircraft. Let the cross sectional area be 5 m^2 and the jet velocity 100 $m.s^{-1}$. Using the lift coefficient equation, we can determine the lift generated in such a case to be 2200N. Using the same aspect ratio we can determine that $x_0 = 1.26$m and $x_m = 2.5$m. Using the density of aluminium and a thickness of 2cm we can determine the weight of the disk to be 54kg. In reality, the disk will be hollow and formed of a skin of 2mm, and rib for structural integrity. Keeping to the same scaling, the nozzle height is calculated to be $h = 10$cm. The mass flow rate required from the engine is estimated to be $\dot{m} = 80kg.s^{-1}$. Therefore, with no easy way of determining the engine weight, one of the lightest turboprop (Arrius 2F) can be taken as an example with a mass of 103kg. The remaining capacity (60kg) can be used between payload and fuel. This study shows that a larger scale aircraft may be possible if the flow behave similarly to the small scale experiments conduct.

Such a craft can be used the industrial sector as a cheap and small alternative to helicopters. It may be used as a type crane to precisely ferry small packages to remote areas. In a practical application like this, optimisation should be made to increase efficiency. One such optimization would be further deflecting the flow to ensure a purely vertical disk exit flow. Furthermore, the engine weight may be considerably reduced if designed specifically to this aircraft's specification.

Chapter 6

Conclusion

An analytical framework was developed to study the system. The rotation parameter B is used to determine in what proportions the jet and spin influence the system. The lift coefficient c_L is defined to non dimensionalize the lift generated in the system. Furthermore, the a force vector analysis is performed to produce a possible control system.

A CFD model is generated and validated against known solutions. It is then used to explore the underlying the system's aerodynamic mechanisms. The boundary layer profiles determined that the velocity profile for a given configuration is closely related to the compound of the jet and spin components.

Secondly, the computational analysis also generated pressure distribution curves for the traditional and novel design. This is used to compare both designs. In the traditional design, an increased angular velocity generates a very large pressure difference at the disk's edge. This is due to equatorial eruption, and causes separation and outwards ejection of the flow. This phenomenon reduces the efficiency of the traditional geometry. The pressure model of the new design shows similarities with the traditional one. The outer half of the novel design behaves similarly to the inner half of the traditional. Furthermore, it was observed that the efficiency of the inner disk in the novel design is reduced with angular velocity.

The CFD model further was used to estimate the lift generated by the system under different configurations. These results agree with experimentally produced data. Lift generated by this system follows a parabolic curve with respect to the mass flow rate of the jet and in term of the flows tangential velocity to the surface. Similarly, the disk's torque is proportional to the square of the surface's angular velocity. Converting the lift to the lift coefficient shows that at higher mass flow rates it tends towards a specific value. This is called the configurational lift coefficient c_l'. This is assumed to be constant for a given configuration.

The flap mechanism was tested both experimentally and computationally. The configurations used differed. In the computational investigation, only one control

surface is actuated and the flap's span Δ is 90^o. In the experimental setup, all flaps are actuated at once and their individual span Δ is 40^o. Using a conversion shown in the methods chapter the results of both investigations can be compared. Both sets of data show the system behaves predictably.

Over the entirety of experimental data, non-linear variations of lift coefficient were observed. Further investigation shows that multiple flow regimes were present in the configurations studied. These flow regimes are further observed within a frequency analysis of datasets. At open control setting ($\beta = -5^o$), and unsteady regimes is observed with a characteristic dominant frequencies of 11 hz and 24 hz. In an non spinning system and $\beta = 5$, resonance was observed. It is characterized by three to four equally spaced peaks between 420Hz and 580Hz. This may be due to a resonance response of the jet's wake by a stationary disk. A steady state regime can be observed between β 13^o & 25^o in a non stationary system. In a spinning one however the steady state seems to be extended to $\beta = 5^o$. This flow regime is characterised by a prominent peak at 81 Hz. Finally, separation occurs when $\beta > 26^o$. In this state, the peak at 81Hz loses amplitude and 11Hz becomes prominent again.

The results present a strong case for the proposed design's feasibility. Enough lift can be produced by the system to enable flight. Furthermore, the pitch and roll controls are shown to be responsive. Rotation of the disk enables yaw control to a higher degree than other Coanda craft studied. Other stability benefits are postulated due to the novel design's elevated aerodynamic centre. Furthermore, the added complexity of a second rotating component can be offset by adding a performance enhancing mechanism. This would increase the lift generated by utilising radial momentum induced by the disk.

Further work

Varying some of the **geometric parameters** such as the aspect ratio is necessary to determine a generalised lift equation. The surface geometry can also be aerodynamically optimised for the desired output. However, many assumptions made would no longer be valid if the shape changes too much. Furthermore, testing control surfaces with varying span can be used to validate some of the equations developed in chapter 3.

PIV should be used to determine the nature of flow in the different regimes discussed in the report. It can be used to determine when and if separation occurs. Furthermore, it can determine the formation and size of eddies as well as boundary layer profiles that can be cross referenced with the computational data.

The **control response** needs to be tested at finer increments in what is thought to be the stable flow regime. Further investigation is also required into the resonance

exhibited in one of the configurations. If it can be reliably reproduced, it can increase efficiency.

Performance enhancing mechanisms discussed previously should be tested. These should show the disk rotation has a much greater effect on the lift produced, as well as a general boost in performance.

Testing the craft in of a **wind tunnel** in a forward flight configuration is crucial to determining two different aspects of the system. Firstly, whether the flight asymmetry due to the rotating surface affects flight by causing a moment imbalance. Secondly, where is the drag vector located for different pitch angles.

The **gyroscopic effects** must be tested. The craft's controls would be vastly different if precession came into effect. This testing can be expanded to determine whether gyroscopic effects can be manipulated to favour stability or manoeuvrability. And whether it can easily change from one to the other.

Finally, the **dynamic stability** of the craft must be tested. Such tests involve building a flight-capable prototype and comparing the actual performance to the postulated behaviour.

Bibliography

[1] Naudin J. L. The GFS UAV project, a Coanda effect flying saucer tested. http://jlnlabs.online.fr/gfsuav/index.htm, 2006.

[2] Florin NEDELCU. Coanda effect UAV a new born baby in the unmanned aerial vehicles family. *Review of the Air Force Academy*, 2(17):21–28, 2010.

[3] H. Coanda. Propelling device, 1936. US Patent # 2,108.652.

[4] H. Coanda. Procédé de propulsion dans un fluide. *Brevet dinvention France*, 2, 1932.

[5] Uwe H. von Glahn. Technical Note 4377: Use of the Coanda effect for jet deflection and vertical lift with multiple-flat-plate and curved-plate deflection surfaces. *National advisory committee for aeronautics (NACA)*, 1951.

[6] J. W. Claude and M. F. J. Carver. Fluid sustained aircraft, 1962.

[7] Avro Aircraft Limited. Project 1794 final development summary report. Technical report, 06 1956. Also available https://research.archives.gov/id/6920770.

[8] Avro Aircraft Limited. Program planning report project 1794 extension program. Technical report, 04 1957. Also available https://research.archives.gov/id/6981836.

[9] Ralph D. Lorenz. Spinning aircraft and nonspinning disc aircraft. *Spinning Flight: Dynamics of Frisbees, Boomerangs, Samaras, and Skipping Stones*, pages 217–238, 2006.

[10] B Lindebaum and William Blake. The vz-9 avrocar. *Available online at https://web. archive. org/web/20060927042257/http://www. vtol. org/pdf/Vertiite-VZ9. pdf*, 1998.

[11] Peter Spittle. Gas turbine technology. *Physics education*, 2003.

[12] Zuk B. *Avrocar: Canada's Flying Saucer: The Story of Avro Canada's Secret, Projects*. Boston Mills Press, June 2001.

[13] D. E. Thomas and M. F. J. Carver. Disc-type aircraft with peripheral jet control, February 27 1962. US Patent 3,022,963.

[14] N. C. Price. High velocity high altitude VTOL aircraft, September 10 1963. US Patent 3,103,324.

[15] H. Coanda. Jet sustained aircraft, June 13 1961. US Patent 2,988,303.

[16] B. Gunston. *The Osprey Encyclopaedia of Russian Aircraft*. Osprey Publishing.

[17] *The YC-14 STOL Prototype: Its Design, Development, and Flight Test*.

[18] S. F. Yaros, M. G. Sexstone, L. D. Huebner, and J.E. Lamar. Synergistic Airframe-Propulsion Interactions and Integrations. *National Aeronautics and Space Administration*, (March), 1998.

[19] Takafumi Nichino, Seonghyeon Hahn, and Karim Shariff. LES of high-reynolds-number Coanda flow separating from a rounded trailing edge of a circulation control airfoil. 2010.

[20] M Mamou and M. Khalid. Steady and unsteady flow simulation of a combined jet flap and Coanda jet effects on a 2d airfoil aerodynamic performance. *Revue des Energies Renouvelables CER*, 7:55–60, 2007.

[21] Valeriu Dragan. Numerical investigations of Coanda lift on a double curvature super circulated ramp. *International Journal of Civil and Structural Engineering*, 2(1):241, 2011.

[22] Burhan Saeed. Exploring the aerodynamic annular-wing for V / STOL aircraft, 2010.

[23] A. Nemati and M. Kumar. Modeling and control of a single axis tilting quadcopter. In *American Control Conference (ACC), 2014*, pages 3077–3082, June 2014.

[24] Jonathan R. Potts and William J. Crowther. Flight control of a spin stabilised axi-symmetric disc-wing. *American Institute of Aeronautics and Astronautics*, 2001.

[25] H. Djojodihardjo, R. I. Ahmed, and A. Yousefian. An analysis on the lift generation for Coand micro air vehicles. *IEEE International Conference on Aerospace Electronics and Remote Sensing Technology*, pages 164–169, Nov 2014.

[26] R. I. Ahmed, A. R. Abu Talib, A. S. Mohd Rafie, and H. Djojodihardjo. Aerodynamics and flight mechanics of MAV based on Coand effect. *Aerospace Science and Technology*, 62:136 – 147, 2017.

[27] A.R. Abu-Talib A.S. Mohd-Rafie Harijono Djojodihardjo, Riyadh I. Ahmed. Analyical and CFD visualization studies of COAND mav.

[28] H. Lee, S. Han, H. Lee, J. Jeon, C. Lee, Y. B. Kim, S. H. Song, and H. R. Choi. Design optimization, modeling, and control of unmanned aerial vehicle lifted by Coand effect. *IEEE/ASME Transactions on Mechatronics*, 22(3):1327–1336, June 2017.

[29] A. Dumitrache, F. Frunzulica, and T. C. Ionescu. Mathematical Modelling and Numerical Investigations on the Coanda Effect. *Nonlinearity, Bifurcation and Chaos — Theory and Applications*, pages 101–132, 2012.

[30] Edward R. Benton. On the flow due to a rotating disk. *Journal of Fluid Mechanics*, 24(4):781, 2006.

[31] W. G. Cochran. The flow due to a rotating disc. In *Mathematical Proceedings of the Cambridge Philosophical Society*, volume 30, pages 365–375. Cambridge Univ Press, 1934.

[32] M. H. Lee, D. R. Jeng, and K. J. de Witt. *Journal of Heat Transfer*, (4):496–502.

[33] B. T. Chao and R. O. Fagbenle. On Merk's method of calculating boundary layer transfer. *International Journal of Heat and Mass Transfer*, 17(2):223–240, 1974.

[34] Aesir unmanned autonomous system. `http://www.aesir-uas.co.uk/`, accessed on 02/2016.

[35] W. H. H. Banks. The boundary layer on a rotating sphere. *The Quarterly Journal of Mechanics and Applied Mathematics*, 18(4):443–454, 1965.

[36] D. J. Cleaver; Z. Wang; I. Gursul; M. R. Visbal. Lift enhancement by means of small-amplitude airfoil oscillations at low Reynolds numbers. *AIAA Journal*, 9:2018–2033, 2011.

Appendix 1 - PC MATLAB code

```
1
2  %make sure nothing is open
3  clear
4  close all
5
6  %close instruments in case
7  if instrfind ≠ 0
8  fclose(instrfind);
9  delete(instrfind);
10 end
11
12 % create figure &initialise
13 fig = figure('units','normalized','outerposition',[0 0.05 1 0.9]);
14 jetval = [];
15 figInit
16
17 %% INPUT PARAMETERS AND INITIALISATION
18 %data initialising
19 global data;
20
21 %booleans
22 Q  = false;          %quit
23 CR = false;          %connected arduino
24 CS = false;          %connected sensor
25 SP = false;          %spinning
26 JSP = false;         %spinning (jet)
27 EXP = false;         %is the experiment running
28 HDG = false;         %is this heading mode
29 Auto = false;        %is it doing autoTesting
30 AutoZ = false;       %should reZero
31 AutoF = false;       %did it just finish autoTesting
32
33 %initialisation of variables
34 data.hz = 0;                                    %velocity array
35 data.Uj = 0;                                    %jet velocity
36 data.tz = 0;                                    %time hz array
37 data.ts = 0;                                    %time sensor array
38 data.F = [0;0;0];                               %sensor force data
39 data.T = [0;0;0];                               %sensor toque data
40 data.expd = [];                                 %memory of past exp
41 CTRLmo = [0,0,0];                               %ctrl moments to ...
       compare (X, Y, and heading)
42 buffs = 0;                                      %buffer for sensor
43 hz_des = {'30'};                                %desired velocity
44 ang_des = {'0'};                                %desired ctrl angle
```

```
45 hdg_des = {'0'};                                    %desired heading
46 filename = {'filename'};                            %filename
47 expts = {'1'};                                      %experimental time string
48 expt = 1;                                           %experimental time
49 Nexp = 0;                                           %number of experiments
50 C = 0;                                              %counter
51 jetLoad = 0;                                        %jet load in %
52 tmpplot = [];                                       %initialisation for ...
       the temp plot used for boundaries
53 TstDlgIn = {'0','0','5'};                           %Inputs for the auto ...
       testing system
54 AutoN = 0;                                          %number of AutoTests left
55
56
57 %legend of the data layout
58 data.exdleg = {'Sensor data', 'Hz', 'Load of the jet',...
59 'Measured jet velocity', 'CTRL angles', 'Desired Heading',...
60 'Actual heading'};
61
62
63 %zeroing values
64 Fz = [0;0;0];
65 Tz = [0;0;0];
66 t1 = [0;0;0];
67 t2 = [0;0;0];
68
69 %stuff required to set up the serial
70 BaudRate = 115200;                                  %BDrate (bits/s)
71
72 %stuff required for udp
73 LocalPort = 19000;
74 InputBufferSize = 15000;
75
76 %% INITIALISING FIGURE FUNCTION
77 function figInit
78
79 % set units to pixels and get the position matrix
80 set(fig,'units','pixels')
81 fig_pos = get(fig,'pos');
82
83 % get width and height in pixels
84 fig_w = fig_pos(3)-fig_pos(1);
85 fig_h = fig_pos(4)-fig_pos(2);
86
87 %defining the box position engulfing all text and push buttons
88 tboxp = 0.2; %ratio in x
89 tboxr = 0.3; %ratio in y
90 tbox = [(1-tboxp)*fig_w,(0.5-tboxr/2)*fig_h,fig_w,(0.5+tboxr/2)*fig_h];
91
```

```
92  %defining the box for the axis
93  xboxm = 0.05; %outermargin
94  %[left, bottom, right, top]
95  xboxt = ...
        [xboxm*fig_w,xboxm*fig_h,(1-tboxp-2*xboxm)*fig_w,(0.33-xboxm)*fig_h];
96  %[left, bottom, width, height]
97  xbox{1} = ...
        [xboxt(1)/fig_w,xboxt(2)/fig_h,(xboxt(3)-xboxt(1))/fig_w,(xboxt(4)-xboxt(2))/fig_h
98  xbox{2} = [xbox{1}(1),xbox{1}(2)+0.33,xbox{1}(3),xbox{1}(4)];
99  xbox{3} = [xbox{1}(1),xbox{1}(2)+0.67,xbox{1}(3),xbox{1}(4)];
100
101 %defining the box for the model
102 modbox{1} = [0.725,0.05,0.1,0.2];
103 modbox{2} = [0.875,0.05,0.1,0.2];
104
105 %defining the box for the heading plot and legend pos
106 hdgbox = [0.8,0.675,0.1,0.2];
107 hdgboxl = [0.730,0.825,0.04,0.02];
108
109 %temp stuff for the model
110 color = 'rgbk';
111 tmp = [0,1;0,0;0,0;0,0;0,1;0,0;0,0;0,0;0,1;0,1;0,1;0,1];
112 tmptitle = {'Force ','Torque '};
113 tmpaxnames = {'Xdata','Ydata','Zdata'};
114 tmpaxlmnames = {'XLim','YLim','ZLim'};
115
116
117 %text box variables
118 ntxtR = 16;                                     %number of text rows
119 ntxtC = 2;                                      %number of text cols
120
121 %getting all pos
122 [postxt,ntxt] = get_pos(ntxtR,ntxtC,tbox);
123
124 %names in boxes
125 textnames = {   'Arduino',                                  'Sensor';...
126 'not Connected',                        'not Connected';...
127 'Connect to Arduino',                   'Connect to Sensor';...
128 'Toggle Experiment',                    'Save Data';...
129 'Toggle Motor',                         'Set Velocity';...
130 'Flush objects',                        'Zero Sensor';...
131 'Set CTRL Angle',                       'Calibrate Pressure';...
132 'Set CTRL heading',                     'Zero Moments while ...
        spining';...
133 '',                                     '';...
134 'N/A',                                  'Current heading (degrees)';...
135 '0',                                    'Current deflection ...
        (degrees)';...
136 '0',                                    'Current Force(N)';...
```

```
'0',                                        'Current Torque(Nm)';...
'0',                                        'Current Velocity (Hz)';...
'0',                                        'Current jet velocity ...
    (m.s-1)';...
'not Running',                              'Experiment'};


%stylles of obejcts
textstyles = {  'text',              'text';...
'text',              'text';...
'pushbutton',        'pushbutton';...
'pushbutton',        'pushbutton';...
'pushbutton',        'pushbutton';...
'pushbutton',        'pushbutton';...
'pushbutton',        'pushbutton';...
'pushbutton',        'pushbutton';...
'text',              'text';...
'text',              'text';...
'text',              'text';...
'text',              'text';...
'text',              'text';...
'text',              'text';...
'text',              'text';...
'text',              'text'};

%plot titles
ptitle = {'Force Measurment', 'Torque Measurement', 'Velocity ...
    Measurement'};

%putting all the UIcontrol objects (text and buttons)
for i = 1:ntxtR
for j = 1:ntxtC
t(i,j) = ...
    uicontrol('Style',textstyles{i,j},'String',textnames{i,j},'pos',postxt{i,j});
end
end

%drawing the three plots
for i = 1:3
s(i) = subplot(3,3,i);
for j = 1:3
a(i,j) = plot(0,0);
ax(i,j) = gca;
hold on
end
hold off
grid on
grid minor
title(ptitle{i});
```

```
183 set(s(i),'pos',xbox{i});
184 end
185
186 %drawing the heading comparisson box
187 s(6) = subplot(10,10,100);
188 polar(0,0)
189 hold on
190 for i = 1:2
191 hdgax(i) = plot([0,1],[0,0]);
192 end
193 hold off
194 title('Heading comparison (0->comp)')
195 legend([hdgax(1),hdgax(2)],{'desired','actual'},'Position',hdgboxl);
196 set(s(6),'pos',hdgbox)
197
198 %drawing the box for the model
199 for j = 1:2
200 s(3+j) = subplot(10,10,100);
201 for i =1:4
202 m(j,i) = ...
       plot3(tmp((i-1)*3+1,:),tmp((i-1)*3+2,:),tmp((i-1)*3+3,:),color(i));
203 axis equal
204 grid on
205 xlim([-0.1,1.1])
206 ylim([-0.1,1.1])
207 zlim([0,1.1])
208 axm(j,i) = gca;
209 hold on
210 end
211 hold off
212 title([tmptitle{j} 'Model x-R y-G z-B t-BK']);
213 set(s(3+j),'pos',modbox{j});
214 end
215
216 %attaching the callback functions
217 set(t(3,1),'Callback',@connectR);
218 set(t(3,2),'Callback',@connectS);
219 set(t(4,1),'Callback',@togX);
220 set(t(4,2),'Callback',@savdat);
221 set(t(5,1),'Callback',@mottog);
222 set(t(5,2),'Callback',@setvel);
223 set(t(6,1),'Callback',@flushnow);
224 set(t(6,2),'Callback',@zero);
225 set(t(7,1),'Callback',@setang);
226 set(t(7,2),'Callback',@calpre);
227 set(t(8,1),'Callback',@sethdg);
228 set(t(8,2),'Callback',@zeroSP);
229
230 %adding the quit button
```

```
231 tquit = ...
       uicontrol('Style','pushbutton','String','Quit','Callback',@quit,'pos',[(1-tboxp*1.
232
233 %adding the jet control
234 jetbut = uicontrol('Style','pushbutton','String','Toggle ...
       Jet','Callback',@jettog,'pos',[(1-tboxp*1.25)*fig_w,0.30*fig_h,tboxp*fig_w*0.25,0.
235 jetsli = ...
       uicontrol('Style','slider','Min',0,'Max',100,'Value',10,'Callback',@setjet,'pos',[
236 jetval = ...
       uicontrol('Style','text','String','10','pos',[(1-tboxp)*fig_w+tboxp*fig_w*0.75,0.3
237 autoTest = ...
       uicontrol('Style','pushbutton','String','Auto','Callback',@RunTest1,'pos',[(1-tbox
238 end
239
240 %% getting the positions function
241 % function [vec{i,j}, n total] = get_pos(nb of rows, nb of cols, ...
       box[left,bottom,right,top])
242 % i is column index
243 % j is row index
244 function [vec, n] = get_pos(nrows, ncols, box)
245 %division vector
246 tw = [0:1/ncols:(ncols-1)/ncols];
247 th = [(nrows-1)/nrows:-1/nrows:0];
248 w = box(3)-box(1);
249 h = box(4)-box(2);
250 %total number
251 n = nrows*ncols;
252
253 for i =1:ncols
254 for j =1:nrows
255 %getting the parameters for the vec
256 nw      = w/ncols;
257 nh      = h/nrows;
258 left    = (1-w)/(2*ncols)+box(1)+tw(i)*w;
259 bottom  = (1-h)/(2*nrows)+box(2)+th(j)*h;
260
261 %adding new param
262 vec{j,i} = [left,bottom ,nw,nh];
263 end
264 end
265 end
266
267 %% functions
268 %setting up the serial
269 function connectR(source,event)
270
271 t(2,1).String = 'Connecting';
272 pause(0.01);
273 %getting the available com ports
```

```
avCOMS = instrhwinfo('serial');
%popup to select a port
[i,¬] = listdlg('Name','Select a port','PromptString',...
'Available ...
   options:','SelectionMode','single','ListString',avCOMS.AvailableSerialPorts);
COMS = avCOMS.AvailableSerialPorts{i};
%initiating connection
S = serial(COMS,'baudrate',BaudRate);           %Creating object
if(Serial_connection(S))                        %if connected
t(2,1).String = 'Ready';                    %show on gui
CR = true;                                  %update bool
else                                            %ditto for else
t(2,1).String = 'not Connected';
CR = false;
end
pause(0.0001);
tic
end

%setting up the udp
function connectS(source,event)

t(2,2).String = 'Connecting';
pause(0.0001);

%creating object
U = udp('','LocalPort',LocalPort,'InputBufferSize',InputBufferSize);
fopen(U);
pause(2);
if U.BytesAvailable>0                           %if connected
t(2,2).String = 'Ready';                    %show on gui
CS = true;                                  %update bool
else                                            %ditto for else
t(2,2).String = 'not Connected';
CS = false;
fclose(U);
end
pause(0.0001);
expts = inputdlg('Experimental time','prompt',1,expts);
expt = str2double(expts{:});
end

%toggling the motor
function mottog(source,event)
if CR
flushoutput(S);
if ¬SP
fprintf(S,'startm');
elseif SP
```

```
322 fprintf(S,'stpmot');
323 end
324 SP = ¬SP;
325 end
326 end
327
328 %setting the velocity
329 function setvel(source,event)
330 hz_des = inputdlg('new Velocity','prompt',1,hz_des);
331 if CR
332 flushoutput(S);
333 fprintf(S,'%s','setvel');
334 fwrite(S,str2num(hz_des{1}),'uint16');
335 end
336 end
337
338 %toggling the jet
339 function jettog(source,event)
340 if CR
341 flushoutput(S);
342 if ¬JSP
343 fprintf(S,'startj');
344 elseif JSP
345 fprintf(S,'stpjet');
346 end
347 JSP = ¬JSP;
348 end
349 end
350
351 %setting the jet velocity
352 function setjet(source,event)
353 jetLoad = source.Value;
354 set(jetval,'String',num2str(jetLoad));
355 if CR
356 flushoutput(S);
357 fprintf(S,'%s','setjet');
358 fwrite(S,source.Value,'uint16');
359 end
360 end
361
362 %calibrating the pressure sensor
363 function calpre(source,event)
364 if CR
365 flushoutput(S);
366 fprintf(S,'%s','calpre');
367 end
368 end
369
370 %setting the angle
```

```
371 function setang(source,event)
372 ang_des = inputdlg('new Angle (between 0 and 35)','prompt',1,ang_des);
373 ang_des = {num2str(max(str2num(ang_des{1}),0))};                    ...
       %constraining value to a minimum of 30
374 ang_des = {num2str(min(str2num(ang_des{1}),35))};                   ...
       %constraining value to a maximum of 80
375 t(size(t,1)-5,1).String = num2str(str2num(ang_des{1}));             ...
       %updating text box of angle
376 t(size(t,1)-6,1).String = 'N/A';                                    ...
       %updating text box of heading
377 if CR
378 flushoutput(S);
379 fprintf(S,'%s','setang');
380 fwrite(S,str2num(ang_des{1}),'uint16');
381 HDG = false;
382 end
383 end
384
385 %setting the heading
386 function sethdg(source,event)
387 hdg_des = inputdlg('new Angle (between 0 and 360)','prompt',1,hdg_des);
388 hdg_des = {num2str(max(str2num(hdg_des{1}),0))};                    ...
       %constraining value to a minimum of 0
389 hdg_des = {num2str(min(str2num(hdg_des{1}),360))};                  ...
       %constraining value to a maximum of 360
390 t(size(t,1)-5,1).String = 'N/A';                                    ...
       %updating text box of angle
391 t(size(t,1)-6,1).String = num2str(str2num(hdg_des{1}));             ...
       %updating text box of heading
392 %updating the heading plot
393 set(hdgax(1),'Xdata',[0;cos(str2num(hdg_des{1})*pi/180)],'Ydata',[0;sin(str2num(hdg_de
394 if CR
395 flushoutput(S);
396 fprintf(S,'%s','sethdg');
397 fwrite(S,str2num(hdg_des{1}),'uint16');
398 HDG = true;
399 end
400 end
401
402 %saving the data
403 function savdat(source,event)
404 filename = inputdlg('new Filename','prompt',1,filename);
405 save(['data/' filename{1}],'data');
406 end
407
408 %saving the data
409 function togX(source,event)
410 data.ts = 0;
411 t1 = [0;0;0];
```

```
412 t2 = [0;0;0];
413 data.F = [0;0;0];
414 data.T = [0;0;0];
415 EXP = ¬EXP;
416 if EXP
417 t(end,1).String = 'Running';
418 else
419 t(end,1).String = 'not Running';
420 end
421 end
422
423 %flushing and closing all the ports
424 function flushnow(source,event)
425 if instrfind ≠ 0
426 fclose(instrfind);
427 delete(instrfind);
428 end
429 CR = false;
430 CS = false;
431 t(2,1).String = 'not Connected';
432 t(2,2).String = 'not Connected';
433 end
434
435 %zeroing function
436 function zero(source,event)
437 Fz = median(t1(:,4:end),2);
438 Tz = median(t2(:,4:end),2);
439 end
440
441 %zeroing function while spinning for the moemnts
442 function zeroSP(source,event)
443 %          findMO;
444 Tz = mean(t2(:,ind(1):ind(2)),2);
445 end
446
447 %quitting function
448 function quit(source,event)
449
450 %making quit boolean true
451 Q = true;
452
453 %if spinning toggle motor
454 if SP
455 mottog;
456 end
457
458 %if connect to anything break and delete instruments
459 if CS || CR
460 fclose(instrfind);
```

```
delete(instrfind);
end

%close figure
close(fig);
end

%msg conversion
function msgC(msg)

x =  [(msg(2) + msg(3)*256) - 2^15, (msg(4) + msg(5)*256) - 2^15, ...
    (msg(6) + msg(7)*256)- 2^15];

if msg(1) == 1018
t1(:,end+1) = x(1:3)/10;
t2(:,end+1) = t2(:,end);
elseif msg(1) == 1019
t2(:,end+1) = x(1:3)/1000;
t1(:,end+1) = t1(:,end);
end

end

%Updating text function
function textUp
%replace the strings for current hz, Uj, T & F
t(size(t,1)-4,1).String = num2str(mean(data.F,2)');
t(size(t,1)-3,1).String = num2str(mean(data.T,2)');
t(size(t,1)-2,1).String = ...
    num2str(mean(data.hz(max(1,length(data.hz)-10):end)));
t(size(t,1)-1,1).String = ...
    num2str(mean(data.Uj(max(1,length(data.Uj)-30):end)));
end

%finding the ctrl moments function from the sinwave
function findMO
%get position and location of peaks
[peaks,locations] = findpeaks(data.T(1,:));
%find the index of the median peak in the first half of the data
tmp1 = locations(peaks(1:5)==max(peaks(1:5)));
%find the index of the second to last peak
tmp2 = ...
    locations(length(peaks)-5+find(peaks(end-4:end)==max(peaks(end-4:end))));
%get the index values
ind = [tmp1(1), tmp2(1)];
%getting the X moment and converting to heading
CTRLmo(1) = mean(data.T(1,ind(1):ind(2)));
%getting the Y moment and converting to heading
CTRLmo(2) = mean(data.T(2,ind(1):ind(2)));
```

```
506 %getting the actual heading
507 CTRLmo(3) = 180*atan2(-CTRLmo(1),-CTRLmo(2))/pi;
508 end
509
510
511 %% Auto-running tests functions
512 %function one to set up the Zeroing
513 function RunTest1(source,event)
514
515 TstDlg = inputdlg({'Enter Jet Duty', 'Enter Disk Velocity', 'Enter ...
       Number of Runs'},'Test Inputs',[1 1 1], TstDlgIn);
516 TstDlgIn = TstDlg;
517 Auto = true;
518 AutoZ = true;
519 AutoN = str2double(TstDlg{3});
520
521 %Setting up jet flow
522 set(jetval,'String',TstDlg{1});
523 if CR
524 flushoutput(S);
525 fprintf(S,'%s','setjet');
526 fwrite(S,str2double(TstDlg{1}),'uint16');
527 end
528 jetLoad = str2double(TstDlg{1});
529
530 %Setting up disk roation
531 if CR
532 flushoutput(S);
533 fprintf(S,'%s','setvel');
534 fwrite(S,str2double(TstDlg{2}),'uint16');
535 end
536
537 %Toggling Experiment for Zeroing
538 togX();
539
540
541 end
542
543 %secondary run test function
544 function RunTest2
545 %if first actual test
546 if str2double(TstDlgIn{3}) == AutoN
547
548 if str2double(TstDlgIn{1}) ≠ 0
549 jettog();
550 end
551
552 if str2double(TstDlgIn{2}) ≠ 0
553 mottog();
```

```
554 end
555
556 %Waiting for the user input to show that everything is up to speed
557 messagebox = msgbox('Click any key when ready');
558 waitforbuttonpress;
559 delete(messagebox);
560
561 end
562
563 %decrement the counter
564 AutoN = AutoN-1;
565
566 %check if last run and if so change bool
567 if AutoN == 0
568 Auto = false;
569 AutoF = true;
570 end
571
572 %run experiment
573 togX()
574
575 end
576
577
578 %% MAIN LOOP
579 while ¬Q
580 %if connected to arduino
581 if CR
582 %if bytes available get hz and timestamp
583 while S.BytesAvailable ≥ 1
584 temp1 = int32(fread(S,1,'uint32'));
585 temp2 = typecast(temp1,'uint16');
586 data.hz = [data.hz;double(temp2(1)/100) ];
587 data.Uj = [data.Uj;double(temp2(2)/100) ];
588 data.tz = [data.tz; toc];
589 end
590 if mod(C,100) ==0
591 set(a(3,1),'Xdata',data.tz(max(1,length(data.tz)-1000):end),'Ydata',data.hz(max(1,leng
592 set(a(3,2),'Xdata',data.tz(max(1,length(data.tz)-1000):end),'Ydata',data.Uj(max(1,leng
593 set(ax(3,1),'Xlim',[data.tz(max(1,length(data.tz)-1000)) ...
       data.tz(end)]);
594 end
595 end
596
597 %if experiment is running
598 if EXP
599
600 %if connected to sensor
601 if CS
```

```
602 if strcmp(U.Status,'closed')
603 fopen(U);
604 end
605 t(2,2).String = 'Measuring';
606 loading = waitbar(0,'Please wait','Name','Running Experiment');
607 t1 = [0;0;0];
608 t2 = [0;0;0];
609 pause(0.00000001);
610 %if bytes availabe then read
611 while length(data.ts)<expt*1000
612 if U.BytesAvailable ≥56
613 temp = uint8(fread(U,1,'uint8'));
614 temp = typecast(temp,'double');
615
616 %if message recieved the right size then translate and
617 %store force and torque with timestamp
618 if length(temp) ≥7
619 msgC(temp);
620 data.ts     = [data.ts,toc];
621 buffs       = [buffs,U.BytesAvailable];
622 end
623 end
624 if mod(length(data.ts),expt*100)==0
625 waitbar(length(data.ts)/(expt*1000))
626 end
627 end
628 close (loading)
629 data.F = t1(:,3:end)-Fz*ones(1,length(t1)-2);
630 data.T = t2(:,3:end)-Tz*ones(1,length(t2)-2);
631
632 % if enough data points then plot last 100 points of sensor
633 if length(data.ts)>2
634 for i = 1:3
635 set(a(1,i),'Xdata',data.ts(3:end),'Ydata',data.F(i,:)');
636 set(a(2,i),'Xdata',data.ts(3:end),'Ydata',data.T(i,:)');
637 end
638 for i =1:3
639 set(m(1,i),tmpaxnames{i},[0;mean(data.F(i,:))])
640 set(axm(1,i),tmpaxlmnames{i},[min([0;mean(data.F(i,:))])-0.1,max([0;mean(data.F(i,:))
641 set(m(2,i),tmpaxnames{i},[0;mean(data.T(i,:))])
642 set(axm(2,i),tmpaxlmnames{i},[min([0;mean(data.T(i,:))])-0.001,max([0;mean(data.T(i,:
643 end
644 %setting the model plots
645 set(m(1,4),'Xdata',[0;mean(data.F(1,:))],'Ydata',[0;mean(data.F(2,:))],'Zdata',[0;mean
646 set(m(2,4),'Xdata',[0;mean(data.T(1,:))],'Ydata',[0;mean(data.T(2,:))],'Zdata',[0;mean
647 %setting the heading graph
648 if SP
649 findMO;
650 subplot(s(2))
```

```
651 delete(tmpplot)
652 hold on
653 tmpplot(1) = ...
       plot([data.ts(ind(1)),data.ts(ind(1))],[min(min(data.T)),max(max(data.T))]);
654 tmpplot(2) = ...
       plot([data.ts(ind(2)),data.ts(ind(2))],[min(min(data.T)),max(max(data.T))]);
655 hold off
656 else
657 tmpplot = [];
658 CTRLmo(1) = mean(data.T(1,:));
659 CTRLmo(2) = mean(data.T(2,:));
660 CTRLmo(3) = 180*atan2(-CTRLmo(1),-CTRLmo(2))/pi;
661 end
662 set(hdgax(2),'Xdata',[0;cos(deg2rad(CTRLmo(3)))],'Ydata',[0;sin(deg2rad(CTRLmo(3)))])
663
664 end
665 if length(data.ts)==expt*1000
666 fclose(U);
667 EXP = false;
668 t(end,1).String = 'not Running';
669 t(2,2).String = 'Ready';
670 Nexp = Nexp+1;
671 data.expd{1,Nexp} = [data.ts(3:end);data.F;data.T];
672 data.expd{2,Nexp} = data.hz(end);
673 data.expd{3,Nexp} = jetLoad;
674 data.expd{4,Nexp} = mean(data.Uj(max(1,length(data.Uj)-4):end));
675 if ¬HDG
676 data.expd{5,Nexp} = str2num(ang_des{1});
677 data.expd{6,Nexp} = 'N/A';
678 data.expd{7,Nexp} = 'N/A';
679 else
680 data.expd{5,Nexp} = 'N/A';
681 data.expd{6,Nexp} = str2num(hdg_des{1});
682 data.expd{7,Nexp} = mod(CTRLmo(3)+360,360);
683 end
684 textUp;
685 end
686 end
687
688 % rerunning zeroing test if out of tolerance
689 if AutoZ && ¬EXP
690 zero;
691 if mean(mean(abs(t1(:,3:end)-Fz*ones(1,length(t1)-2))))<0.04
692 AutoZ = false;
693 else
694 togX;
695 end
696 end
697
```

```
698
699 % running other autotest if needed
700 if Auto && ¬EXP && ¬AutoZ
701 RunTest2;
702 end
703
704 % toggling whats just been used if an autotest was just used
705 if AutoF && ¬EXP
706 if str2double(TstDlgIn{1}) ≠ 0
707 jettog();
708 end
709
710 if str2double(TstDlgIn{2}) ≠ 0
711 mottog();
712 end
713 AutoF = false;
714 end
715
716 end
717 if mod(C,100)==0
718 textUp;
719 drawnow;
720 end
721 C = C+1;
722 end
```

Appendix 2 - Arduino code

```
1
2 #include <DueTimer.h>
3 #include <Servo.h>
4 #define pi 3.14159265359
5
6 //Char values for commands + command buffer
7 char command [] = "000000";   //buffer variable for command
8 char motstr [] = "startm";    //starting motor
9 char jetstr [] = "startj";    //starting jet
10 char setvel [] = "setvel";   //setting the motor vel
11 char setjet [] = "setjet";   //setting the jet vel
12 char stpmot [] = "stpmot";   //stoping motor
13 char stpjet [] = "stpjet";   //stoping jet
14 char setang [] = "setang";   //setting the desired angle
15 char calpre [] = "calpre";   //calibrating the pressure
16 char sethdg [] = "sethdg";   //setting the heading
17
18 //Booleans
19 bool temp = false;            // bool temp
20 bool startM = false;          // bool motor running
21 bool motIni = false;          // bool is motor initialised
22 bool startJ = false;          // bool jet running
23 bool jetIni = false;          // bool is jet initialised
24
25 //Pin assignments (check schematic file in documents)
26 int motpin = 25;              //motor pin
27 int jetpin = 27;              //jet pin
28 int rpspin = 31;              //encoder pin
29 int escpinm = 23;             //motor power detection pin
30 int escpinj = 29;             //jet power detection pin
31 int prepin = A1;              //pressure sensor pin
32 int c1pin = 45;               //servo 1 pin
33 int c2pin = 47;               //servo 2 pin
34 int c3pin = 49;               //servo 3 pin
35 int tmppin = 40;              //LEDPIN FOR STATUS
36
37 //RPS variables
```

```
38 uint16_t hz = 0;                          //revolutions per ...
     sec (*100 to be sent as integer with 2 decimals)
39 double hzscale = 100 * 1000000 / 7;    //scaling factor ...
     for hz
40 int16_t hzdes = 30;                       //desired revolution
41
42 //PWM generation
43 int period = 20000;                  //20 ms period
44 int noduty = period * 0.05;          //no duty load
45 double I = 1000;                     //duty variation ...
     parameter for motor
46 double K = 0;                        //duty variation ...
     parameter for jet (%)
47 int16_t Kdes = 10;                   //desired duty for ...
     the jet
48
49 //Counters
50 int c = 0;                        //global counter
51 int chz;                          //counter to measure the hz
52
53 //Temporary 16 - 32 bit byte
54 byte b16[2];
55 byte b32[4];
56
57 //Pressure variables
58 double rho = 1.225;               //density of air
59 uint16_t Uj = 0;                  //jet velocity ...
                        (ms-1)        (*100 to be sent as ...
     integer with 2 decimals)
60 double dp = 0;                   //pressure difference ...
                 (Pa)
61 double pV = 0;                   //voltage read from ...
     analog pin  (V)
62 double pV0;                      //voltage offset measured ...
     in calibration
63 double perr = 1;                 //the error associated
64
65 //Servo data
66 Servo c1;                         //servo 1 handle
67 Servo c2;                         //servo 2 handle
68 Servo c3;                         //servo 3 handle
```

```
69 int16_t a1;                    //angle to send to servo ...
     when same
70 int a3[3];                    //angle to send to servo ...
     when sep
71 int mina = 10;                //minimum angle
72 int maxa = 20;                //maximum angle
73 int16_t hang;                  //heading angle
74
75 ////////////////////////////////////////////////////////////////////////
76
77 void setup() {
78
79 //GENERAL
80 //setting the serial
81 Serial.begin(115200);
82 //setting the resolution of analog pin to 12 bit
83 analogReadResolution(12);
84
85 //PINS
86 //setting all pinmodes
87 pinMode(motpin,   OUTPUT);
88 pinMode(jetpin,   OUTPUT);
89 pinMode(rpspin,   INPUT);
90 pinMode(escpinm,  INPUT);
91 pinMode(escpinj,  INPUT);
92 pinMode(tmppin,   OUTPUT);
93 //attaching servo
94 c1.attach(c1pin);
95 c2.attach(c2pin);
96 c3.attach(c3pin);
97
98 //INTERRUPTS
99 //attaching interupt to measure rps
100 attachInterrupt(rpspin, hzint, RISING);
101 //timers for the pwm generation
102 Timer6.attachInterrupt(motup).setPeriod(period);          ...
     //mot up signal
103 Timer7.attachInterrupt(jetup).setPeriod(period);          ...
     //jet up signal
104 Timer8.attachInterrupt(jetdown).setPeriod(noduty);       ...
     //jet down signal
```

```
105 Timer1.attachInterrupt(motdown).setPeriod(noduty);        ...
      //mot down signal
106
107
108 //INITIALISING MOTOR
109 initialiseMOT();
110 initialiseJET();
111
112 //INITIALISING SERVO
113 angUP(mina);
114
115 //CALIBRATING PRESSURE READ
116 calibrateP();
117
118 //SENDING READY SIGNAL
119 Serial.print("ready");
120 }
121
122 ////////////////////////////////////////////////////////////////////
123
124 void loop() {
125
126 //CHECKING FOR MESSAGES
127 checkmessage();
128
129 //THINGS TO DO NOT EVERY LOOP
130 if (c % 5000 == 0) {
131
132 //SENDING THE HZ
133 senddat();
134
135 //RUNNING THE MOTOR EVERY
136 if (startM && motIni) motctrl();
137
138 //RUNNING THE JET
139 if (startJ && jetIni) jetctrl();
140
141 //WRITTING THE STATUS
142 if ((startJ && abs(Kdes-K)≤0.1)       && (startM && ...
      abs((hz / 100) - hzdes) ≤ 2))        ...
      digitalWrite(tmppin, HIGH);
```

```
143 else if ((startJ && abs(Kdes-K)≤0.1) && !startM) ...
                                                ...
      digitalWrite(tmppin, HIGH);
144 else if ( !startJ                        && (startM && ...
      abs((hz / 100) - hzdes) ≤ 2))          ...
      digitalWrite(tmppin, HIGH);
145 else ...

      digitalWrite(tmppin, LOW);
146
147 }
148
149 //INCREMENT COUNTER
150 c++;
151 }
152
153 ////////////////////////////////////////////////////////////////////////
154
155 //MOT INIT FNC
156 void initialiseMOT() {
157 //while motor not initialise
158 while (!motIni) {
159 //if motor has power
160 if (digitalRead(escpinm) == HIGH) {
161 //start timer
162 Timer6.start();
163 delay(1000);
164 //run through duty cycle value range
165 for (int j = 0; j < 21 ; j++) {
166 Timer1.setPeriod(0.05 * period * (1 + j / 20));
167 delay(30);
168 }
169 //change boolean
170 Timer1.setPeriod(noduty);
171 motIni = true;
172 }
173 }
174 }
175
176 ////////////////////////////////////////////////////////////////////////
177
```

```
178 //JET INIT FNC
179 void initialiseJET() {
180 //while motor not initialise
181 while (!jetIni) {
182 //if motor has power
183 if (digitalRead(escpinj) == HIGH) {
184 //start timer
185 Timer7.start();
186 delay(1000);
187 //run through duty cycle value range
188 for (int j = 0; j < 21 ; j++) {
189 Timer8.setPeriod(0.05 * period * (1 + j / 20));
190 delay(30);
191 }
192 //change boolean
193 Timer8.setPeriod(noduty);
194 jetIni = true;
195 }
196 }
197 }
198
199 ////////////////////////////////////////////////////////////////////////
200
201 //CHECK MSG FNC
202 void checkmessage() {
203 //getting the new character at the end of the line
204 if (Serial.available() > 0) {
205 for (int i = 0; i < 6; i++)      command[i] = command[i ...
      + 1];
206 command[5] = Serial.read();
207 }
208 //checking which message was sent
209 //start the motor
210 if (strcmp(command, motstr) == 0)         startM = true, ...
               command[5] = 'n';
211 //stop motor
212 else if (strcmp(command, stpmot) == 0)    startM = ...
      false,          Timer1.setPeriod(noduty), ...
                                  I = 1000, ...
                                   command[5] = 'n';
213 //set desired velocity
```

```
214 else if (strcmp(command, setvel) == 0)   Rbyte(), ...
                    hzdes = ( b16[0] | (b16[1] << 8) ), ...
                      command[5] = 'n';
215 //start the jet
216 else if (strcmp(command, jetstr) == 0)   startJ = true, ...
                command[5] = 'n';
217 //stop thw jet
218 else if (strcmp(command, stpjet) == 0)   startJ = ...
      false,          Timer8.setPeriod(noduty), ...
                                  K = 10, ...
                                     command[5] = 'n';
219 //set desired jet duty
220 else if (strcmp(command, setjet) == 0)   Rbyte(), ...
                    Kdes = ( b16[0] | (b16[1] << 8) ), ...
                       command[5] = 'n';
221 //set desired angle on servo
222 else if (strcmp(command, setang) == 0)   Rbyte(), ...
                    a1 = ( b16[0] | (b16[1] << 8) ), ...
                         angUP(constrain(a1, mina, ...
      maxa)),       command[5] = 'n';
223 //calibrating the pressure
224 else if (strcmp(command, calpre) == 0)   calibrateP(), ...
                 command[5] = 'n';
225 //set desired heading for servo
226 else if (strcmp(command, sethdg) == 0)   Rbyte(), ...
                    hang = ( b16[0] | (b16[1] << 8) ), ...
                       hdgUP(), ...
                                    command[5] = 'n';
227 }
228
229 ////////////////////////////////////////////////////////////////////////
230
231 //RUN MOT
232 void motctrl() {
233 //changing the PWM index counter if the desired RPS is ...
      not reached
234 if ((hz / 100) ≤ hzdes - 2) I = I + 0.1, I = ...
      constrain(I, 1040, 1300);
235 if ((hz / 100) ≥ hzdes + 2) I = I - 0.1, I = ...
      constrain(I, 1040, 1300);
236 Timer1.setPeriod(I);
```

```
237 }
238
239 ////////////////////////////////////////////////////////////////////////
240
241 //RUN JET
242 void jetctrl() {
243 //changing the PWM index counter if the desired RPS is ...
      not reached
244 temp = false;
245 if (K ≤ Kdes) K = K + 0.1, K = constrain(K, 18, 100);
246 if (K ≥ Kdes) K = K - 0.1, K = constrain(K, 18, 100);
247 Timer8.setPeriod(1000 + 10 * K);
248 }
249
250 ////////////////////////////////////////////////////////////////////////
251
252 //SENDING THE HZ THROUGH SERIAL
253 void senddat() {
254 //calculate the jet velocity
255 calV();
256 //setting the outgoing bytes
257 setbyte(hz, Uj);
258 Serial.write(b32, sizeof(b32));
259 }
260
261 ////////////////////////////////////////////////////////////////////////
262
263 //SETTING THE 32BIT BYTES
264 void setbyte(int16_t a, int16_t b) {
265 b32[0] = a & 255; b32[1] = (a >> 8) & 255; b32[2] = b & ...
      255; b32[3] = (b >> 8) & 255;
266 }
267
268 ////////////////////////////////////////////////////////////////////////
269
270 //RECIEVING 16bit Byte FNC
271 void Rbyte() {
272 //waiting for more than one byte to be available
273 while (Serial.available() ≤ 1)     delay(10);
274 //filling the the 16bit byte with the information
275 if (Serial.available() ≥ 2)        b16[0] = ...
```

```
    Serial.read(),    b16[1] = Serial.read();
}

////////////////////////////////////////////////////////////////////////////

//CALC HZ FNC
void hzint() {
hz = hzscale / (micros() - chz);
chz = micros();
}

////////////////////////////////////////////////////////////////////////////

//GEN PWM FNC
//up for motor
void motup() {
digitalWrite(motpin, HIGH);
Timer1.start();
}
//up for jet
void jetup() {
digitalWrite(jetpin, HIGH);
Timer8.start();
}
//down for motor
void motdown() {
digitalWrite(motpin, LOW);
Timer1.stop();
}
//down for jet
void jetdown() {
digitalWrite(jetpin, LOW);
Timer8.stop();
}

////////////////////////////////////////////////////////////////////////////

//UPDATE SERVO FUNCTION
//with same angle
void angUP(int a) {
c1.write(a);
```

```
316 c2.write(a);
317 c3.write(a);
318 }
319 //with different angle
320 void angUP(int a[3]) {
321 c1.write(a[0]);
322 c2.write(a[1]);
323 c3.write(a[2]);
324 }
325
326 ////////////////////////////////////////////////////////////////////////
327
328 //CALCULATE ANGLES FROM HEADING AND UPDATE SERVOS
329 void hdgUP() {
330 //convert heading to angle of maximum lift in radians ...
      (aka opposite than heading)
331 double tmp = (double) hang / 180 * pi + pi;
332 //trigonometry to find the desired angles
333 for (int i = 0; i < 3; i++) {
334 a3[i] = cos(tmp - i * 2 * pi / 3) * (maxa - mina)+ mina ;
335 }
336 //updating the angles
337 angUP(a3);
338 }
339
340 ////////////////////////////////////////////////////////////////////////
341
342 //CALCULATE THE AIRSPEED FROM PRESSURE
343 void calV() {
344 double tmpV = 0;  //volatge tmp var
345 int nV = 100;     //number of voltage points
346 //getting the average voltage of multiple points
347 for(int i = 0; i<nV; i++){
348 tmpV += analogRead(prepin);
349 }
350 //getting voltage from the pin
351 pV = (double) tmpV * 5 / (4096 * nV) - pV0;
352 //getting pressure from voltage
353 dp = max((pV - 1) * 1000, 0);
354 //calculating the jet velocity using          p = ...
      1/2*rho*V^2
```

```
355 Uj = sqrt(2 * dp / rho) * 100;
356 }
357
358 ////////////////////////////////////////////////////////////////////////
359
360 //CALIBRATE THE PRESSURE MEASUREMENT
361 void calibrateP() {
362 //at rest the voltage read must be 1, pV0 is the ...
      voltage offset
363 //function takes the average of 10 points
364 pV0 = 0;
365 for (int i = 0; i < 10; i++) {
366 pV0 += (double) analogRead(prepin) * 5 / 4096 - 1;
367 }
368 pV0 /= 10;
369 }
```